Collective Rydberg Excitations in Magic Traps

Dissertation
zur
Erlangung des Doktorgrades (Dr. rer. nat.)
der
Mathematisch-Naturwissenschaftlichen Fakultät
der
Rheinischen Friedrich-Wilhelms-Universität Bonn

vorgelegt von
Lukas Paul Daniel Ahlheit
aus
Braunschweig

Bonn 2025

Angefertigt mit Genehmigung der Mathematisch-Naturwissenschaftlichen Fakultät der Rheinischen Friedrich-Wilhelms-Universität Bonn

1. Gutachter: Prof. Dr. Sebastian Hofferberth
2. Gutachter: Prof. Dr. Stefan Linden

Tag der Promotion:
Erscheinungsjahr:

Do not think in other people's words.

Abstract

Single photons typically interact only weakly with atoms and, even less so, with each other. By coupling photons to highly excited Rydberg states in atomic ensembles, strong long-range interactions between polaritons are induced, enabling effective photon–photon interactions through the polariton–polariton coupling.

This thesis presents a combined theoretical and experimental investigation of magic trapping for atoms in both the ground and Rydberg states. The central focus is on how the trap geometry determines the magic condition that optimizes photon storage as a collective excitation in an ultracold atomic ensemble.

The first part of the thesis introduces electromagnetically induced transparency and the storage of single photons as atomic spin waves. Various mechanisms that lead to dephasing of these coherent collective excitation are discussed, including atomic motion and inhomogeneous differential light shifts across the atomic ensemble. To mitigate these effects, a magic standing-wave trap is considered—one that not only minimizes the differential light shift between the ground and Rydberg states, but also provides spatial confinement of the atoms.

To identify a magic trapping wavelength, optical potentials are calculated for atoms in both the ground and Rydberg states. This analysis goes beyond the standard dipole approximation, which breaks down for Rydberg atoms in standing-wave traps with near-infrared wavelengths, as the wave function of the Rydberg electron can extend over several micrometers. Instead, the full energy shift is evaluated by accounting for the interaction of the almost-free Rydberg electron with the periodic intensity profile of the standing-wave trap. This effect is considered to evaluate the resulting trap potentials for two one-dimensional trap configurations—a running-wave and a standing-wave trap—both of which are later implemented experimentally.

Next, this thesis presents the experimental apparatus for preparing ultracold ensembles of rubidium-87 atoms, which serve as the medium for Rydberg excitations and photon storage. The apparatus was reconstructed during the course of this work, following its relocation from the University of Southern Denmark to the University of Bonn in 2021. An overview of the experiment is provided, along with selected characterization steps relevant to the results presented in this thesis.

Based on the calculated trap potentials for the ground and Rydberg states, a one-dimensional trap is implemented into the experimental apparatus. Rydberg states are difficult to trap, because the Rydberg electron is repelled by oscillating electric fields. By coupling a Rydberg $nS_{1/2}$ state near-resonantly to the $6P_{3/2}$ state, attractive optical potentials for the Rydberg atoms are created. Magic trapping conditions for both trap geometries are theoretically derived and subsequently tested in photon storage and retrieval experiments. The optimal trap wavelength minimizes the differential light shift-induced dephasing in both the running-wave and the standing-wave trap configuration. Additionally, it is shown how confinement in the standing-wave trap modifies the dynamics of the storage process due to oscillatory atomic motion within the standing-wave wells and the formation of ultralong-range Rydberg molecules.

Parts of this thesis have been published in the following article:

[1] Lukas Ahlheit, Chris Nill, Daniil Svirskiy, Jan de Haan, Simon Schroers, Wolfgang Alt, Nina Stiesdal, Igor Lesanovsky, and Sebastian Hofferberth, *Magic running- and standing-wave optical traps for Rydberg atoms*, Physical Review A **111** (2025) 013115

Contents

CHAPTER 1

Introduction

In quantum optics, the interaction between light quanta—single photons—and matter is studied to explore fundamental physical principals, and to enable the control of photons for technological applications [2, 3]. Atoms represent a powerful quantum matter platform due to their well-characterized internal structure and the availability of precise control techniques. However, single photons generally interact only weakly with individual atoms, and even more weakly with other photons [4].

One approach to addressing the challenge of achieving strong photon-atom coupling involves cavity quantum electrodynamics (QED) systems [5, 6], where a single atom is coupled to an optical cavity. Such systems have demonstrated strong coupling between photons and atoms [7–9], enabling effective photon–photon interactions that can be used, for example, to realize single-photon switches [10] and photon–photon quantum gates [11].

As an alternative to cavity QED, the coupling of single photons to atoms can be enhanced by using many atoms collectively. Under the condition of electromagnetically induced transparency, the propagating photons can be coherently converted into propagating or stationary excitations within atomic ensembles [12, 13]. In this context, the coherent superposition of the quantum state of light and the collective state of matter can be described as a quasi-particle known as a dark-state polariton [14]. The matter component of a dark-state polariton consists of a collective spin excitation shared across the ensemble. These collective excitations are called spin waves and can be used to realize a quantum memory [15–21].

Two polaritons can experience strong interactions, if one of the involved atomic states is a Rydberg state [22]. The long-range dipolar interaction between Rydberg atoms has many applications, especially the Rydberg blockade, which restricts the number of simultaneous excitations within a given volume to one [23–29]. When combined with collective enhancement, this mechanism yields strong optical nonlinearities at the few-photon level [30, 31].

Furthermore, the strong dipole–dipole interaction between Rydberg atoms has been mapped onto optical fields [28, 32, 33], enabling photon–photon interaction mediated by polariton–polariton coupling [34, 35]. These interactions support a range of single-photon applications, including single-photon transistors [36, 37], phase gates [38] and quantum-logic gates [39]. However, the performance of these applications is often limited by decoherence of the collective atomic states. Similar decoherence is also limiting the performance of quantum memories in atomic ensembles [19, 40].

The coherence time of collective excitations in ultra-cold atomic ensembles is limited by several

dephasing mechanisms [41]. One source of dephasing is the thermal motion of the atoms sharing the excitation, which leads to a gradual loss of the spin wave coherence [18]. The rate of this thermal dephasing depends on the effective k-vector of the spin wave created within inside the atomic ensemble [42].

Encoding the dark-state polariton as a coherence between atomic ground states typically results in small k-vector mismatches, allowing coherence times on the order of milliseconds [18, 43, 44] and, under favorable conditions, even seconds [45]. In contrast, when a Rydberg state is involved in the collective excitation—requiring a two-photon transition—the resulting effective k-vector is generally larger, which increases the sensitivity to atomic motion compared to configurations involving only ground states.

To mitigate motional dephasing, one approach is to create a spin wave phase pattern that compensates the unknown phase resulting from thermal motion after a given storage duration [46]. Alternatively, confining the atomic ensemble along the direction of the spin wave k-vector using an optical standing-wave trap can restrict atomic motion in the relevant direction and thus suppress dephasing.

However, optical trapping potentials can lead to an additional dephasing mechanism arising from the differential light shift between the ground and Rydberg states [47, 48]. In a typical optical dipole trap, atoms in the ground state are confined, while atoms in Rydberg states experience a repulsive potential [49]. This repulsion arises from the almost-free electron in high-lying Rydberg states. When exposed to oscillating electric field, the free electron experiences a ponderomotive energy shift [50], which constitutes the dominant contribution to the light shift for Rydberg states [51]. The result is an overall repulsive potential acting on Rydberg atoms within the trapping field.

To limit the influence of both motional and differential light shift–induced dephasing mechanisms, the atomic ensemble can be confined in optical standing-wave traps with an equal dynamic polarizability for two (or more) involved states. In such traps—known as "state-insensitive" or magic traps [52, 53]—the optical potential experienced by the atoms is effectively the same for the involved states, thereby suppressing differential light shift–induced dephasing.

One approach to create magic traps for ground-to-Rydberg coherences involves blue-detuned optical traps, in which both the ground and Rydberg states are equally repelled from high intensity regions [54, 55]. The combination of a standing-wave for axial confinement and a bottle beam for radial confinement of the atomic ensemble requires complicated beam shaping for such a blue-detuned magic trap. A more straightforward alternative is the use of red-detuned standing-wave traps, where both the ground and Rydberg states can be confined with minimal differential light shifts. To counteract the ponderomotive repulsion experienced by the almost-free electron in the Rydberg state, the trapping wavelength can be tuned near a resonance between the Rydberg state and a low-lying state. This near-resonant coupling strongly modifies the polarizability of the Rydberg atom [56].

However, for Rydberg states with principal quantum number $n \gtrsim 55$, the spatial extent of the electron wave function becomes comparable to half the wavelength of the near-infrared light typically used in optical dipole traps [22]. In this regime, the dynamic polarizability becomes sensitive to the spatial intensity variations of the trapping light field [50, 57, 58]. Despite these challenges, magic traps for ground and Rydberg states have been successfully implemented in various experiments [45, 59], and have been used to extend coherence times between ground and Rydberg states [60].

Previously, our rubidium quantum optics experiment applied two different trapping strategies. In one approach, a red-detuned crossed optical dipole trap was used to confine atoms in the ground state. To avoid differential light shifts during Rydberg excitation, the trapping beams were turned off; however, this configuration still suffered from thermal dephasing. In the second approach, a

red-detuned dimple trapping beam was used to confine atomic ensembles within volumes small enough to be fully blockaded by the Rydberg interaction. In this case, the dimple trap remained on during the Rydberg experiments and the induced light shift was exploited to distinguish atoms inside the trap from those outside, thereby improving the fidelity of the Rydberg blockade [61]. Nevertheless, in these small ensembles, the coherence of the collective excitations remained limited by both thermal and the differential light shift–induced dephasing.

In this thesis, I report on the implementation of a magic trap for Rydberg atoms and its application to extend the coherence times of collective Rydberg excitations. In Chapter 2, I introduce the theoretical concepts relevant to the Rydberg quantum optics experiments presented in this work. Subsequently, in Chapter 3, I derive the trapping potentials for both the ground and the Rydberg state, providing a theoretical basis for the realization of a magic trap. Chapter 4 describes the reassembly of the experimental apparatus following its relocation from Odense, Denmark, to Bonn, Germany, in 2021. The primary upgrade to the setup was the integration of the magic trap, used to confine the atomic ensemble that serves as the platform for collective Rydberg excitations. In Chapter 5, I detail the experimental implementation and the use of collective excitations to probe differential light shifts within a one-dimensional trap. Through photon storage and retrieval experiments, I resolved differences in the effective polarizability of Rydberg atoms confined in running-wave and standing-wave trap configurations. Finally, Chapter 6 summarizes the results of this thesis and outlines potential experimental improvements and future directions for investigation.

CHAPTER 2

Nonlinear Quantum Optics with Collective Rydberg Excitations

Throughout this thesis, light storage is considered as collective excitations in ensembles of atoms. This chapter introduces the relevant theoretical concepts and equations. First, electromagnetically induced transparency (EIT) in a three-level system is presented [62], along with a discussion of how EIT enables the storage of photons as collective excitations in atomic media. The chapter then introduces Rydberg states and highlights their extreme properties in comparison to ground-state atoms. We review the mapping of strong atomic interactions between Rydberg states onto photons. Finally, we examine the limitation of collective Rydberg excitations when using them for single photon storage experiments.

2.1 Electromagnetically Induced Transparency

For the discussion in this thesis, we first consider a three-level system. Figure 2.1(a) shows a three-level ladder scheme with a weak probe field close to resonance with the $|1\rangle \leftrightarrow |2\rangle$ transition. The transmission of the probe field with frequency ω through the atomic medium is modified in the presence of a strong control laser driving the $|2\rangle \leftrightarrow |3\rangle$ transition. The modification in such a three-level system is for instance electromagnetically induced transparency (EIT) [12] or coherent population trapping [63]. We focus our discussion on the ladder scheme in Fig. 2.1(a) as it is relevant in the case where the upper state $|3\rangle$ is a Rydberg state.

For the three-level system in Fig. 2.1, the linear susceptibility as function of frequency ω is in the weak probe field limit given by [62, 64]

$$\chi^{(1)}(\omega) = \frac{|\mu_{12}|^2\rho}{\epsilon_0\hbar}\left[\frac{4\delta(|\Omega_{32}|^2 - 4\delta\Delta_{21}) - 4\Delta_{21}\gamma_{31}^2}{\left||\Omega_{32}|^2 + (\gamma_{21} + i2\Delta_{21})(\gamma_{31} + i2\delta)\right|^2} + i\frac{8\delta^2\gamma_{21} + 2\gamma_{31}(|\Omega_{32}|^2 + \gamma_{31}\gamma_{21})}{\left||\Omega_{32}|^2 + (\gamma_{21} + i2\Delta_{21})(\gamma_{31} + i2\delta)\right|^2}\right]. \tag{2.1}$$

Here, μ_{12} is the electronic dipole moment for the $|1\rangle \leftrightarrow |2\rangle$ transition, ρ is the atom number density, $\hbar$ is the reduced Planck constant, $\Delta_{21} = \omega - \omega_{21}$ and $\Delta_{32} = \omega - \omega_{32}$ are the single-photon detunings on the probe and control transition, $\delta = \Delta_{21} - \Delta_{32}$ is the two-photon detuning, and Ω_{32} is the control Rabi

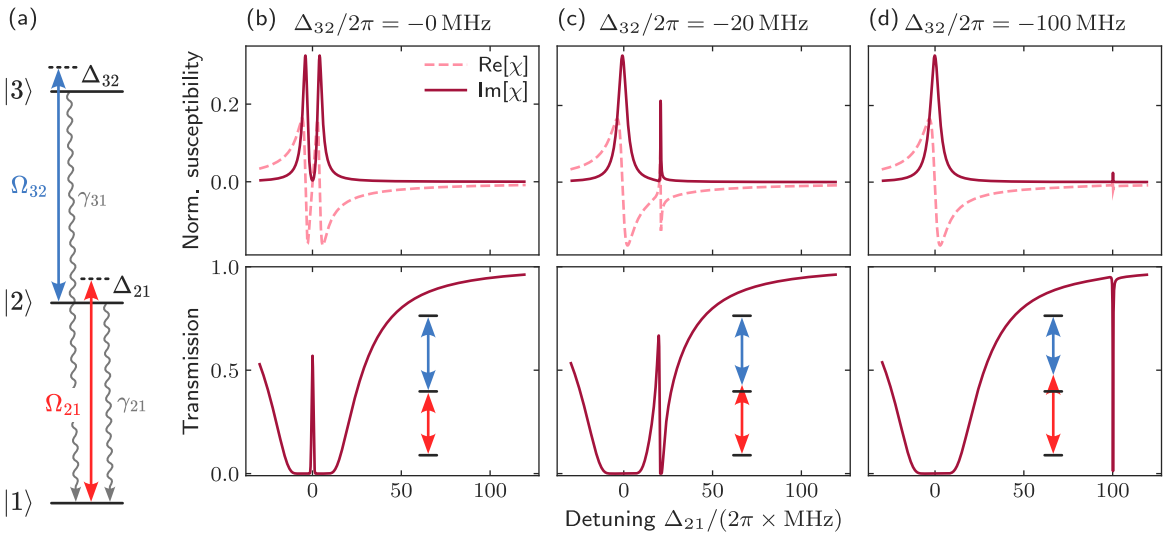

Figure 2.1: (a) Three atomic levels coupled by two laser beams with Rabi frequencies $\Omega_{21(32)}$ and transition frequency $\omega_{21(32)} = |E_{2(1)} - E_{3(2)}|/\hbar$, respectively. (b), (c), (d) Theoretical calculation of the real (dashed) and imaginary (solid) part of the susceptibility $\chi^{(1)}$, normalized to the prefactor in Eq. 2.1, in the top row and transmission in the bottom row as function of the detuning Δ_{21}. The calculation is for control Rabi frequency $\Omega_{32} = 2\pi \times 8\,\mathrm{MHz}$, and decay rates $\gamma_{21} = 2\pi \times 6.07\,\mathrm{MHz}$ and $\gamma_{31} = 2\pi \times 0.1\,\mathrm{MHz}$. The control detuning is different for (b), (c), and (d). The three cases are (b) electromagnetically induced transparency with $\Delta_{32} = 2\pi \times 0\,\mathrm{MHz}$, (c) an intermediate regime with $\Delta_{32} = -2\pi \times 20\,\mathrm{MHz}$, and (d) a two-photon Raman resonance with $\Delta_{32} = -2\pi \times 100\,\mathrm{MHz}$. The small schematics show the resonant two-photon transition between $|1\rangle$ and $|3\rangle$ in the three cases.

frequency.

The transmission through and refractive index of an optically thick medium follows from the susceptibility as [64]

$$T(\omega) = \exp\Big(-kL\,\mathrm{Im}\Big[\chi^{(1)}(\omega)\Big]\Big), \tag{2.2}$$

$$n(\omega) = \sqrt{1 + \mathrm{Re}[\chi^{(1)}(\omega)]}, \tag{2.3}$$

with the wave vector of the light $k = 2\pi/\lambda$, the wavelength of the light λ, and the atomic cloud length L. Figure 2.1(b) shows the real and imaginary parts of the linear susceptibility $\chi^{(1)}(\omega)$ in resonance with the intermediate state $|2\rangle$. The corresponding theoretical transmission, shown in the lower panel and calculated using Eq. 2.2, exhibits a transparency window for the probe field. The transmission on this EIT resonance does not reach unity, as a finite decay rate γ_{31} from the state $|3\rangle$ to the state $|1\rangle$ is taken into account.

For larger detunings Δ_{32}, as shown in Fig. 2.1(c) and 2.1(d), the transmission feature transitions from a transparency window into a dispersive shape and, at sufficiently large detuning, into a narrow two-photon Raman resonance [65], respectively.

The EIT transmission peak shown in Fig. 2.1(b) is accompanied by a positive slope of the real part of the susceptibility, which determines the light propagation through the medium. For a wave packet

that travels under EIT conditions, the group velocity is given by [64]

$$v_{\mathrm{gr}} = \left.\frac{d\omega}{dk}\right|_{\delta=0} = \frac{c}{n + \omega \cdot (dn/d\omega)}. \tag{2.4}$$

The experimental control over the refractive index allows slowing down an incoming probe field inside an atomic ensemble [16, 66]. In the case of a few-photon probe pulse, the superposition between the photonic and matter states can be described as a quasi-particle, a dark-state polariton [14]. The properties of these polaritons are given by the mixture between the atomic coherence and the probe light field.

2.1.1 Storage of Light Pulses in Collective States

The mechanism of slowing down a light pulse introduced in Eq. 2.4 can be continued to the storage of a light pulse by completely turning off the control light [17].

During the photon storage, where the control light on the transition $|2\rangle \leftrightarrow |3\rangle$ is absent, the dark-state polariton is fully transferred into the coherence between the states $|1\rangle$ and $|3\rangle$. A single photon stored as a shared excitation across an ensemble of N atoms can be viewed as a wave of excited spins [67] and described as an entangled Dicke-like state given by [68, 69]

$$|\psi(t)\rangle = \frac{1}{\sqrt{N}} \sum_j \exp\left[i\,\boldsymbol{k}\cdot\boldsymbol{r}_j(t)\right] \left|1_1 \ldots 3_j \ldots 1_N\right\rangle, \tag{2.5}$$

where $\boldsymbol{k}$ is the wave vector of the photon excitation, and $\boldsymbol{r}_j(t)$ denotes the three-dimensional position of atom j at time t. The state $\left|1_1 \ldots 3_j \ldots 1_N\right\rangle$ denotes the state where the jth atom is in state $|3\rangle$, and all other atoms are in state $|1\rangle$. The polaritons have been turned into stationary collective excitations, where the polaritons are mapped onto atomic hyperfine ground states [15, 16]. In such an EIT scheme, storage durations in the millisecond [18, 43, 44] to minute [45] timescale have been experimentally demonstrated.

The storage duration is limited by the dephasing of the stored collective state. To investigate where the decoherence comes from, the time evolution of the collective state is considered, and the retrieval efficiency $\eta(t_s)$ is calculated. The spin wave that can be converted back into a forward propagating photon by the coupling with the control laser is denoted by $|\psi(0)\rangle$. During the storage duration t_s, the collective state evolves into the state $|\psi(t_s)\rangle$. The retrieval efficiency $\eta(t_s)$ that quantifies the quantum state overlap after a time t_s is given by [48]

$$\eta(t_s) = |\langle\psi(0)|\psi(t_s)\rangle|^2. \tag{2.6}$$

Since the photon is stored in the medium as an atomic coherence, the storage duration is limited by various mechanisms [41], including thermal atomic motion [18], state lifetimes, and differential light shifts across the atoms that share the coherence [47]. The motion of each contributing atom j modifies the phase of the collective state in Eq. 2.5, which leads to a decoherence in the state overlap upon photon retrieval. In the thermal expansion of the atomic ensemble, the atom j follows a trajectory like $\boldsymbol{r}_j(t) = \boldsymbol{r}_{j,0} + \boldsymbol{v}_j t$ with a velocity $\boldsymbol{v}_j$. In that case, the quantum state overlap in Eq. 2.6 is given by

a Gaussian decay as [18, 70]

$$\eta(t_s) = \eta_0 e^{-t_s^2/\tau_T^2}. \tag{2.7}$$

Here, τ_T is the decay constant, or coherence time, of this Gaussian decay envelope, and η_0 is a constant that captures imperfections during the storage and retrieval, like residual absorption. The decay constant is related to the atomic temperature T as

$$\tau_T = 1/\left(k\, v_{\text{atoms}}\right) = 1/\left(k\sqrt{k_B T/m}\right), \tag{2.8}$$

where v_{atoms} is the one-dimensional average speed and $k = 2\pi/\lambda$ is the wave vector component in the direction of the movement. In order to extend the storage duration, the mean velocity of the atoms can be reduced by laser cooling [71–73]. Additionally, the collective state in Eq. 2.5 becomes less sensitive to the time evolution of the atom positions $\boldsymbol{r}(t)$ for lower effective k-vectors. As an example, the collective excitation can be created with the absorption of two photons, as shown in Fig. 2.1(b). The resulting effective vector $\boldsymbol{k} = \boldsymbol{k}_1 + \boldsymbol{k}_2$ can be tailored with the wavelength and propagation direction of the two photons, with their respective k-vectors $\boldsymbol{k}_1$ and $\boldsymbol{k}_2$ [74]. The storage in an EIT scheme with two atomic ground states (a so-called Lambda scheme) makes use of similar wave vectors of the two photons, while the two photons co-propagate, to result in low effective k-vectors [15, 16].

For the EIT ladder scheme in Fig. 2.1(a) two photons have to be absorbed, and it is advantageous to send the two counter-propagating to partially cancel the momentum kick onto the atom associated with photon absorption [75, 76]. For parallel excitation beams, the vector multiplication between the wave vector $\boldsymbol{k}$ and position $\boldsymbol{r}(t)$ implies that only the atomic movement along the k-vector becomes relevant.

Besides the thermal dephasing, the collective state in Eq. 2.5 is influenced by the surroundings of the atoms. In the scope of this thesis, the relevant effect is the presence of the trapping potential during the Rydberg experiments. In Ref. [48], a model for photon storage and retrieval experiments is developed that includes the dephasing of the collective state by differential light shifts. The model describes the time evolution of atoms trapped in a red-detuned optical dipole trap. The collective state in Eq. 2.5 is extended with a phase factor $\exp\left[-iU_{q,j}(\boldsymbol{r})t/\hbar\right]$ for each atom j in its respective state q. Here, the position-dependent trapping potential is denoted with $U_{q,j}(\boldsymbol{r})$, and two different trapping potentials can be considered for the states $|1\rangle$ and $|3\rangle$.

As another decoherence mechanism, the coherence in the collective excitations can be lost through the decay of any involved atomic state [41]. In the photon storage and retrieval experiments, the radiative decay is given by

$$f(t_s) = A\exp\left(-t_s/\tau\right), \tag{2.9}$$

where the timescale of the decay is given by the lifetime τ. The involved states in the collective excitation are ideally long-lived compared to the storage or gate operation in a quantum network.

2.2 Rydberg States

The realization of slow or stored light in atomic ensembles enables new opportunities of few-photon manipulation. As one example, the excited state $|3\rangle$ in the three-level scheme in Fig. 2.1(a) can

be a Rydberg state [28]. Rydberg states of atoms are characterized by strong and long-range interactions [77]. In the following section, we introduce Rydberg atoms, and discuss the possibility of mapping Rydberg-Rydberg interactions onto photons.

Rydberg atoms are atoms excited into states with high principal quantum number n [22]. The properties of Rydberg atoms compared to ground-state atoms are given in table 2.1 for rubidium-87.

Below, we provide the properties of Rydberg states that are relevant for the rest of the thesis. The binding energy for an alkali atom excited to a Rydberg state is given by [22]

$$E(n,j,l) = -\frac{R'}{(n^*)^2}, \tag{2.10}$$

with the specific Rydberg constant R' and the effective principal quantum number $n^* = n - \delta_{njl}$. The quantum defects δ_{njl} are corrections to the case of hydrogen, and describe the shielding of the core by the inner electrons, such that the single outer electron experiences a weaker potential.

The quantum defects depend on the total angular momentum quantum number $j = |l \pm s|$, the orbital angular momentum quantum number l, and the spin quantum number s. In high Rydberg states, the valence electron is only weakly bound, which leads to a largely increased size of the electron wave function. The electron orbit radius r_e can be calculated as the most probable electron radius with

$$r_e = \langle r \rangle = \langle nS|r|nS\rangle = \int_0^\infty R^2(r) r^3 dr. \tag{2.11}$$

Here, $R(r)$ is the radial electron wave function in the Rydberg state nS [78, 79]. r_e can be approximated by [22]

$$r_e = [3(n^*)^2 - l(l+1)]/2.$$

The two calculations agree within a few percent, and if not stated otherwise we use Eq. 2.11 in this thesis. The Rydberg atom with the large electron wave function is sensitive to external fields, and this is described by the static polarizability α_{static} given by [80]

$$\alpha_{\text{static}} = [2.202 \times 10^{-9}(n^*)^6 + 5.53 \times 10^{-11}(n^*)^7]\,\text{MHz}/(\text{V/cm})^2. \tag{2.12}$$

The large electron wave function in Rydberg states also results in a small overlap integral with low-lying states. The overlap is characterized by the reduced matrix elements D_{an} between two atomic states with principal quantum number a and n as

$$D_{an} = \langle aP_{3/2}||d||nS_{1/2}\rangle. \tag{2.13}$$

The reduced matrix element for a Rydberg S-state as $D_{an} \propto (n^*)^{-3/2}$. The lower reduced matrix element in Table 2.1 for the Rydberg state means a reduced coupling of optical light fields to the upper transition of the EIT scheme in Fig. 2.1(a).

One benefit of weaker coupling of Rydberg states to lower-lying states is a prolonged lifetime [22]. Here, we present the equations to calculate the lifetimes relevant for our experimental parameters.

A simple model for spontaneous and blackbody-radiation-induced transitions was developed by

Table 2.1: The scaling of atomic state properties with the effective principal quantum number n^*. The two example states are for rubidium-87 atoms. The transition dipole moments are calculated as the reduced matrix elements $\left|\langle 5P_{3/2}||d||nS_{1/2}\rangle\right|$ in Eq. 2.13, following the definition in Ref. [79]. a_0 is the Bohr radius, and e is the elementary charge. Table adapted from Ref. [81].

Property	$(n^*)^x$	$5S$ - ground state	$90S$ - Rydberg state
Binding energy E	$(n^*)^{-2}$	4.18 eV	1.8 meV
Electron orbit radius r_e	$(n^*)^2$	5.632 a_0	11319 a_0
Static polarizability α	$(n^*)^7$	$-79.4\,\mathrm{MHz/(V/cm)^2}$	$-1494\,\mathrm{MHz/(V/cm)^2}$
Reduced matrix element D_{an}	$(n^*)^{-3/2}$	5.98 ea_0	0.006 ea_0
van der Waals C_6 coefficient	$(n^*)^{11}$	4707 au	-1.16×10^{23} au

Beterov et al. [82]. At zero temperature, the Rydberg state lifetime is given by

$$\frac{1}{\tau_0} = \frac{1}{\tau_s \cdot \left(n^*\right)^\delta}, \tag{2.14}$$

where τ_s and δ for Rb are given in table II in Ref. [82]. The lifetime due to spontaneous decay is commonly approximated by the scaling $\tau_0 \propto (n^*)^3$ [81]. The modified principal quantum number $n^* = n - \delta_{nlj}$ is calculated using quantum defects δ_{nlj} from Ref. [83] for rubidium-87. For temperatures above zero, the blackbody radiation (BBR) introduces another decay channel for Rydberg states into all lower lying states. In Ref. [82], a semi-empirical analytical function is given as

$$\frac{1}{\tau_{\mathrm{BBR}}(T)} = \frac{A}{\left(n^*\right)} \frac{2.14\times10^{10}}{\exp\left[315780\cdot B/\left(\left(n^*\right)^C\cdot T\right)\right]}. \tag{2.15}$$

The parameters A, B, C, and D for Rb are given in table I of Ref. [82]. Both effects together give an effective lifetime as

$$\frac{1}{\tau_{\mathrm{eff}}} = \frac{1}{\tau_0} + \frac{1}{\tau_{\mathrm{BBR}}(T)}. \tag{2.16}$$

At room temperature $T = 300\,\mathrm{K}$, the effective decay constant is $\tau_{\mathrm{eff}} \approx 49\,\mu\mathrm{s}$ at $n = 45$ and $\tau_{\mathrm{eff}} \approx 263\,\mu\mathrm{s}$ at $n = 90$. In all the photon storage and retrieval experiments in this thesis, we are generally limited by other effects instead of the spontaneous and the blackbody-radiation-induced decay.

2.3 Rydberg Interactions

The interaction between two highly excited atoms in the same state nS can be calculated by the application of non-degenerate second-order perturbation theory [84, 85]. In general, the energy shift

of a quantum state q arising from the interaction with operator $\hat{V}$ can be written as [78, 86]

$$\Delta E_{qq} = \sum_{i,j \neq q} \frac{\left| \langle qq|\hat{V}|ij\rangle \right|^2}{E_{qq} - E_{ij}}, \tag{2.17}$$

where E are the unperturbed energies of states q and all other states i and j coupling to state q. Generally, the interaction between two dipoles scales with $\hat{V} \propto 1/R^3$. As Rydberg atoms are neutral, there is no direct dipole–dipole interaction between two S-states. Instead, two Rydberg S-states interact via their induced dipoles and the resulting interaction for a distance R between the Rydberg atoms is given by [85]

$$V_{\mathrm{vdW}}(R) = -\frac{C_6}{R^6}, \tag{2.18}$$

which is the leading order of the van der Waals interaction. The C_6 coefficient characterizes the interaction between two nS Rydberg states and scales with the principal quantum number as $(n^*)^{11}$, see Table 2.1.

The energy shift due to the Rydberg–Rydberg interaction can be used for different applications. In one application, the energy shift can be used to limit the number of excitations in an atomic medium [23]. The two excitations lasers, in Fig. 2.1(a), are set to a two-photon detuning of $\delta = 2\pi \times 0\,\mathrm{MHz}$. A second Rydberg excitation is only possible at distances, where the interaction induced level shift is less than the transition linewidth to the Rydberg state, where the linewidth is given by the laser linewidth as well as the laser power. This distance is called the Rydberg blockade radius r_{B}.

In an ensemble smaller than the blockade radius r_{B}, the Rydberg blockade realizes an effective two-level system with enhanced coupling to single photons, so-called Rydberg superatoms [30, 87]. Multiple properties of Rydberg superatom have been studied, including internal dynamics [88], and their dipole moment [89]. The generally undesirable dephasing of the collective excitations can be used to subtract photons from an incoming photon pulse [90]. The scheme can be extended to subtract m photons, where the photons are absorbed by m superatoms [91]. Each superatom dephases into a dark state that does not emit into the desired forward propagating mode. Thereby, the m photons are removed from the outgoing light pulse.

The energy shift due to the Rydberg–Rydberg interaction can shift neighboring atoms into resonance with the excitation lasers. The presence of one Rydberg atom facilitates the excitation of neighboring atoms into Rydberg states, which is known in literature as Rydberg facilitation [92–94]. The study of epidemic dynamics has recently been studied in the spread of Rydberg excitations across an atomic gas [95–98].

The strong interaction between two Rydberg atoms can mediate an effective interaction between two photons [26, 27]. Two single photons can be mapped into collective atomic states, as in Eq. 2.5, in two spatially separated ensembles and the long-range interaction results in detectable correlations between the two photons [99]. Furthermore, the effective interaction between photons mediated by Rydberg excitations lead to the observation of bunching [34] and anti-bunching [32, 35] of light. While the photons are stored in the collective excitations, they can be manipulated by e.g. microwave fields [100].

2.4 Limitations for Photon Storage in Collective Rydberg Excitations

The experiments in this thesis are performed with collective states described by Eq. 2.5, where the excited state $|3\rangle$ is a Rydberg state. In this section, we discuss the implications and limitations that arise from involving a Rydberg state in the collective state.

As already discussed, the movement of the atoms during the typical duration of our experiments poses limitations for the achievable coherence times. The temperature of the atomic cloud represents the mean velocity of the atoms, and quantifies the decay rate caused by motion as introduced in Eq. 2.8.

For a temperature of $T = 2\,\mu\text{K}$, the average speed for rubidium-87 is $v_{\text{atoms}} = 0.014\,\mu\text{m}/\mu\text{s}$. Therefore, the atoms move approximately $0.4\,\mu\text{m}$ in $20\,\mu\text{s}$, which is a typical timescale for our experiments. This motion must be compared to the wavelength of the stored collective excitation.

For rubidium-87, the direct transition from the $5S$ to the $90P$ Rydberg state results in a spin wave k-vector of $k = 2\pi/297\,\text{nm} = 21\,\mu\text{m}^{-1}$. A two-photon excitation, with two beams with k_1 and k_2 respectively, can tune the effective k-vector $k = k_1 \pm k_2$ in comparison to a single photon excitation, where the $\pm$ stands for co- and counter-propagating photons respectively. Therefore, a counter-propagating scheme should be used to excite the $90S$ Rydberg state via the $5P$ intermediate state. This excitation scheme results in an effective k-vector of $k = 2\pi/480\,\text{nm} - 2\pi/780\,\text{nm} = 5\,\mu\text{m}^{-1}$.

In general, two similar wavelengths are advantageous to reduce the imprinted momentum, which lead to the successful implementations in ground state schemes [18, 43]. For the case of involving Rydberg states, one possibility of minimizing k lies in different atomic species with a favorable spacing of energy levels. One candidate is ytterbium with effective two-photon excitation k-vector of $k = 2\pi/395\,\text{nm} - 2\pi/399\,\text{nm} = 0.2\,\mu\text{m}^{-1}$ [101].

While the effective k-vector can not be changed for a given atomic species, there are ways of reducing the influence of motional dephasing. Motional dephasing can for instance be suppressed by compensating for the phase scrambling that occurs in thermal motion of the atoms [46]. The acquired phase factor of each atom in Eq. 2.5 can be pre-compensated by mapping the initially excited Rydberg state onto a second Rydberg state [102]. The compensation requires a precise timing, and the coherence time is optimized for each specific storage duration.

In case it is not possible to pre-compensate motional dephasing, one can restrict the atomic motion along the direction of the spin wave by an optical standing wave. However, optical traps can lead to differential light shifts on the involved atomic states. This limits the coherence time both for single trapped atoms [103, 104], and for collective excitations [47, 105]. In this thesis, we investigate the influence of confining the atomic ensemble in an optical standing-wave trap. The wavelength of the trapping laser is tuned to a magic value, where differential light shifts between the ground and the Rydberg state are minimized. The trapping potentials for atoms in both states are calculated in the next chapter, and the experimental implementation and performance is discussed in Chapter 5.

CHAPTER 3

Trapping Potentials for Magic Trapping of Ground and Rydberg States

To create a magic trap with minimal differential light shifts, it is essential to know the trapping potentials in the relevant atomic states. In this chapter, we calculate the trapping potentials for an atom in the ground and Rydberg states. We follow the calculation presented in Ref. [60], and calculate the potential for different trap geometries, a running-wave and a standing-wave trap. For both geometries, we discuss and visualize the different contributions to the potential landscape. The potentials discussed in this chapter will later be used to determine the magic wavelength and to compare theoretical predictions with experimental results.

3.1 Atom-Field Interaction

For the calculations presented in this chapter, we treat the atom quantum mechanically and the field classically. First, we introduce the minimal coupling Hamiltonian for a single electron in a scalar potential $\phi(\boldsymbol{r},t)$ and a vector potential $\boldsymbol{A}(\boldsymbol{r},t)$. For our description, we use the Coulomb gauge,[1] which is defined by $\nabla \cdot \boldsymbol{A}(\boldsymbol{r},t) = 0$, and, thereby, $\phi(\boldsymbol{r},t) = 0$.

The Hamiltonian of the Rydberg electron is given by the minimal coupling Hamiltonian of a one-electron atom[2]

$$\hat{H}(t) = \frac{1}{2m_\mathrm{e}}\left(\hat{\boldsymbol{p}}_\mathrm{e} - \frac{e}{c}\boldsymbol{A}(\boldsymbol{r}+\boldsymbol{r}_\mathrm{e},t)\right)^2 + V_\mathrm{c}(\boldsymbol{r}_\mathrm{e}). \tag{3.1}$$

Here, e and m_e are the electron charge and mass, $\hat{\boldsymbol{p}}_e$ the momentum operator of the electron, c the speed of light, $\boldsymbol{A}(\boldsymbol{r},t)$ the laser beam vector potential, and $V_\mathrm{c}(\boldsymbol{r}_\mathrm{e})$ is the core potential. The atom core is located at position $\boldsymbol{r}$ and the single valence electron is at position $\boldsymbol{r}+\boldsymbol{r}_\mathrm{e}$. The core potential is given by the scalar Coulomb potential of the atomic core as $V_\mathrm{c}(\boldsymbol{r}_\mathrm{e}) = e\phi_\mathrm{c}(\boldsymbol{r}_\mathrm{e})$ [108]. In order to find

[1] Also known as radiation [106], velocity [51, 107] or transverse gauge [51].

[2] The light field Hamiltonian is neglected here, because we are only interested in the shift due to the atom-field coupling with respect to the unperturbed eigenenergies. For further reading, see Peter W. Milonni, The Quantum Vacuum (Academic Press, 1993), Section 4.2, p. 115. [108]

solutions to the minimal-coupling Hamiltonian, the first term is multiplied out as

$$\hat{H}(t) = \frac{1}{2m_\mathrm{e}}\left(\hat{\boldsymbol{p}}_\mathrm{e}^2 - \frac{e}{c}\hat{\boldsymbol{p}}_\mathrm{e}\cdot\boldsymbol{A}(\boldsymbol{r}+\boldsymbol{r}_\mathrm{e},t) - \frac{e}{c}\boldsymbol{A}(\boldsymbol{r}+\boldsymbol{r}_\mathrm{e},t)\cdot\hat{\boldsymbol{p}}_\mathrm{e} + \frac{e^2}{c^2}\boldsymbol{A}^2(\boldsymbol{r}+\boldsymbol{r}_\mathrm{e},t)\right) + V_\mathrm{c}(\boldsymbol{r}_\mathrm{e}).$$

The quantum operator $\hat{\boldsymbol{p}}_\mathrm{e}$ and the classical field $\boldsymbol{A}(\boldsymbol{r}+\boldsymbol{r}_\mathrm{e},t)$ commute. Then, the Hamiltonian can be written as

$$\hat{H}(t) = \underbrace{\frac{\hat{\boldsymbol{p}}_\mathrm{e}^2}{2m_\mathrm{e}} + V_\mathrm{c}(\boldsymbol{r}_\mathrm{e})}_{\hat{H}_0} \underbrace{-\frac{e\boldsymbol{A}(\boldsymbol{r}+\boldsymbol{r}_\mathrm{e},t)\cdot\hat{\boldsymbol{p}}_\mathrm{e}}{m_\mathrm{e}c}}_{\hat{H}_1(t)} + \underbrace{\frac{e^2\boldsymbol{A}^2(\boldsymbol{r}+\boldsymbol{r}_\mathrm{e},t)}{2m_\mathrm{e}c^2}}_{\hat{H}_2(t)}. \tag{3.2}$$

The Hamiltonian is now in the form of the hydrogen-like Hamiltonian $\hat{H}_0$ with the terms $\hat{H}_{1,2}(t)$ treated as perturbations periodic in time. These perturbative terms describe the interaction between the atom and the trapping light field.

3.1.1 Dipole Approximation and Atomic Polarizability

The calculation of trapping potentials from the minimal-coupling Hamiltonian in Eq. 3.2 is often performed for ground-state atoms in the dipole approximation [109]. The trapping of particles that are point-like in relation to the optical wavelength is well described for optical dipole traps [110–112]. While optical dipole traps are standard tools for experiments with ultracold ground-state atoms, special care for Rydberg atoms with their larger extent as introduced in Section 2.2. In the following, we summarize how to calculate dynamic polarizabilities and AC Stark shifts in the dipole approximation.

The classical light field is described by a vector potential corresponding to a traveling plane wave with $\boldsymbol{A}(\boldsymbol{r}+\boldsymbol{r}_\mathrm{e},t) \propto \exp(i\boldsymbol{k}\cdot(\boldsymbol{r}+\boldsymbol{r}_\mathrm{e}) - i\omega t) + c.c.$. The wave vector of the trap laser pointing in the x direction is denoted by $\boldsymbol{k} = k\hat{\boldsymbol{e}}_x$, where $\boldsymbol{k} = 2\pi/\lambda$ with the wavelength of the external field λ. Electromagnetic fields with optical frequencies have $1/k \sim 100\,\mathrm{nm}$, and this length scale can be compared to the electron wave function radius for a given atomic state with principal quantum number n. The electron radius $\boldsymbol{r}_\mathrm{e}$ from Eq. 2.11 is about 0.3 nm for a ground-state atom [22]. In this case, $\boldsymbol{k}\cdot\boldsymbol{r}_\mathrm{e} \sim 10^{-3} \ll 1$. Figure 3.1(a) shows the small size of ground-state atoms with respect to an optical wavelength. The vector potential part depending on the electron position $\boldsymbol{r}_\mathrm{e}$ can be expressed as an exponential series, and with the above arguments simplified to

$$\begin{aligned}
\boldsymbol{A}(\boldsymbol{r}+\boldsymbol{r}_\mathrm{e},t) &= \boldsymbol{A}(t)\exp\left(i\boldsymbol{k}\cdot(\boldsymbol{r}+\boldsymbol{r}_\mathrm{e})\right) + c.c. \\
&= \boldsymbol{A}(t)\exp\left(i\boldsymbol{k}\cdot\boldsymbol{r}\right)\left(1 + i\boldsymbol{k}\cdot\boldsymbol{r}_\mathrm{e} + \left[i\boldsymbol{k}\cdot\boldsymbol{r}_\mathrm{e}\right]^2/2 + \dots\right) + c.c. \\
&\simeq \boldsymbol{A}(t)\exp\left(i\boldsymbol{k}\cdot\boldsymbol{r}\right) + c.c. \\
&= \boldsymbol{A}(\boldsymbol{r},t) + c.c.,
\end{aligned}$$

with an asymptotic equality in the second to last step assuming $\boldsymbol{k}\cdot\boldsymbol{r}_\mathrm{e} \ll 1$. This is generally called the dipole approximation or the long-wavelength approximation [113].

In the field of cold atoms, the interaction part of the minimal coupling Hamiltonian in Eq. 3.2 is often simplified in the dipole approximation to the Hamiltonian $\hat{H}^*_\mathrm{int,dip} = -\hat{\boldsymbol{d}}\cdot\boldsymbol{E}$ [112], with the atomic dipole moment $\hat{\boldsymbol{d}} = e\hat{\boldsymbol{r}}_\mathrm{e}$. The derivation is given in Ref. [115, p. 13] and Ref. [106, p. 148], and only briefly outlined here. To begin with, the vector potential $\boldsymbol{A}(\boldsymbol{r},t)$ in the dipole approximation is

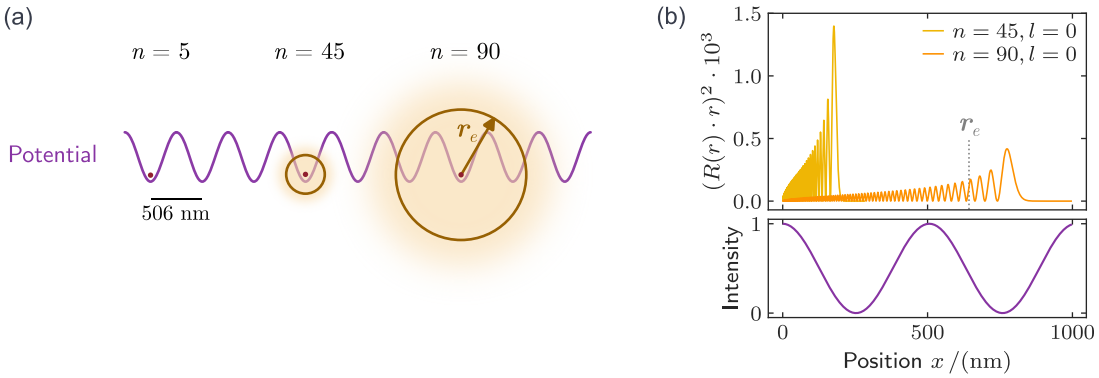

Figure 3.1: Rydberg atoms in a standing wave trap. (a) Atoms in the $n = 5$, $n = 45$, and $n = 90$ state inside a standing wave trap with 506 nm periodicity, corresponding to a wavelength of 1012 nm. The expectation value of the Rydberg electron radius $\langle r \rangle = r_e$ is highlighted. The red dot represents the core. The core size and radius r_e in the ground state $n = 5$ is not to scale with the wavelength. (b) Radial wave function of the Rydberg electron (top) with respect to the standing wave intensity (bottom). Rydberg S-states are shown by solid lines. The Rydberg electron radius for $n = 90$ as defined in the main text is marked as a gray dotted line. Figure (a) adapted from Ref. [114].

used. Then, the terms $\hat{H}_1(t)$ and $\hat{H}_2(t)$ in the minimal coupling Hamiltonian in Eq. 3.2 are given by

$$\hat{H}_{\text{int,dip}}(\boldsymbol{r},t) = -\frac{e\boldsymbol{A}(\boldsymbol{r},t)\cdot\hat{\boldsymbol{p}}_e}{m_e c} + \frac{e^2\boldsymbol{A}^2(\boldsymbol{r},t)}{2m_e c^2}. \tag{3.3}$$

Next, the Power-Zienau transformation [116] given by

$$U = \exp\left[\frac{ie}{\hbar}\boldsymbol{r}_e\cdot\boldsymbol{A}(\boldsymbol{r},t)\right],$$

is performed. The transformed wave functions $\Phi(\boldsymbol{r},t)$ are given by

$$\Psi(\boldsymbol{r}_e,t) = \exp\left[-\frac{ie}{\hbar}\boldsymbol{A}(t)\cdot\boldsymbol{r}_e\right]\Phi(\boldsymbol{r}_e,t).$$

Inserting these wave functions into the Schrödinger equation with the Hamiltonian from Eq. 3.1 and with $\boldsymbol{E}(\boldsymbol{r},t) = -\partial\boldsymbol{A}(\boldsymbol{r},t)/\partial t$, one finds [107]

$$i\hbar\partial\Phi(\boldsymbol{r}_e,t)/\partial t = [\hat{H}_0 \underbrace{-e\hat{\boldsymbol{r}}_e\cdot\boldsymbol{E}(\boldsymbol{r},t)}_{\hat{H}^*_{\text{int,dip}}}]\Phi(\boldsymbol{r}_e,t).$$

Now the electric-dipole interaction Hamiltonian is in the known form of

$$\hat{H}^*_{\text{int,dip}}(\boldsymbol{r},t) = -\hat{\boldsymbol{d}}\cdot\boldsymbol{E}(\boldsymbol{r},t), \tag{3.4}$$

with $\hat{\boldsymbol{d}} = e\hat{\boldsymbol{r}}_e$ as the atomic dipole moment. The two forms $\hat{H}^*_{\text{int,dip}}$ (Eq. 3.4) and $\hat{H}_{\text{int,dip}}$ (Eq. 3.3) are equivalent, provided that both the original and the transformed wave functions are exact solutions to the Schrödinger equation. For ground-state atoms, it turns out to be a good description to consider the

atom having multipoles of different order interacting with the electric field. Therefore, the expansion of the charge distribution in dipole, quadrupole and higher order poles can be used [117].

The interaction Hamiltonian $\hat{H}^{*}_{\mathrm{int,dip}} = -\hat{\boldsymbol{d}} \cdot \boldsymbol{E}(\boldsymbol{r}, t)$ can be related to a dynamic polarizability $\alpha(\omega)$ using the Kramers-Heisenberg formula [109, 118]. The frequency-dependence of $\alpha(\omega)$ arises from the time-varying electric field, and explains the naming as dynamic or AC polarizability. Figure 3.2 shows the dynamic polarizability from Ref. [79] for the ground state $5S_{1/2}$ in rubidium-87. The trapping potential arising from the polarizability is given by [112]

$$U(\boldsymbol{r}) = -\alpha(\omega)\omega^2 |\boldsymbol{A}(\boldsymbol{r})|^2 = -\frac{1}{2}\alpha(\omega)\left\langle |\boldsymbol{E}(\boldsymbol{r}, t)|^2 \right\rangle_t , \tag{3.5}$$

with the time average of the square of the driving electric field over one oscillation period. The positive ground state polarizability in Fig. 3.2 in the near-infrared wavelength range (here $\lambda > 795\,\mathrm{nm}$) creates an attractive trapping potential for ground-state atoms. The dipole trap potential is proportional to $1/\Delta$, whereas the scattering rate scales as $1/\Delta^2$ with the detuning Δ [112]. Therefore, one typically tries to be far detuned, which, although requiring higher laser power, reduces dephasing and heating of the atoms.

In contrast to the ground state, the size of the electron wave function for highly excited Rydberg states can become similar to the laser field wavelength. Figure 3.1(a) visualizes the size difference between states with low and high principal quantum numbers n with respect to a standing wave trapping potential having wavelength $\lambda = 1012\,\mathrm{nm}$. The highlighted most probable electron radius gives an intuitive picture of the "size" of the Rydberg atom. For Rydberg state $45S$, $\boldsymbol{r}_\mathrm{e} \sim 160\,\mathrm{nm}$ and, with $\boldsymbol{k} \cdot \boldsymbol{r}_\mathrm{e} \sim 1$, the dipole approximation becomes invalid. Figure 3.1(b) shows the Rydberg electron radial wave function in comparison to a standing wave intensity distribution. To keep our derivation of trapping potentials applicable for both ground state and high Rydberg states, we do not apply the dipole approximation to the minimal-coupling Hamiltonian in Eq. 3.2.

Far off-resonance, the interaction of high-lying Rydberg states with near-infrared lasers gives rise to a negative polarizability [51]. The value approaches the free-electron polarizability $\alpha_f = -e^2/m_\mathrm{e}\omega^2$ shown in Fig. 3.2 for high principal quantum numbers. This corresponds to the so-called ponderomotive energy shift: although the electric field oscillates with zero time average, the electron undergoes rapid quiver motion, storing kinetic energy on average [119]. This time-averaged energy is the ponderomotive energy. The almost-free electron in Rydberg states experiences this ponderomotive energy shift, and due to the negative sign of the free-electron polarizability, the entire Rydberg atom is repelled by high-intensity laser fields. Therefore, it is common to turn off the dipole trap during experiments to prevent the Rydberg atom from being lost due to this repulsion [49].

The repulsion caused by the ponderomotive energy shift can be mitigated by using a near-resonant trapping field. The focus in this thesis is on the near-resonant coupling between the $6P$ state and high-lying Rydberg states, which is represented by the middle dashed line in Fig. 3.2. At a wavelength of 1012 nm, lasers with output power in the range of watts are commercially available. The remainder of this chapter is dedicated to calculating the energy shift of these Rydberg states due to this coupling.

3.1.2 AC Stark Shift Calculation with Floquet Theory

To calculate the potential without the dipole approximation, we return to Eq. 3.2 and find time-dependent solutions with Floquet theory. The Hamiltonian is in the form of the hydrogen-like Hamiltonian $\hat{H}_0$ with the terms $\hat{H}_{1,2}(t)$ treated as time-dependent perturbations. The eigenstates $\Psi_n^{(0)}$

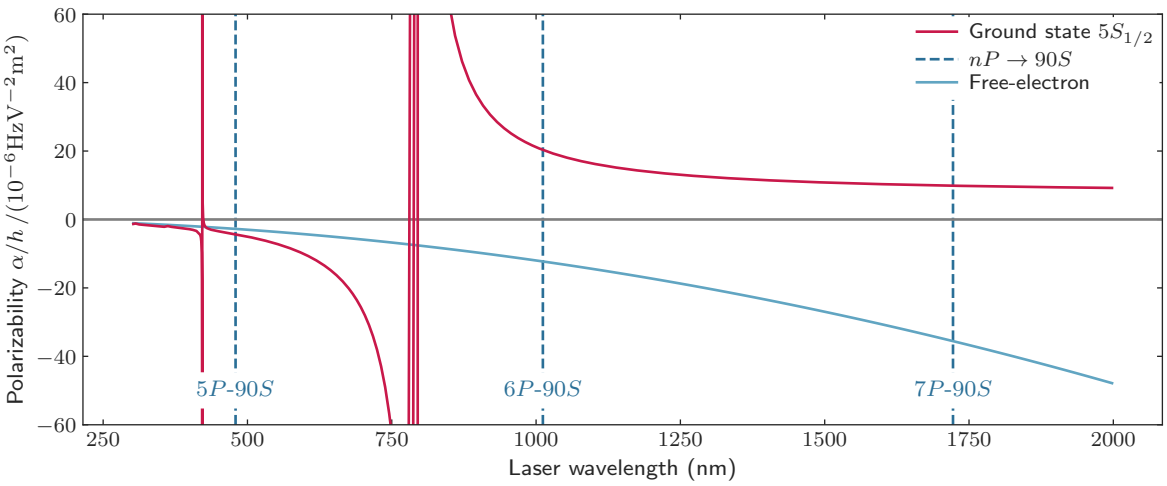

Figure 3.2: Dynamic polarizability for the $5S_{1/2}$ ground state (red, solid) in rubidium-87 as a function of laser wavelength. The transition wavelengths from the Rydberg state $90S_{1/2}$ to the lower-lying $5P_{3/2}$, $6P_{3/2}$ and $7P_{3/2}$ states are indicated by the blue dashed vertical lines. The solid light blue line is the free-electron polarizability $\alpha_f = -e^2/m_e\omega^2$.

and eigenenergies $E_n^{(0)}$ of the unperturbed $\hat{H}_0$ are known [120]. They are solutions to the equation

$$\hat{H}_0\Psi^{(0)} = \left(\frac{\hat{\boldsymbol{p}}_e^2}{2m_e} + V_c(\boldsymbol{r}_e)\right)\Psi^{(0)} = E^{(0)}\Psi^{(0)} \tag{3.6}$$

The core potential $V_c(\boldsymbol{r}_e)$ is derived from model potentials with the corresponding quantum defects for rubidium [51, 121]. This holds in the single active electron approximation, that can be applied for both the ground and Rydberg states. The terms $\hat{H}_1(t)$ and $\hat{H}_2(t)$ are small perturbations and give rise to the energy shift arising from the external laser field. Then, one seeks a solution of the Schrödinger equation of the perturbed Hamiltonian

$$i\hbar\frac{\partial\Psi}{\partial t} = [\hat{H}_0 + \hat{H}_1(t) + \hat{H}_2(t)]\Psi \tag{3.7}$$

The laser field is periodic in time, which makes the two perturbations periodic in time. In other words, the time dependence of the vector potential $\boldsymbol{A}(\boldsymbol{r} + \boldsymbol{r}_e, t)$ requires time-dependent perturbation theory to solve the Schrödinger equation. We use the Floquet quasi-energy approach to find the energy corrections [122, 123].

In the following, a recipe for applying the Floquet quasi-energy approach to a time-dependent perturbation problem is given. The recipe summarizes the calculation given in Ref. [115, p. 22]. More details on the calculation can also be found in Ref. [114]. First, the solutions for a time-independent perturbation are stated. These energy corrections are extended in the Floquet approach to include the time dependence. The total energy correction for state q arising from a perturbation Hamiltonian $\hat{G}$ is

given in Ref. [124, p. 130, 131] as

$$\begin{aligned}\delta E_q &= E_q^{(1)} + E_q^{(2)},\\ &= \langle q|\hat{G}|q\rangle + \sum_{j\neq q} \frac{\left|\langle q|\hat{G}|j\rangle\right|^2}{E_q^{(0)} - E_j^{(0)}}.\end{aligned}$$

Next, the energy corrections from the time-dependent perturbation $\hat{G}(t)$ are calculated. For this purpose, the unperturbed energies $E_q^{(0)}$ for state q are replaced with the quasi-energies $E_q^{(0)} + m\hbar\omega$, where m is an integer. The dipole matrix elements are not only integrated over space, but also averaged over one oscillation period $T = 2\pi/\omega$. The energy corrections are finally derived as

$$E_q^{(1)} = \sum_m \int_0^{\frac{2\pi}{\omega}} \langle q|\hat{G}_m(t)|q\rangle\, dt, \tag{3.8}$$

$$E_q^{(2)} = \sum_{j\neq q,m} \int_0^{\frac{2\pi}{\omega}} \frac{\left|\langle q|\hat{G}_m(t)|j\rangle\right|^2}{E_q^{(0)} - E_j^{(0)} - m\hbar\omega} dt, \tag{3.9}$$

where the time dependent Hamiltonian $\hat{G}(t)$ is decomposed into Fourier components $\hat{G}_m(t)$ and the trapping laser has frequency ω. For an external field from a trapping laser, the perturbation Hamiltonian is periodic in time $T = 2\pi/\omega$. According to the quasi-energy method [122, p. 331], the periodicity is decomposed into oscillation components $\exp(im\omega t)$ with integer multiple $m = 0, \pm1, \pm2, \ldots$.

This recipe can now be applied to calculate the energy corrections arising from a trap laser field.

3.1.3 Energy Corrections

In this section, we calculate the two energy corrections arising from the $\boldsymbol{A}(\boldsymbol{r}+\boldsymbol{r}_\mathrm{e}, t)\cdot\hat{\boldsymbol{p}}_\mathrm{e}$ and $\boldsymbol{A}^2(\boldsymbol{r}+\boldsymbol{r}_\mathrm{e}, t)$ term, respectively.

We first calculate the energy correction $U_\mathrm{q}^{(1)}(\boldsymbol{r})$ due to the time-dependent perturbation Hamiltonian $\hat{H}_1(t)$. The Hamiltonian is of the form $\boldsymbol{A}(\boldsymbol{r}+\boldsymbol{r}_\mathrm{e}, t)\cdot\hat{\boldsymbol{p}}_\mathrm{e}$. The energy correction from Eq. 3.8 is equal to zero for this Hamiltonian, as the vector potential $\boldsymbol{A}(\boldsymbol{r}+\boldsymbol{r}_\mathrm{e}, t)$ averages out over one oscillation period.

To calculate the second order energy correction, the vector potential $\boldsymbol{A}(\boldsymbol{r}+\boldsymbol{r}_\mathrm{e}, t)$ can be expanded as a series with factors of $\exp(im\omega t)$. The $m = \pm1$ components, $\exp(i\omega t) + \exp(-i\omega t)$, describe our sinusoidal laser field exactly and no other orders have to be considered. The Hamiltonian reduces to

$$\hat{H}_1(t) = \frac{e\boldsymbol{A}(\boldsymbol{r}+\boldsymbol{r}_\mathrm{e})\cdot\hat{\boldsymbol{p}}_\mathrm{e}}{m_\mathrm{e}c} e^{i\omega t} + \frac{e\boldsymbol{A}^*(\boldsymbol{r}+\boldsymbol{r}_\mathrm{e})\cdot\hat{\boldsymbol{p}}_\mathrm{e}}{m_\mathrm{e}c} e^{-i\omega t}. \tag{3.10}$$

With Eq. 3.9, this Hamiltonian results in an energy correction for state q given by

$$U_q^{(1)}(\boldsymbol{r}) \approx \frac{e^2}{m_\mathrm{e}^2} \sum_{j\neq q} \frac{1}{\hbar} \left(\frac{\left|\langle q|\boldsymbol{A}(\boldsymbol{r}+\boldsymbol{r}_\mathrm{e})\cdot\boldsymbol{p}_\mathrm{e}|j\rangle\right|^2}{\omega_{qj} - \omega} + \frac{\left|\langle q|\boldsymbol{A}^*(\boldsymbol{r}+\boldsymbol{r}_\mathrm{e})\cdot\boldsymbol{p}_\mathrm{e}|j\rangle\right|^2}{\omega_{qj} + \omega} \right). \tag{3.11}$$

Here, the matrix elements evaluate the electron wave function overlap of the two atomic states $|q\rangle$ and $|j\rangle$ with respect to the spatially varying vector potential. In order to simplify these matrix elements,

the vector potential can be expanded as a Taylor series for a small electron radius $\boldsymbol{r}_\mathrm{e}$ [125] as

$$\boldsymbol{A}(\boldsymbol{r}+\boldsymbol{r}_\mathrm{e}) = \boldsymbol{A}(\boldsymbol{r}) + \boldsymbol{r}_\mathrm{e}\cdot\nabla_{\boldsymbol{r}}\boldsymbol{A}(\boldsymbol{r}) + \frac{1}{2}\sum_{i,j} r_i r_j \frac{\partial^2 \boldsymbol{A}}{\partial r_i \partial r_j}(\boldsymbol{r}) + \dots \tag{3.12}$$

With this expansion, the expectation values are expressed in terms of the wave function overlap between the two states q and j as

$$\begin{aligned}\langle q|\boldsymbol{A}(\boldsymbol{r}+\boldsymbol{r}_\mathrm{e})\cdot\hat{\boldsymbol{p}}_\mathrm{e}|j\rangle &= \int \Psi_q^*(\boldsymbol{r})\boldsymbol{A}(\boldsymbol{r}+\boldsymbol{r}_\mathrm{e})\cdot\hat{\boldsymbol{p}}_\mathrm{e}\Psi_j(\boldsymbol{r})\,d\boldsymbol{r}\\ &= \int \Psi_q^*(\boldsymbol{r})\boldsymbol{A}(\boldsymbol{r})\cdot\hat{\boldsymbol{p}}_\mathrm{e}\Psi_j(\boldsymbol{r})\,d\boldsymbol{r}\\ &+ \int \Psi_q^*(\boldsymbol{r})(\boldsymbol{r}_\mathrm{e}\cdot\nabla_{\boldsymbol{r}}\boldsymbol{A}(\boldsymbol{r}))\cdot\hat{\boldsymbol{p}}_\mathrm{e}\Psi_j(\boldsymbol{r})\,d\boldsymbol{r}\\ &+ \dots\end{aligned}$$

In these terms, the contribution of the vector potential is evaluated on the scale of the two involved wave functions Ψ_q and Ψ_j. The sum in Eq. 3.11 has to be calculated by considering all possible states.

Figure 3.3(a), (b) and (c) depict the expansion of the vector potential and the respective matrix element for low- and high-lying atomic states. This visualization is meant to give the reader a size comparison of the involved wave functions and optical wavelength.

For the ground state in Fig. 3.3(a), the wave function sizes are much smaller than the laser wavelength. The vector potential is evaluated in a small range and is in the dipole approximation independent of the electron position.

Rydberg states, that are larger than the ground state, would sample the variation of the vector potential. The overlap in Fig. 3.3(b) between Rydberg states (large electron wave function) and low-lying states (small electron wave function) is still small, because the smaller wave function determines the relevant spatial volume. For this reason, the dipole approximation can also be applied for optical excitations into Rydberg states. The higher order terms depicted by the gradient and curvature are negligible, because of the vanishing variation of the vector potential in the overlap region.

The vector potential variation in the overlap between two Rydberg state in Fig. 3.3(c) is not vanishing. However, the transition frequency between Rydberg states lies in the microwave range [22] and the denominator in Eq. 3.11 suppresses these contributions. Figure 3.3(d) shows the binding energy of atomic states in rubidium-87, as well as the energy carried by a single photon with a wavelength of 1012 nm.

With these arguments, it is sufficient to consider the first term in Eq. 3.12. The energy correction

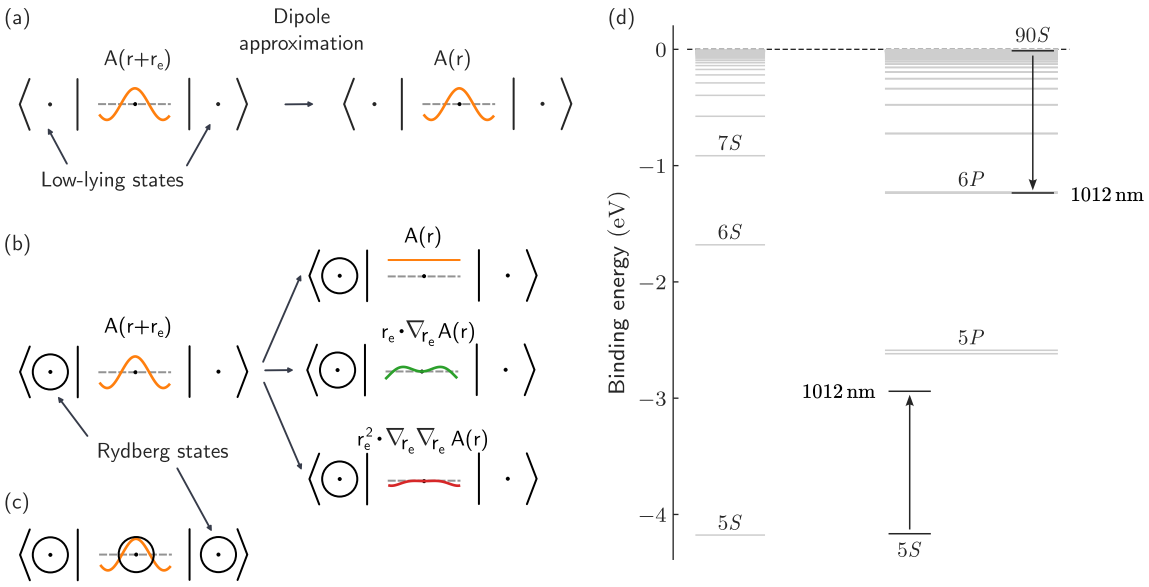

Figure 3.3: (a), (b) and (c) Symbolic representation of matrix elements with a wave function overlap across the vector potential $\boldsymbol{A}(\boldsymbol{r}+\boldsymbol{r}_\mathrm{e})$. The bra and ket states are atomic states. The dots represent the wave function of low-lying states and the large circles the ones of Rydberg states. (a) For two low-lying states, the field does not vary over either of the two electron wave functions and the dipole approximation is valid. (b) The vector potential is expanded into a constant, a gradient and a curvature contribution according to Eq. 3.12. The small black dot in the vector potential depictions shows the size of the smaller of the two involved wave function with respect to the wavelength. (c) The overlap calculation between two Rydberg states. (d) Binding energy of nS and nP levels in rubidium-87 (gray horizontal lines). The vertical black arrows have a length on the energy scale corresponding to the trap laser wavelength of ~ 1012 nm. The black vertical lines mark the energies reached from the states $5S$ and $90S$ respectively by coupling with one trap photon. For the $5S$ ground state, the main contribution to the sum in Eq. 3.24 is from the $5P$ states. The trap wavelength is chosen such that the example Rydberg state $90S$ is coupled to the low-lying $6P$ state.

can therefore be simplified to

$$\begin{aligned} U_q^{(1)}(\boldsymbol{r}) =& \frac{e^2}{\hbar m_\mathrm{e}^2} \sum_{j\neq q} \left(\frac{|\langle q|\boldsymbol{A}(\boldsymbol{r})\cdot\boldsymbol{p}_\mathrm{e}|j\rangle|^2}{\omega_{qj}-\omega} + \frac{\left|\langle q|\boldsymbol{A}^*(\boldsymbol{r})\cdot\boldsymbol{p}_\mathrm{e}|j\rangle\right|^2}{\omega_{qj}+\omega} \right) \\ &+ \frac{e^2}{\hbar m_\mathrm{e}^2} \sum_{j\neq q} \left(\frac{|\langle q|(\nabla_{\boldsymbol{r}}\boldsymbol{A}(\boldsymbol{r})\cdot\boldsymbol{r}_\mathrm{e})\cdot\boldsymbol{p}_\mathrm{e}|j\rangle|^2}{\omega_{qj}-\omega} + \frac{\left|\langle q|(\nabla_{\boldsymbol{r}}\boldsymbol{A}^*(\boldsymbol{r})\cdot\boldsymbol{r}_\mathrm{e})\cdot\boldsymbol{p}_\mathrm{e}|j\rangle\right|^2}{\omega_{qj}+\omega} \right) + \dots \\ \approx& \frac{e^2}{\hbar m_\mathrm{e}^2} \sum_{j\neq q} \left(\frac{|\langle q|\boldsymbol{A}(\boldsymbol{r})\cdot\boldsymbol{p}_\mathrm{e}|j\rangle|^2}{\omega_{qj}-\omega} + \frac{\left|\langle q|\boldsymbol{A}^*(\boldsymbol{r})\cdot\boldsymbol{p}_\mathrm{e}|j\rangle\right|^2}{\omega_{qj}+\omega} \right). \end{aligned} \tag{3.13}$$

Together with $\boldsymbol{A}(\boldsymbol{r}) = \boldsymbol{\epsilon}A(\boldsymbol{r})$ and the commutation identity of the hydrogen atom [126] $\langle r|\boldsymbol{\epsilon}\cdot\boldsymbol{p}_\mathrm{e}|j\rangle =$

$im_e\omega_{rj}\langle r|e\,\boldsymbol{\epsilon}\cdot\boldsymbol{r}_e|j\rangle$, one can write the energy correction in the first term of the series expansion as

$$U_q^{(1)}(\boldsymbol{r}) = -|\boldsymbol{A}(\boldsymbol{r})|^2\omega^2\left[-\sum_{j\neq q}\frac{\omega_{qj}^2}{\omega^2}\left(\frac{|\langle q|e\boldsymbol{\epsilon}\cdot\boldsymbol{r}_e|j\rangle|^2}{\hbar(\omega_{qj}-\omega)}+\frac{\left|\langle q|e\boldsymbol{\epsilon}^*\cdot\boldsymbol{r}_e|j\rangle\right|^2}{\hbar(\omega_{qj}+\omega)}\right)\right] \tag{3.14}$$

This equation will be evaluated for the ground and Rydberg states in the following section.

Next, we evaluate the energy correction for the perturbation Hamiltonian $\hat{H}_2(t)\propto\boldsymbol{A}^2(\boldsymbol{r}+\boldsymbol{r}_e,t)$ expressed in Floquet modes with the derived energy correction $U_q^{(2)}(\boldsymbol{r})$ for time-dependent perturbation in Eq. 3.8 and 3.9. In contrast to the $\boldsymbol{A}(\boldsymbol{r}+\boldsymbol{r}_e,t)\cdot\hat{\boldsymbol{p}}_e$ term, the first-order perturbation does not vanish. Furthermore, we consider only the first order as it is already proportional to $\boldsymbol{A}^2(\boldsymbol{r})$, which is also the case for the contribution from the $\boldsymbol{A}(\boldsymbol{r}+\boldsymbol{r}_e,t)\cdot\hat{\boldsymbol{p}}_e$ term in Eq. 3.14. With the first-order perturbation, the energy correction $U_q^{(2)}(\boldsymbol{r})$ is given by

$$\begin{aligned}U_q^{(2)}(\boldsymbol{r}) &\approx \frac{e^2}{2m_e}\left\langle q|2\boldsymbol{A}(\boldsymbol{r}+\boldsymbol{r}_e)\boldsymbol{A}^*(\boldsymbol{r}+\boldsymbol{r}_e)|q\right\rangle\\ &= -\alpha_f\omega^2\left\langle q|\boldsymbol{A}(\boldsymbol{r}+\boldsymbol{r}_e)\boldsymbol{A}^*(\boldsymbol{r}+\boldsymbol{r}_e)|q\right\rangle,\end{aligned} \tag{3.15}$$

where $\alpha_f=-e^2/m_e\omega^2$ is the free-electron polarizability. The expectation value has to be evaluated for the wave function of the respective state q. For both the ground and the Rydberg state, the energy correction in Eq. 3.15 is proportional to the free-electron polarizability. It has to be noted that the free-electron polarizability α_f is generally associated with the almost-free electron in Rydberg atoms [50]. The free-electron polarizability has a non-negligible contribution for the ground state due to our specific gauge choice. Nevertheless, the total value of the ground state polarizability is the same independent of the gauge choice. In Appendix A, we reformulate our result of the polarizabilities in Eq. 3.14 and Eq. 3.15 to a single sum over coupled states, as it is often given in the literature [59, 112, 113, 127]. To calculate how much the free-electron polarizability contributes to the total energy correction of the ground and the Rydberg state respectively, one has to consider the exact shape of the vector potential $\boldsymbol{A}(\boldsymbol{r}+\boldsymbol{r}_e)$ in Eq. 3.15.

3.2 Running- and Standing-Wave Traps

In this section, the vector potentials for the running- and standing-wave trap, as realized in the experiment, are given. Afterward, the vector potentials are used to calculate the trapping potentials for atoms in the ground and Rydberg states. This theoretical chapter concludes with a general discussion about trapping potential dependence on the principal quantum number n.

3.2.1 Explicit Vector Potential

The derivations in Section 3.1.3 were for a general vector potential $\boldsymbol{A}(\boldsymbol{r}+\boldsymbol{r}_e,t)$. Here, we present the vector potentials for the optical beam arrangement in the experiment. Figure 3.4 shows the running-wave and the standing-wave trap, and their implementation in the experimental setup is later discussed in Chapter 5. The running-wave trap is formed by a single laser beam propagating along the x direction. A second, counter-propagating beam results in the standing-wave trapping potential.

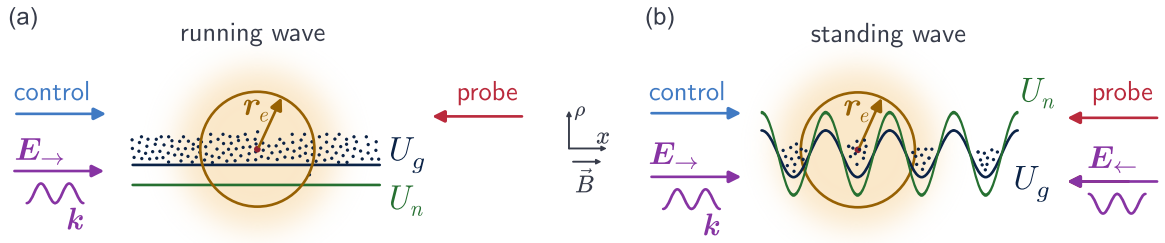

Figure 3.4: Optical beam arrangement for the (a) running- and (b) standing-wave trap experiments. The atoms are trapped in a running wave, which is made by the incoming electric field amplitude $\boldsymbol{E}_{\rightarrow}$. The standing wave trap is created by a counter-propagating beam with $\boldsymbol{E}_{\leftarrow}$. The derivation of the trapping potential for the ground state U_g and the Rydberg state U_n is described in the rest of this chapter. The counter-propagating probe and control light create the collective Rydberg excitations introduced in the previous chapter. Figure adapted from Ref. [1].

The beams in the experiment are Gaussian beams, and their electric field is given by

$$\boldsymbol{E}(\rho,x) = E_0\boldsymbol{\epsilon}\frac{w_0}{w(x)}\exp\left(\frac{-\rho^2}{w^2(x)}\right)\exp\left(-ikx - k\frac{r^2}{2R(z)} + \phi_{\mathrm{G}}(z)\right), \tag{3.16}$$

where $\boldsymbol{\epsilon}$ is the polarization vector, and $k = 2\pi/\lambda$ is the wave vector for wavelength λ. The Gaussian beam waist $w(x)$ is given by

$$w(x) = w_0\sqrt{1+\left(\frac{x}{x_{\mathrm{R}}}\right)^2}, \tag{3.17}$$

and the Rayleigh range x_{R} is defined as

$$x_{\mathrm{R}} = \frac{\pi w_0^2}{\lambda}.$$

For our experiment, the radius of curvature $R(z)$ and the Gouy phase $\phi_{\mathrm{G}}(z)$ can be neglected, as the atoms reside only in the central part of the trap with positions x much smaller than the Rayleigh range x_{R}.

The vector potential for the two counter propagating beams is given by

$$\begin{aligned}\boldsymbol{A}(\boldsymbol{r}+\boldsymbol{r}_{\mathrm{e}},t) = \frac{\boldsymbol{\epsilon}}{\omega}\Big(&E_{\rightarrow}(\boldsymbol{r})\sin\left((\boldsymbol{r}+\boldsymbol{r}_{\mathrm{e}})\cdot\boldsymbol{k}-\omega t\right)\\ &-E_{\leftarrow}(\boldsymbol{r})\sin\left((\boldsymbol{r}+\boldsymbol{r}_{\mathrm{e}})\cdot\boldsymbol{k}+\omega t\right)\Big),\end{aligned} \tag{3.18}$$

where the arrows denote the in-coming ($\rightarrow$) and the retro-reflected ($\leftarrow$) beam. The resulting electric field in the Coulomb gauge is defined as $\boldsymbol{E}(\boldsymbol{r},t) = -\partial\boldsymbol{A}(\boldsymbol{r},t)/\partial t$ and given by

$$\begin{aligned}\boldsymbol{E}(\boldsymbol{r}+\boldsymbol{r}_{\mathrm{e}},t) = \boldsymbol{\epsilon}\Big(&E_{\rightarrow}(\boldsymbol{r})\cos\left((\boldsymbol{r}+\boldsymbol{r}_{\mathrm{e}})\cdot\boldsymbol{k}-\omega t\right)\\ &+E_{\leftarrow}(\boldsymbol{r})\cos\left((\boldsymbol{r}+\boldsymbol{r}_{\mathrm{e}})\cdot\boldsymbol{k}+\omega t\right)\Big),\end{aligned} \tag{3.19}$$

where $\boldsymbol{k} = k\hat{\boldsymbol{e}}_x$ is the wave vector of the trap laser propagating along the x-axis. In our experiments, the electric field amplitudes do not vary over the size of the Rydberg atom, and we set $E_{\rightarrow(\leftarrow)}(\boldsymbol{r}+\boldsymbol{r}_{\mathrm{e}}) \approx$

$E_{\rightarrow(\leftarrow)}(\boldsymbol{r})$. The electric field amplitudes are Gaussian envelopes defined as

$$E_{\rightarrow(\leftarrow)}(\boldsymbol{r}) = E_{\rightarrow(\leftarrow)}(\rho, x) = E_{0,\rightarrow(\leftarrow)} \frac{w_0}{w(x)} \exp\left(-\rho^2/w^2(x)\right). \tag{3.20}$$

The two electric field amplitudes $E_{\rightarrow(\leftarrow)}(\boldsymbol{r})$ are denoted with the arrows for the in-coming ($\rightarrow$) and the retro-reflected ($\leftarrow$) beam. The positions are expressed in cylindrical coordinates with radius ρ and axial position x, as the further analysis will focus on the radial and axial trapping beam shapes.

We express the vector potential as a time-dependent and a time-independent part to solve the time-dependent perturbation theory with the Floquet quasi-energy approach from Section 3.1.2. The vector potential in Eq. 3.18 can be written as

$$\boldsymbol{A}(\boldsymbol{r} + \boldsymbol{r}_\mathrm{e}, t) = \boldsymbol{A}(\boldsymbol{r} + \boldsymbol{r}_\mathrm{e}) e^{-i\omega t} + \boldsymbol{A}^*(\boldsymbol{r} + \boldsymbol{r}_\mathrm{e}) e^{i\omega t},$$

with the time-independent vector potential

$$\boldsymbol{A}(\boldsymbol{r} + \boldsymbol{r}_\mathrm{e}) = \boldsymbol{\epsilon} \left(\frac{(E_\rightarrow(\boldsymbol{r}) - E_\leftarrow(\boldsymbol{r}))}{2\omega} \sin\left(\boldsymbol{k}(\boldsymbol{r} + \boldsymbol{r}_\mathrm{e})\right) - \frac{i(E_\rightarrow(\boldsymbol{r}) + E_\leftarrow(\boldsymbol{r}))}{2\omega} \cos\left(\boldsymbol{k}(\boldsymbol{r} + \boldsymbol{r}_\mathrm{e})\right) \right). \tag{3.21}$$

It follows, that the squared time-independent vector potential is given by

$$\begin{aligned} 4\omega^2 |\boldsymbol{A}(\boldsymbol{r} + \boldsymbol{r}_\mathrm{e})|^2 =& E_\rightarrow(\boldsymbol{r})^2 + E_\leftarrow(\boldsymbol{r})^2 + 2E_\rightarrow(\boldsymbol{r}) E_\leftarrow(\boldsymbol{r}) \cos(2\boldsymbol{k}\boldsymbol{r}_\mathrm{e}) \cos(2\boldsymbol{k}\boldsymbol{r}) \\ & - 4E_\rightarrow(\boldsymbol{r}) E_\leftarrow(\boldsymbol{r}) \sin(2\boldsymbol{k}\boldsymbol{r}_\mathrm{e}) \sin(\boldsymbol{k}\boldsymbol{r}) \cos(\boldsymbol{k}\boldsymbol{r}). \end{aligned} \tag{3.22}$$

This squared vector potential can be used to evaluate the light shift calculated in the previous section (Eq. 3.14 and Eq. 3.15) as well as the well-known AC Stark shift in Eq. 3.5.

3.2.2 Trapping Potentials for the Ground and the Rydberg State

To calculate the energy shift for the ground state, we set $|q\rangle = |g\rangle$ in Eq. 3.14 and 3.15. Furthermore, the ground state allows us to apply the dipole approximation with $k x_\mathrm{e} \ll 1$.

The energy shift for the ground state $U_g^{(1)}(\boldsymbol{r})$ and $U_g^{(2)}(\boldsymbol{r})$, from the $\boldsymbol{A}(\boldsymbol{r}+\boldsymbol{r}_\mathrm{e}, t)\cdot\hat{\boldsymbol{p}}_\mathrm{e}$ and $\boldsymbol{A}^2(\boldsymbol{r}+\boldsymbol{r}_\mathrm{e}, t)$ term respectively, can be written as

$$U_g^{(1)}(\boldsymbol{r}) = -|\boldsymbol{A}(\boldsymbol{r})|^2 \omega^2 \cdot \underbrace{\left[-\sum_{j\neq g} \frac{\omega_{gj}^2}{\omega^2} \frac{1}{\hbar} \left(\frac{|\langle g|e\,\boldsymbol{\epsilon}\cdot\boldsymbol{r}_\mathrm{e}|j\rangle|^2}{\omega_{gj} - \omega} + \frac{\left|\langle g|e\,\boldsymbol{\epsilon}^*\cdot\boldsymbol{r}_\mathrm{e}|j\rangle\right|^2}{\omega_{gj} + \omega} \right) \right]}_{\text{dynamic polarizability } \alpha_g^{(1)}(\omega)} \tag{3.23}$$

$$\begin{aligned} U_g^{(2)}(\boldsymbol{r}) &\approx -\alpha_f \omega^2 \left\langle g|\boldsymbol{A}(\boldsymbol{r})\boldsymbol{A}^*(\boldsymbol{r})|g\right\rangle \\ &= -\alpha_f \omega^2 |\boldsymbol{A}(\boldsymbol{r})|^2. \end{aligned} \tag{3.24}$$

The sum over all contributing states in $U_g^{(1)}(\boldsymbol{r})$ can be combined in the dynamic polarizability $\alpha_g^{(1)}(\omega)$. It has to be noted, that this is not the total dynamic polarizability of the ground-state atom. There is an additional contribution from the $\boldsymbol{A}^2(\boldsymbol{r} + \boldsymbol{r}_\mathrm{e}, t)$ term. The expectation value in Eq. 3.15 is simplified in the dipole approximation and the squared vector potential in Eq. 3.24 is independent of the electron

position.

From the two contributions above, the total energy shift of the ground state is given by

$$\begin{aligned} U_g(\boldsymbol{r}) &= U_g^{(1)}(\boldsymbol{r}) + U_g^{(2)}(\boldsymbol{r}) \\ &= -\underbrace{[\alpha_g^{(1)}(\omega) + \alpha_f(\omega)]}_{\alpha_g(\omega)}\omega^2 |\boldsymbol{A}(\boldsymbol{r})|^2. \end{aligned}$$

The energy shift is proportional to the dynamic polarizability of the ground-state atom $\alpha_g(\omega)$ as discussed in Section 3.1.1. The dynamic polarizability of the ground-state atom $\alpha_g(\omega)$ has a contribution from the free-electron polarizability as discussed in Section 3.1.3 and Appendix A.

To write the energy shift for the running and standing wave configuration, we use the explicit vector potential $\boldsymbol{A}(\boldsymbol{r} + \boldsymbol{r}_e)$ given in Eq. 3.22 with $\boldsymbol{r}_e \approx 0$. The potentials can be separated into the axially periodic potential $U_g^{\sim}(\boldsymbol{r})$, labeled with ~, and the axially nonperiodic potential $U_g^{-}(\boldsymbol{r})$, labeled with –. For the ground state, the trapping potential is given by

$$U_g(\boldsymbol{r}) \approx U_g^{\sim}(\boldsymbol{r}) + U_g^{-}(\boldsymbol{r}), \tag{3.25}$$

$$U_g^{\sim}(\boldsymbol{r}) = -\alpha_g(\omega) E_{\rightarrow}(\boldsymbol{r}) E_{\leftarrow}(\boldsymbol{r}) \cos^2(kx), \tag{3.26}$$

$$U_g^{-}(\boldsymbol{r}) = -\frac{\alpha_g(\omega)}{4}\Big(E_{\rightarrow}(\boldsymbol{r}) - E_{\leftarrow}(\boldsymbol{r})\Big)^2. \tag{3.27}$$

The periodic potential $U_g^{\sim}(\boldsymbol{r})$ is characterized by the cosine-squared modulation along the propagation axis as typical for standing-wave lattices. To understand the dynamics of the ground-state atoms in Eq. 3.26, each standing-wave potential well can be treated in a harmonic approximation as [128]

$$V_{\mathrm{ax}} = \frac{1}{2}\beta x^2,$$

where β is the harmonic spring constant. The motion of the atoms is characterized by the axial trapping frequency ν_{ax}, which is derived from the spring constant as

$$\nu_{\mathrm{ax}} = \frac{1}{2\pi}\sqrt{\frac{\beta}{m_{\mathrm{Rb}}}} = \sqrt{\frac{2U_0^{\sim}}{m_{\mathrm{Rb}}\lambda^2}}, \tag{3.28}$$

where m_{Rb} is the mass of one rubidium atom, $U_0^{\sim} = \alpha_g(\omega) E_{\rightarrow}(0) E_{\leftarrow}(0)$ is the center trap depth in the periodic potential, and λ is the trap laser wavelength. An imbalance between the incoming and retro-reflected beam powers leads to the nonperiodic potential $U_g^{-}(\boldsymbol{r})$.

To calculate the energy shift of the Rydberg state, we set $|q\rangle = |n\rangle$ in Eq. 3.14 and Eq. 3.15. Here, n specifies the Rydberg state principal quantum number. The trap laser wavelength can be tuned close to an atomic resonance as discussed in Section 3.1.1. In our experiment, we consider a near-resonant trap between a Rydberg state $|n\rangle$ and the state $|a\rangle = \left|6P_{3/2}\right\rangle$ in rubidium-87. The transition frequency ω_{an} depends on the specific Rydberg state. The contribution from the $6P_{3/2}$ state in the sum of Eq. 3.14 is larger by three orders of magnitude compared to all other sum parts combined. For our experiment $\omega_{an} + \omega \gg \omega_{an} - \omega$, the rotating-wave approximation is therefore valid and only the term with $\omega_{an} - \omega$ in Equation 3.14 has to be considered. The energy correction $U_n^{(1)}(\boldsymbol{r})$ of the Rydberg state can be

simplified to

$$U_n^{(1)}(\boldsymbol{r}) \approx |\boldsymbol{A}(\boldsymbol{r})|^2 \frac{\omega_{an}^2}{\hbar} \frac{|\langle n|e\,\boldsymbol{\epsilon}\cdot\boldsymbol{r}_\mathrm{e}|a\rangle|^2}{\omega_{an}-\omega},$$
$$\approx -\omega^2 |\boldsymbol{A}(\boldsymbol{r})|^2 \frac{|\langle n|e\,\boldsymbol{\epsilon}\cdot\boldsymbol{r}_\mathrm{e}|a\rangle|^2}{\hbar\Delta}.$$

Here, we defined the detuning $\Delta = \omega - \omega_{an}$ and set $\omega_{an}^2 \approx \omega^2$. For our trap laser with circular polarization $\boldsymbol{\epsilon}$, the dipole matrix element is given in terms of the reduced dipole matrix element D_{an} by

$$\begin{aligned}|\langle n|e\,\boldsymbol{\epsilon}\cdot\boldsymbol{r}_\mathrm{e}|a\rangle|^2 &= \left|\left\langle n\left|\frac{e}{\sqrt{2}}(\hat{\boldsymbol{e}}_x + i\hat{\boldsymbol{e}}_y)\cdot\boldsymbol{r}_\mathrm{e}\right|a\right\rangle\right|^2 \\ &=: \frac{1}{2}\left|\frac{1}{2}\langle nS_{1/2}, J=1/2||d||6P_{3/2}, J=3/2\rangle\right|^2 \\ &=: \frac{1}{8}D_{an}^2,\end{aligned}$$

with the unit vectors $\hat{\boldsymbol{e}}_x$ and $\hat{\boldsymbol{e}}_y$. The reduced dipole matrix element $D_{an} = \langle a||e\boldsymbol{r}_\mathrm{e}||n\rangle$ are evaluated with the ARC python package [79]. The resulting energy shift for the Rydberg state from the Hamiltonian $\hat{H}_1(t)$ is given by

$$U_n^{(1)}(\boldsymbol{r}) \approx -\frac{D_{an}^2}{8\hbar\Delta}\omega^2|\boldsymbol{A}(\boldsymbol{r})|^2. \tag{3.29}$$

For a linearly polarized trap, as in Ref. [60], the energy shift has a prefactor of $1/12$ instead of $1/8$ due to different angular parts in the dipole matrix elements $\langle n|e\,\boldsymbol{\epsilon}\cdot\boldsymbol{r}_\mathrm{e}|a\rangle$.

The energy shift from the $\boldsymbol{A}^2(\boldsymbol{r}+\boldsymbol{r}_\mathrm{e},t)$ term in Eq. 3.15 can be calculated with the explicit vector potential in Eq. 3.22 as

$$\begin{aligned}U_n^{(2)}(\boldsymbol{r}) \approx -\frac{\alpha_f}{4}\Big[&4E_{\rightarrow}(\boldsymbol{r})E_{\leftarrow}(\boldsymbol{r})\cos^2(kx)\,\langle n|\cos(2kx_\mathrm{e})|n\rangle \\ &- 2E_{\rightarrow}(\boldsymbol{r})E_{\leftarrow}(\boldsymbol{r})\sin(2kx)\,\langle n|\sin(2kx_\mathrm{e})|n\rangle \\ &+ 2E_{\rightarrow}(\boldsymbol{r})E_{\leftarrow}(\boldsymbol{r})\left[1-\langle n|\cos(2kx_\mathrm{e})|n\rangle\right] \\ &+ \Big(E_{\rightarrow}(\boldsymbol{r}) - E_{\leftarrow}(\boldsymbol{r})\Big)^2\Big]\end{aligned}$$

The expectation value $\langle n|\sin(2kx_\mathrm{e})|n\rangle$ vanishes, because the sine function is an odd function. To describe the spatial variance of the wave functions compared to the optical wavelength sketched in Fig. 3.1(b), the landscape factor $\theta_n = \langle n|\cos(2kx_\mathrm{e})|n\rangle$ [51, 60] can be introduced. The energy shift is

simplified to

$$U_n^{(2)}(\boldsymbol{r}) = -\frac{\alpha_f}{4}\Big[4E_{\rightarrow}(\boldsymbol{r})E_{\leftarrow}(\boldsymbol{r})\cos^2(kx)\theta_n + 2E_{\rightarrow}(\boldsymbol{r})E_{\leftarrow}(\boldsymbol{r})\left[1-\theta_n\right] + \Big(E_{\rightarrow}(\boldsymbol{r}) - E_{\leftarrow}(\boldsymbol{r})\Big)^2\Big].$$

This potential has a similar cosine-squared modulation as in the periodic potential for the ground state $U_g^{\sim}(\boldsymbol{r})$ in Eq. 3.26.

In the landscape factor θ_n, the size of the Rydberg electron wave function, hidden in $|n\rangle$, is compared to the cosine-shaped modulation of the standing wave trap. The landscape factor θ_n can be calculated by expanding the cosine in terms of spherical Bessel functions. It follows that the landscape factor is given by [58]

$$\theta_n = \langle nS|\cos(2kx_\mathrm{e})|nS\rangle = \int_0^\infty dx_\mathrm{e}(R_n(x_\mathrm{e})\cdot x_\mathrm{e})^2 j_0(2kx_\mathrm{e}), \tag{3.30}$$

where $R_n(x_\mathrm{e})$ is the radial electron wave function in Rydberg state nS, and $j_0(2kx_\mathrm{e})$ is the spherical Bessel function of the first kind for zero angular momentum [60].

Figure 3.5(a) and 3.5(b) show the size of different Rydberg electron radial wave functions in comparison to a cosine-squared intensity distribution. For a direct comparison, the Bessel function for the respective laser wavelength is presented in Fig. 3.5(c). The extent of the wave function in Fig. 3.5(a) increases quickly with principal quantum number, with the Rydberg electron radius scaling $r_\mathrm{e} \propto (n^*)^2$ given in Table 2.1. The variation in Rydberg state energy with n is so small compared to the energy of the $|a\rangle$ to $|n\rangle$ transition that the laser wavelength almost does not change, as shown in Fig. 3.5(b). These scalings lead to an increased sampling of the Rydberg electron of the potential landscape with higher principal quantum number [58]. Fig. 3.5(d) shows the change of the landscape factor over a range of principal quantum numbers. The electron of a ground-state atom explores only a small spatial region and therefore, the landscape factor is close to 1. For higher Rydberg state, the electron effectively samples several lattice sites and the effect of the periodic intensity variation averages out to $\theta_n = 0$.

The total energy shift of the Rydberg state is then

$$\begin{aligned} U_n(\boldsymbol{r}) &\approx U_n^{(1)}(\boldsymbol{r}) + U_n^{(2)}(\boldsymbol{r}) \\ &= -\frac{D_{an}^2}{8\hbar\Delta}\omega^2|\boldsymbol{A}(\boldsymbol{r})|^2 + U_n^{(2)}(\boldsymbol{r}). \end{aligned}$$

As for the ground state, the Rydberg state potentials can be written as a periodic and nonperiodic part

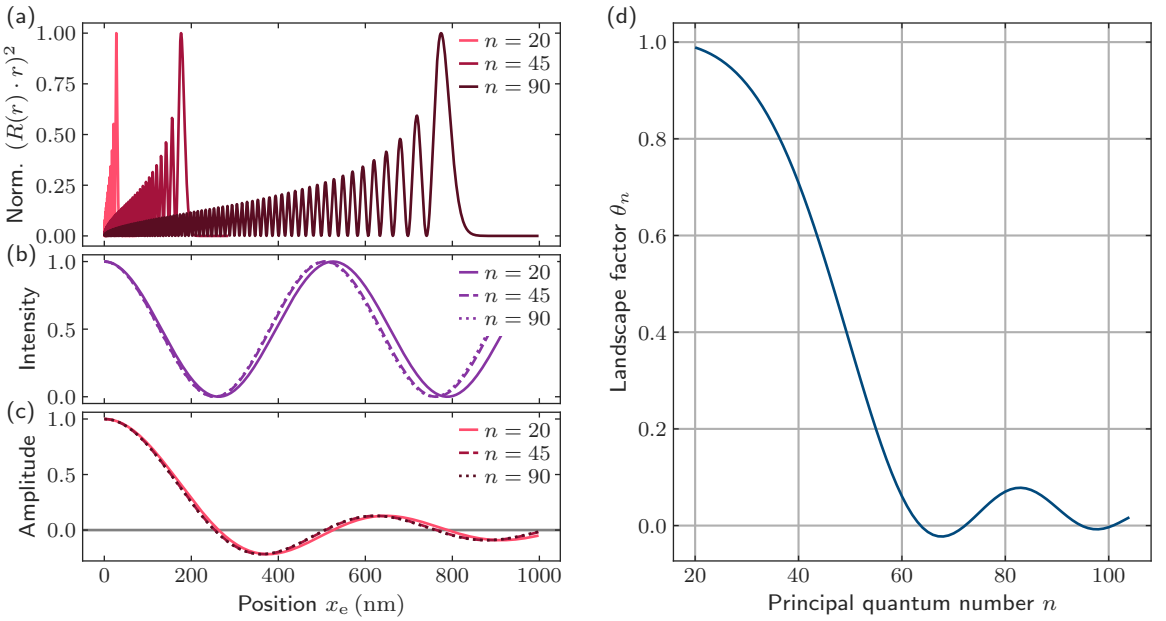

Figure 3.5: (a) Normalized radial wave function of the Rydberg electron in states $|20S\rangle$, $|45S\rangle$, and $|90S\rangle$. (b) The $\cos^2$ intensity distribution for a laser with the wavelength required to couple the respective Rydberg state and the lower-lying state $\left|6P_{3/2}\right\rangle$. (c) Bessel function of the first kind as it is used to calculate the landscape factor. (d) Landscape factor θ_n from Eq. 3.30 as a function of the principal quantum number n.

given by

$$U_n(\boldsymbol{r}) = U_n^{\sim}(\boldsymbol{r}) + U_n^{-}(\boldsymbol{r}), \tag{3.31}$$

$$U_n^{\sim}(\boldsymbol{r}) = -E_{\rightarrow}(\boldsymbol{r})E_{\leftarrow}(\boldsymbol{r})\cos^2(kx)\left(\frac{D_{an}^2}{4\hbar\Delta} + \alpha_f\theta_n\right), \tag{3.32}$$

$$\begin{aligned} U_n^{-}(\boldsymbol{r}) = &-\frac{D_{an}^2}{16\hbar\Delta}\left(E_{\rightarrow}(\boldsymbol{r}) - E_{\leftarrow}(\boldsymbol{r})\right)^2 \\ &-\frac{\alpha_f}{4}\Big[2E_{\rightarrow}(\boldsymbol{r})E_{\leftarrow}(\boldsymbol{r})\left(1-\theta_n\right) \\ &+\left(E_{\rightarrow}(\boldsymbol{r}) - E_{\leftarrow}(\boldsymbol{r})\right)^2\Big]. \end{aligned} \tag{3.33}$$

It should be noted that the Rydberg state trapping potentials depend on the trap laser detuning Δ. In contrast, the ground state potential in Eqs. 3.25-3.27 does not depend on the detuning. We use this fact to control the potential depth difference between the ground and Rydberg states. The option to tune the potential difference is a key component to create a magic wavelength trap.

CHAPTER 4

Experimental Apparatus and Methods for Rubidium Rydberg Quantum Optics

After discussing the theoretical background of trapping atoms in ground and Rydberg states, we now turn to the experimental apparatus. In this chapter, we present an overview of the experimental setup, that is used to prepare, characterize and conduct experiments with a cloud of rubidium-87 atoms.

4.1 Overview of Experimental Setup

Figure 4.1(a) is a photograph taken of the experiment in February 2025. The first iteration of this experiment was built in Stuttgart and is mainly documented in the PhD thesis of H. Gorniaczyk [129].

The cloud of ultracold rubidium-87 atoms is prepared from a rubidium background gas inside the experiment vacuum chamber, partly shown in Fig. 4.1(a). The background gas is created from a rubidium alloy dispenser[1] located in the cylindrical glass-to-metal transition of the vacuum chamber (shown on the left in Fig. 4.1(a)). The rubidium evaporation rate is controlled by an applied current of around 4.2 A, and an ion pump[2] and a titanium sublimation unit[3] are used to maintain the vacuum to 1×10^{-10} mbar.

The experiments with rubidium atoms are conducted in a quartz glass cuboid with dimensions $60 \times 80 \times 149$ mm. The surfaces of the cuboid are coated with an anti-reflection coating ($R < 1.5\,\%$) optimized for normal incidence at wavelengths of 780, 420, 480, 532, and 1064 nm. The cuboid is connected to a stainless steel chamber with the cylindrical glass-to-metal transition shown in Fig. 4.1(a), ensuring that the glass part of the vacuum system is mechanically suspended from the steel chamber. The vacuum chamber has multiple electrical feedthroughs. The complete chamber can be moved along the y axis by shifting the mounting feet of the steel chamber and pulling the glass cuboid out of the magnetic field cage along the y axis in Fig. 4.1(a). This allows the rest of the experimental setup to remain fixed and aligned during the displacement.

Reinserting the glass cell into the center of the experiment has proven to be reproducible, typically requiring only minor realignment of the optical beams to resume normal operation.

[1] SAES Getters; Model: RB/NF/4.8/17 FT 10+10
[2] Varian VacIon Plus 40 Starcell
[3] Agilent Technologies Titanium Sublimation Cartridge

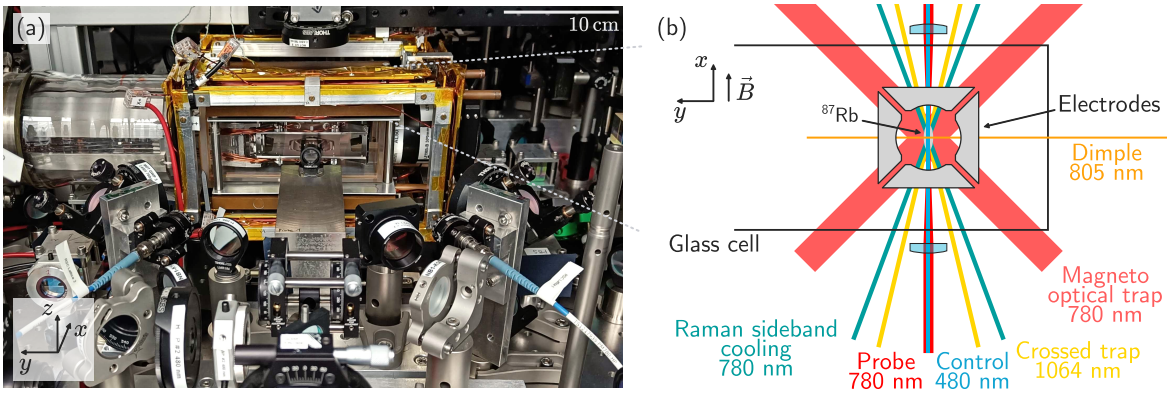

Figure 4.1: Overview of the experimental setup. (a) Photograph along the x-axis towards the cuboid-shaped glass cell of the vacuum chamber. Inside the glass cuboid, a cloud of rubidium-87 atoms is trapped and used for Rydberg experiments. Outside the vacuum chamber a set of coils are arranged to control magnetic fields. Inside the vacuum chamber a set of electrodes allows manipulating the local electric field the atoms experience. (b) Top view of the glass cell and the optical beam arrangement. The main axis is defined by the probe and control beam. Further, beams for the trapping and cooling of atoms are separately guided into the glass cell under different angles. See the main text for more details.

A pair of coils for controlling the magnetic field in the vacuum cell is mounted directly above and below the cell. These coils are mounted in an anti-Helmholtz configuration, producing a quadrupole magnetic field at the center of the cell. The quadrupole field is essential for the magneto-optical trapping and cooling of the rubidium atoms [130].

In addition, three orthogonal pairs of coils in Helmholtz configuration are installed around the glass cell to compensate for ambient magnetic fields. Figure 4.1(b) shows the configuration of the trapping and cooling beams used for the magneto-optical trap, as well as other beams employed for optically addressing the atoms.

The primary experiments described in this work are performed using a probe beam and a control beam, both aligned along the x-axis. The probe and control beam drive the two transitions in the EIT scheme shown in Fig. 2.1(a). Both beams are directed at normal incidence onto the anti-reflection-coated surfaces of the glass cell.

In our experiment, the lasers are selected and configured to match the specific interactions required with the atoms, with their wavelength, linewidth, and optical output power adjusted to the specific application. This section outlines the laser system that was set up in the course of this thesis.

For rubidium-87, the required optical wavelengths are accessible using commercially available diode laser systems. In our experiment, we mostly use commercial Littrow-type external cavity diode lasers.[4] For specific applications that demand high optical power, particularly in trapping and cooling, these lasers are amplified using a tapered amplifier,[5] yielding output powers in the watt range. A frequency doubling stage[6] is used to generate a laser beam at a wavelength of 480 nm that is required to excite the Rydberg states.

Most of the lasers are used to resonantly interact with specific atomic transitions, where the transition

[4] Toptica DL pro
[5] Toptica TA pro
[6] Toptica TA-SHG pro

wavelengths for rubidium, between different nS and nP states used in this thesis, are well known [80, 131, 132]. In order to monitor the wavelength of our near-infrared laser, we use a wavelength meter[7] with an absolute accuracy of 200 MHz. However, the linewidth for the lowest two dipole-allowed transitions are given by their natural linewidth $\Gamma_{D1} = 2\pi \times 5.75\,\text{MHz}$ and $\Gamma_{D2} = 2\pi \times 6.07\,\text{MHz}$ [133]. To precisely control the interaction between the laser light and the atoms, it is necessary to stabilize the laser frequency to a level well below the atomic natural linewidth. Most of the lasers in our setup are therefore stabilized in their optical frequency by referencing them to a long-term stable frequency standard.

In our lab, a high-Finesse Fabry-Perot cavity mounted in an ultra-low expansion (ULE) spacer is used as a frequency reference. The spacer with the cavity is placed in a cavity housing[8] which is temperature stabilized and kept under vacuum. Despite the isolated conditions of the cavity on the spacer, a linear drift of the cavity resonance at 960 nm of $20.8(6)\,\text{kHz/day}$ is observed. The drift has been monitored over months, and compensated for by adjusting the frequency referencing to the cavity accordingly.

To allow the stabilization of lasers with different wavelength, the stable reference cavity mirrors are coated for high reflection in the ranges 780 – 795 nm, 840 nm, 950 – 970 nm, and 1010 – 1020 nm. Figure 4.2 shows a schematic of the components and techniques that were set up during this thesis. Three lasers at the wavelengths 780 nm, 960 nm, and 1012 nm are stabilized with the Pound-Drever-Hall technique (PDH) [134, 135] to resonances of the stable reference cavity. The generated error signal by the PDH technique is adjusted in a proportional-integral-derivative controller (PID) and subsequently applied to the laser diode current and piezoelectric-controlled grating. For the two lasers at wavelength of 960 nm and 1012 nm, we installed fiber-coupled electro-optic modulators (EOM) in the beam path towards the cavity. As the modulated sidebands can be stabilized with respect to the cavity, one can adjust the exact frequency of the laser by changing the EOM modulation frequency.

In most of the experimental steps, from atom preparation to Rydberg experiments, the lasers with a wavelength of 780 nm are close to the transition $5S_{1/2} \leftrightarrow 5P_{3/2}$ (D2-line) in rubidium-87. To precisely control the laser wavelength required for a given application, multiple lasers at a wavelength of 780 nm are stabilized in frequency relative to one reference laser. This reference laser is stabilized to the reference cavity as indicated in Fig. 4.2. In this so-called beatnote offset lock, the beatnote between two lasers can be compared to a computer controllable frequency $f_{\text{ref,beat}}$. The frequency comparison is converted into an error signal by using a delay line [136] or an all-digital phase detection [137], and the feedback is adjusted in a PID controller to correct for laser frequency deviations.

A careful optimization of all these feedback loops includes the reduction of cable and optical path length, tuning of electrical signal and optical beam powers, and choice of the PID controllers settings. Thereby, the laser linewidth can be reduced to well below the natural linewidth of the lowest rubidium transitions, and to a similar scale as the narrow Rydberg transitions, given by the Rydberg state lifetimes in Section 2.2.

A detailed study of laser frequency noise and the influence of this noise on Rydberg experiments is to be published in Ref. [138].

[7] Ångstrom High Finesse WS6/200-1988
[8] Stable Laser Systems, Housing model: VH6010-4

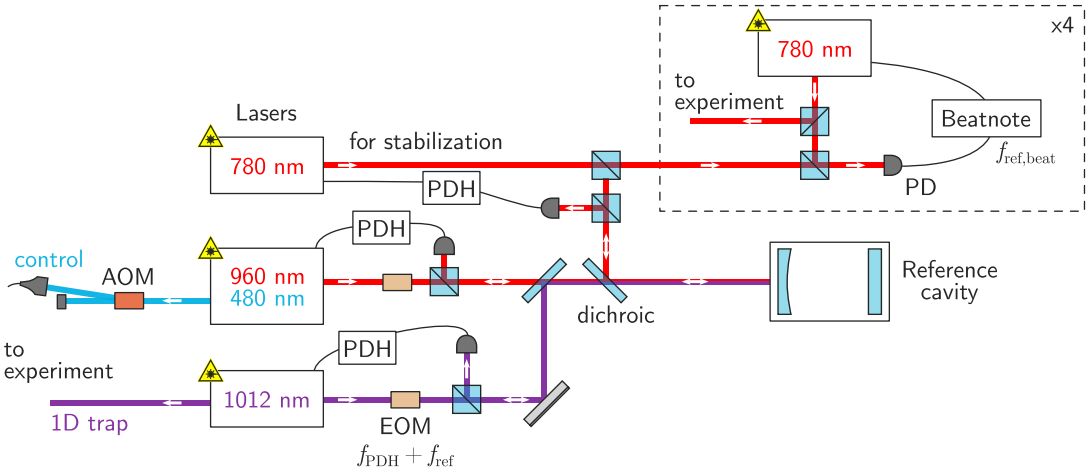

Figure 4.2: Schematic of the laser setup providing an overview of the different techniques used to control the frequency, and power of the laser beams used in the experiments discussed in this thesis. Lasers with wavelengths of 780 nm, 960 nm, and 1012 nm are stabilized. The three lasers on the left are stabilized with the Pound-Drever-Hall technique (PDH) to the stable reference cavity. The boxes labeled PDH include a demodulation module (demodulate with f_{PDH}) and a feedback controller. The exact frequency of the control and the one-dimensional trap are set by the reference frequency f_{ref} modulated onto the light with electro-optic modulators (EOM), that defines the frequency offset with respect to a transmission resonance of the reference cavity. The fundamental beam at 960 nm is stabilized, and another part of the beam is amplified and frequency doubled to 480 nm to be used as control laser in the Rydberg experiments. The 780 nm laser stabilized to the reference cavity is used as a reference to stabilize four additional lasers at 780 nm with the beatnote offset locking technique, for which four setups as sketched in the upper right corner. As the name suggests, the relative frequency between two lasers is detected on a photodiode (PD) and afterward stabilized with a feedback controller to a reference frequency $f_{\mathrm{ref,beat}}$, see main text for details. Each beam, before it is sent to the experiment, is deflected by an acousto-optic modulator (AOM), where the amplitude of the applied radio frequency controls the amount of light coupled into an optical fiber.

4.1.1 Trapping and Cooling of Neutral Rubidium Atoms

In this section, the different experimental steps from the background gas to a cold atomic cloud are discussed. Additionally, the method of absorption imaging is introduced and used to characterize the atomic cloud shape and temperature.

Magneto-Optical Trap Loaded from Background Gas

A magneto-optical trap (MOT) is a widely used technique [130] for capturing, confining and cooling atoms within a defined region inside a vacuum chamber. Figure 4.3(a) illustrates the optical and magnetic field configuration required for a MOT. The gradient magnetic field creates a magnetic field that increases linearly in amplitude with a vanishing field in the center. We load the MOT with a radial and axial gradient of 8.2 G/cm and 16.3 G/cm, respectively. Thereby, the atoms experience a position dependent Zeeman splitting [139]. Laser beams from six directions are used to reduce the atomic momentum. The laser beams are tuned to only interact with atoms moving towards the respective beam. Due to the Doppler shift, only atoms moving towards and not collinear with the beam are absorbing photons. An isotropic spontaneous emission results in a net removal of momentum from

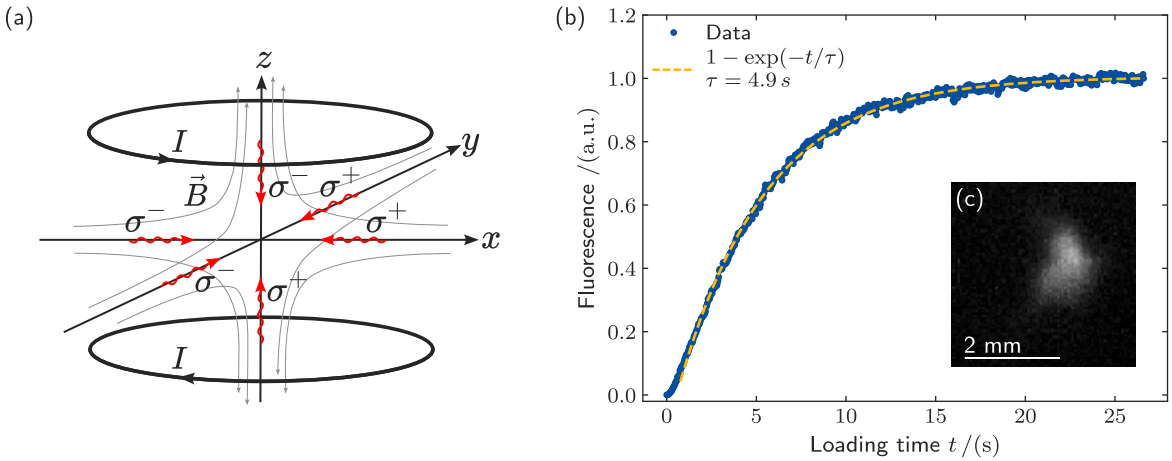

Figure 4.3: (a) Light and magnetic fields used for a magneto-optical trap. The six laser beams are $\sigma^{\pm}$ polarized. The thin lines show the orientation of the quadrupole magnetic field created by the current I running through a pair of coils in anti-Helmholtz configuration. (b) Atomic fluorescence as function of MOT laser operation time. The dashed line is an exponential fit with a time constant of 4.9 s [140, 141]. (c) Fluorescence image of the MOT. Figure (a) adapted from Ref. [142].

the respective atom. The gradient amplitude defines the spatial region in which the Zeeman shift is large enough to enable the atomic excitation together with the Doppler shift. Adjusting the magnetic field gradient and laser detunings allows the creation of a spatial region where atoms are effectively confined.

Figure 4.3(b) shows the fluorescence from the trapped rubidium-87 atoms after the MOT beams are turned on. For the experiments presented in this thesis the MOT load time was 1.3 s, which is a trade-off between number of atoms used for later experiments and overall experiment cycle duration.

The atoms are trapped in a region of approximately 2 mm^3 as shown in Fig. 4.3(c). The region in which the atomic cloud is confined can be changed by varying the gradient field amplitude. An increase in gradients, for us 37 G/cm and 74 G/cm, leads to a smaller distance from the gradient center where the energy level shifts are comparable to the Doppler shifts.

Resonant Absorption Imaging

The image shown in Fig. 4.3(c) is obtained using fluorescence detection, but the atomic cloud can also be imaged using absorption imaging [143]. In this technique, atoms scatter photons from a resonant imaging beam, and the resulting shadow cast by the cloud is recorded on a camera. Absorption images of the atomic ensemble are used to ensure spatial overlap with the optical beams in the vacuum chamber and to extract information about the temperature of the atomic cloud.

Figure 4.4(a) shows the setup to record images of the atom cloud in two different directions. The horizontal system images the x-y plane and the vertical system images the x-z plane. In each direction, a collimated beam on resonance with the D2-line (780 nm) is sent onto the rubidium cloud. The plane of the atomic cloud is imaged onto a CCD camera[9] with a telescope. For one absorption image, three separate images are captured.

[9] PCO; Model: pco.pixelfly USB digital 14 bit CCD camera; sensor: ICX285AL

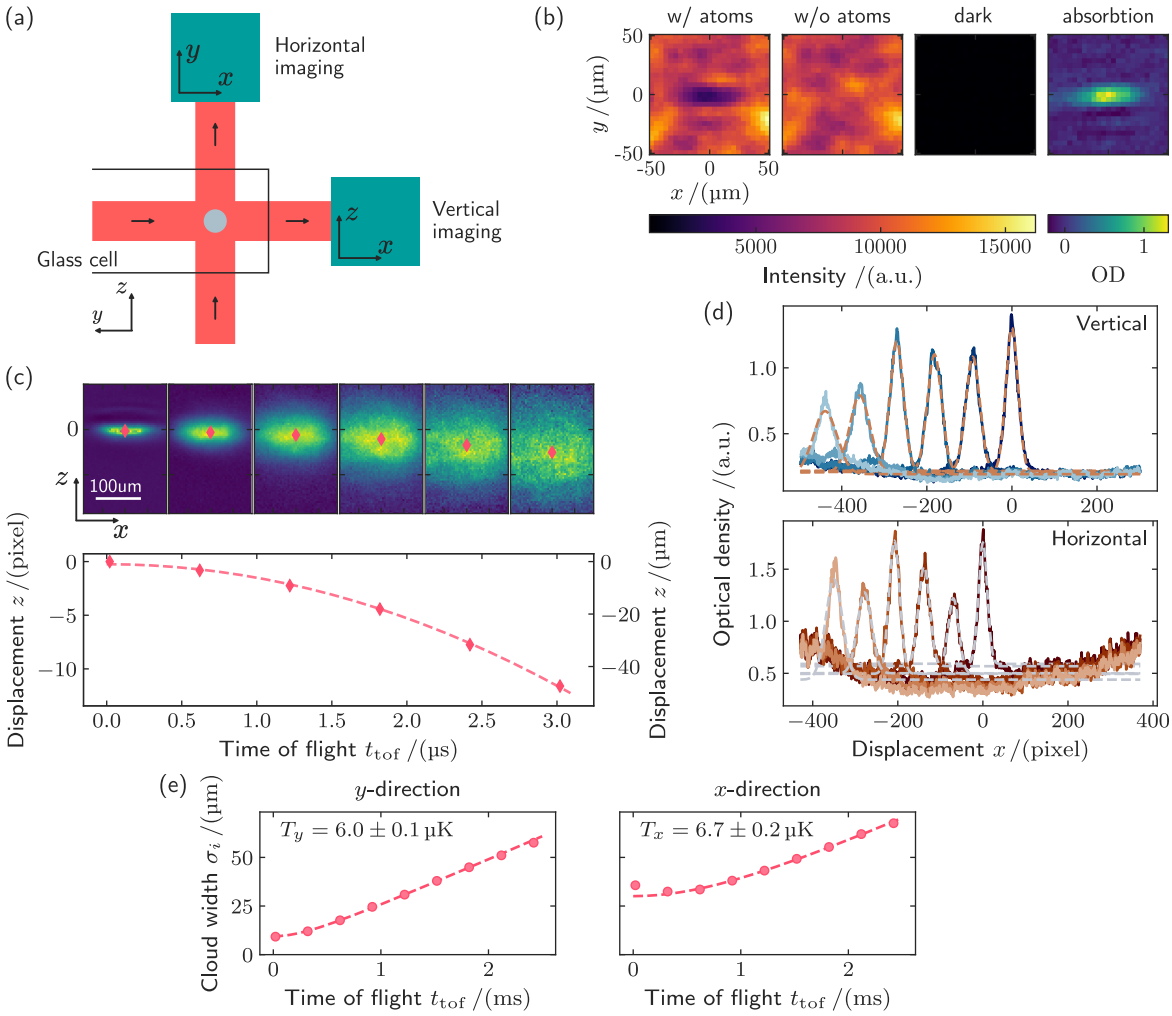

Figure 4.4: (a) Setup to record absorption images of the atomic cloud from two different directions. (b) Three images from the horizontal direction as they are used to calculate the final absorption image. The shadow and bright image are recorded with and without atoms in the imaging beam path. The dark background image is measured without the imaging beam. (c) Image size calibration in the vertical imaging. The atomic cloud falls under gravity. The cloud center-of-mass displacement z as a function of time of flight duration t_{tof} is fit with Eq. 4.2 (dashed line). (d) Image size calibration in horizontal imaging. A magnetically trapped atomic cloud is shifted for six different bias magnetic fields along the x-axis. The vertical size calibration is transferred to the horizontal direction by the common shift. (e) Atomic cloud width σ_i, for axis i in the horizontal imaging, and theoretical thermal expansion (dashed, Eq. 4.3) as function of t_{tof} after releasing from the crossed dipole trap.

Figure 4.4(b) shows example images with and without atoms, as well as a background image. From these, we calculate an optical column density for each pixel as

$$\mathrm{OD} = -\ln\left(\frac{I_{\mathrm{shadow}} - I_{\mathrm{bg}}}{I_{\mathrm{bright}} - I_{\mathrm{bg}}}\right). \tag{4.1}$$

Here, I refers to the pixel data recorded with atoms (shadow), without atoms (bright), and the

background image (bg), respectively. The absorption images allow us to investigate the atomic density distribution at any point in the experiment cycle. It is an undesirable side effect of this type of analysis that the absorption imaging is a destructive measurement. No Rydberg experiments can be performed afterward imaging.

The image size of the atomic cloud on the camera chip is given by the magnification of the imaging system. We use the atomic cloud to calibrate the effective size of a single pixel in the two different directions. The camera has a pixel size of $6.45 \times 6.45\,\mu\text{m}^2$. In Fig. 4.4(c), we image the cloud falling under gravity for different time of flight durations t_{tof}. The center-of-mass cloud position is given by

$$z_{\text{com}} = \frac{1}{2} a t_{\text{tof}}^2 + z_0, \tag{4.2}$$

where a is the acceleration in the z direction in units of pixel/s^2, and z_0 is the initial cloud position. We calculate an effective pixel size from the known gravity of earth g [144] as $g/a = 4.09\,\mu\text{m/pixel}$. We assume the vertical imaging system to have the same magnification along the x- and the z-axis, as all optical elements are orthonormal with respect to the laser beam. The images in Fig. 4.4(b) are given in µm by using the effective pixel size.

Once the effective pixel size has been determined for the vertical imaging system, it can serve as a reference for the horizontal imaging system. To determine the effective pixel size in the horizontal direction, the atoms are trapped in a magnetic trap [73]. The magnetic field experienced by the atoms in the x direction is given by

$$B(x) = G_{\text{x}} \cdot x + B_{\text{x,bias}} + B_{\text{x,bg}},$$

where G_{x} is the trapping gradient field, $B_{\text{x,bias}}$ is a controllable bias field, and $B_{\text{x,bg}}$ is a background field in the lab. For $B(x) = 0$, we find the position in y direction with zero field as

$$x(B_{\text{x,bias}}) = -B_{\text{x,bias}}/G_{\text{x}} - B_{\text{x,bg}}/G_{\text{x}}.$$

Figure 4.4(d) shows the shift of the atomic distribution center along the common axis of the two imaging systems, while the different traces are recorded for different applied magnetic bias fields. From this and the known shift in the vertical direction, we calibrate the effective pixel size in the horizontal direction to $5.27\,\mu\text{m/pixel}$.

Once the imaging system has been calibrated, the absorption images can be used to characterize the atomic cloud. The temperature of the atomic cloud can be determined by observing its expansion as a function of time-of-flight [145]. For each time of flight, a Gaussian function given by

$$f(x) = A \cdot \exp\left(-[x - x_0]^2/[2\sigma^2]\right) + C$$

is fitted to the absorption images, and the width of the distribution is extracted. The temperature of the atomic cloud T is obtained from the function

$$\sigma(t_{\text{tof}}) = \sqrt{\frac{k_{\text{B}} T}{m_{\text{Rb}}} t_{\text{tof}}^2 + \sigma_0^2}, \tag{4.3}$$

where k_{B} is the Boltzmann constant, m_{Rb} is the mass of rubidium-87 and σ_0 is the initial cloud size.

Crossed and Dimple Optical Dipole Trap

To perform experiments involving collective Rydberg excitations, as introduced in Chapter 2, a cold and unperturbed atomic cloud is required. The strong magnetic field gradients present in the MOT are incompatible with coherent excitation.

A suitable alternative is the use of far off-resonant optical dipole traps [112]. These traps enable tight spatial confinement without significant scattering, and they can be configured to reduce perturbations to internal atomic states. In our experiments, a brief release from the trap followed by recapture allows multiple measurements to be conducted with the same atomic cloud, while avoiding differential light shifts during the free-fall phase.

As indicated in Fig. 4.1(b), the optical dipole trap in our experiments is formed by two crossed laser beams. Their crossing angle is 31.4°. The crossing region is overlapped with the center of the compressed MOT. Figure 4.5(a) and 4.5(b) show the transfer sequence from the MOT into the crossed trap. In order to optimize the transfer efficiency, we increase the magnetic field gradients at the end of the MOT phase to decrease the spatial extent of the atomic cloud. With a cloud volume of approx. 200 μm^3, the overlap with the crossed dipole trap is increased. We increase the optical density of the cloud by simultaneous evaporative [146, 147] and Raman sideband cooling [148–151]. More details on the cooling stage can be found in Ref. [152, 153]. We reach a final atom number of 60000(3000) with a temperature of 6.7(2) µK. The temperature is determined from the cloud expansion in Fig. 4.4(e). The density of the atomic cloud distorts the measured atom distribution for the initial absorption image. In the calculated trapping potential, we estimate a peak atomic density of $3.6 \times 10^{12}\ 1/\mathrm{cm}^3$.

Figure 4.5(c) shows the cigar-shaped cloud with the long axis along the probe direction. We define the length of the atom cloud $L = 81.6\,\mu m$ as the $1/e^2$ full-width.

The atom cloud can be further shaped by a dimple beam, which is perpendicular to the long axis of the cloud as indicated in Fig. 4.1(b). The dimple beam is focused onto the atom cloud by an objective with an effective focal length of 79.5 mm. An acousto-optic deflector (AOD) allows the deflection of the incoming beam into multiple steerable macro tweezer beams. Their position can be individually adjusted along the x-axis, as described in Ref. [154]. The $1/e^2$ waist radius in the x direction is 7.4 µm, and allows trapping ensembles that are smaller than the Rydberg blockade radius. Thereby, we can realize one [30, 88] or up to three [91] Rydberg superatoms, which are discussed in Section 2.3.

4.1.2 Two-Photon Excitation Optics

With the atoms trapped and cooled in the optical dipole trap, the experiments with Rydberg atoms can take place. Figure 4.6 shows the optical setup for the two-photon Rydberg excitation that corresponds to the excitation scheme introduced in Section 2.1. The setup consists of a single 480 nm control beam together with two 780 nm probe beams from opposite directions. All beams for the two-photon excitation are propagating along a single axis. This configuration allows us to perform measurements with probe and control light co- and counter-propagating depending on the choice of probe beam. Starting with probe 2 on the left side in Fig. 4.6, the 780 nm light is coupled out of a single mode polarization-maintaining fiber[10] with a fixed 25.08 mm focal length triple lens collimator.[11] The light

[10] OZ Optics PMJ-3AF-3AF-850-5/125-3A-8-1
[11] Thorlabs TC25APC-780

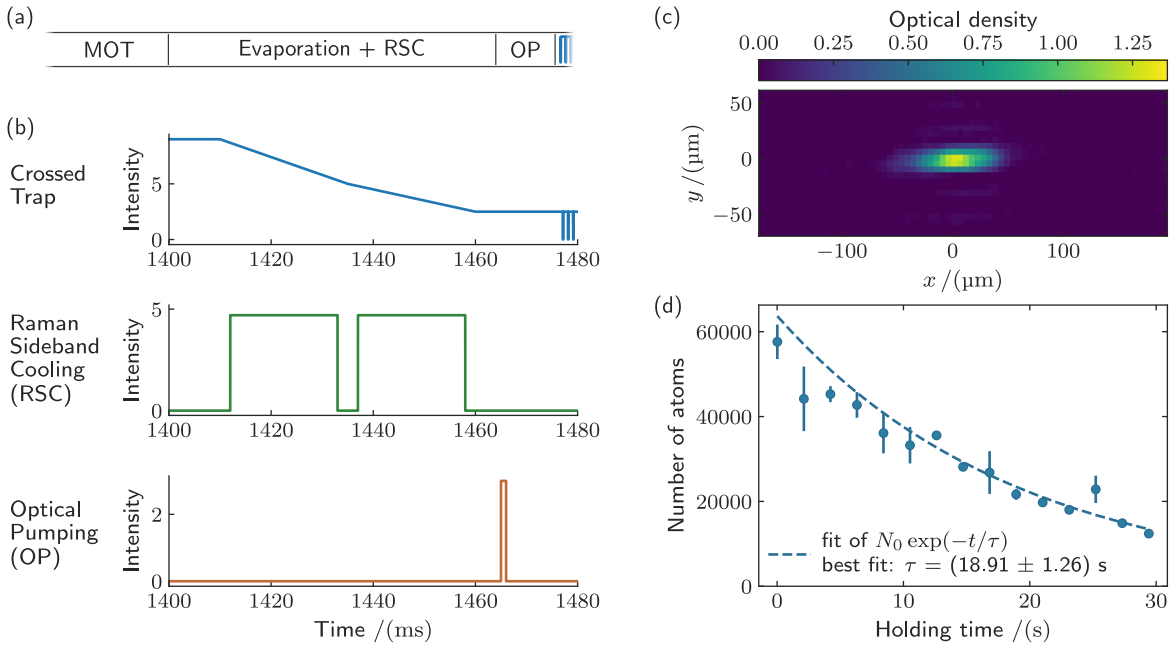

Figure 4.5: (a) Timing sequence for evaporative and Raman sideband cooling (RSC). (b) Intensity ramps to cool the atoms trapped in the crossed dipole trap by evaporative cooling with simultaneous Raman sideband cooling. See the main text for details on the Raman sideband cooling. An optical pumping (OP) pulse prepares the atomic state, which is discussed later in Section 4.2. (c) Absorption image of the atomic cloud prepared in the crossed optical dipole trap, right after the optical pumping. (d) Atom number as a function of holding time in the optical dipole trap.

is transmitted through a polarizing beamsplitter cube (PBS) and turned into right-handed circularly polarized light by a set of half- and quarter-wave plate.

The beam passes through two dichroic mirrors to separate the counter-propagating 1012 nm light[12] and the 480 nm control light,[13] respectively. Afterward, the probe beam is focused into the vacuum chamber glass cell by an achromatic lens outside the vacuum chamber. The effective focal length of this lens is $f_{\text{eff}} = 50\,\text{mm}$.[14] We determined the waist radius of the probe and the control beam by removing the vacuum chamber from the magnetic coil cage in Fig. 4.1(a). The beam is recorded at different positions in the x direction with a camera, while a small glass window sample is placed in the beam path to mimic the glass cell window. The $1/e^2$ intensity waist radius of the probe beam is 5.1 µm, and for the control beam it is 19.1 µm.

The atomic cloud has to be positioned at the waist of the probe beam. In order to determine the waist position precisely, we use the atom cloud as a measurement tool. A probe beam with a classical beam power can remove atoms locally from the larger ensemble by scattering photons. The extent of the atom cloud confined in the crossed dipole trap, as in Fig. 4.6(c), is with a length $L = 81.6\,\mu\text{m}$ comparable to the Rayleigh range of the probe beam with $x_{\text{R,p}} = 100\,\mu\text{m}$. Therefore, we perform these measurements with the atoms trapped in the dimple trap, which can be positioned over a larger

[12] Thorlabs DMSP950
[13] Thorlabs DMLP650
[14] Edmund Optics #49-328, Achromatic Lens 12.5 mm Dia. × 50 mm FL, VIS-NIR Coating

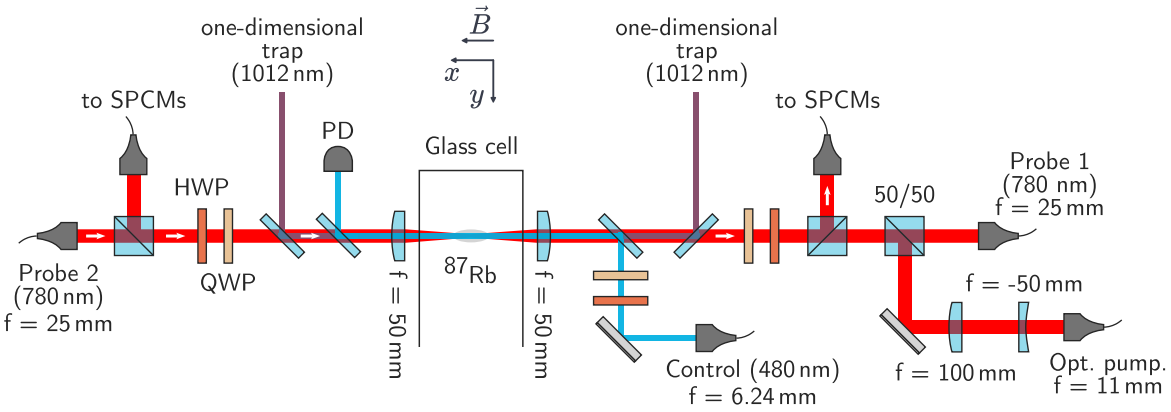

Figure 4.6: Setup for two-photon Rydberg excitation with two counter-propagating 780 nm probe (1,2) beams. The white arrows indicate the propagation direction of the probe 2 beam. The beam polarizations are set by half-wave plates (HWP) and quarter-wave plates (QWP). After passing the atoms, the probe light is reflected on polarizing beamsplitter cubes (unlabeled cubes) towards the single photon counting modules (SPCMs). A 50/50 beamsplitter cube overlaps the hyperfine optical pumping and probe 1 light. The 480 nm control and the 1012 nm trap beam are superimposed with the probe beams with dichroic mirrors. All beams propagate collimated outside the vacuum chamber and are focused onto the atoms with a pair of lenses. The control light intensity is stabilized with a photodiode (PD) placed behind the chamber.

x-range.

Figure 4.7(a) shows the atom cloud at different positions in the x direction, where the probe beam removes atoms within its beam path. For this measurement, the atoms are released from the trap and expand for 0.3 ms before being exposed to the probe beam. We determine the width from where atoms are removed by a fit of two Gaussian distributions as shown in Fig. 4.7(b). The overall cloud is described by one wide Gaussian, and a second narrower Gaussian with negative amplitude characterizes the distribution of missing atoms. The respective widths are the waist radius, where the integrated OD reduced to $1/e^2$. The change of the waist along the x-axis follows the theory for a Gaussian beam waist as shown in Fig. 4.7(c). We position the atomic cloud with the crossed optical dipole trap in the focus of the probe beams. All parts of the experiment are referenced with respect to the focal point of the probe beam.

After passing the atoms, the probe 2 polarization is rotated to be orthogonal with respect to the polarization at the outcoupler and, hence, reflected at the PBS. The probe light is coupled into a single mode fiber[15] towards our single photon detection setup. We do not require a polarization-maintaining fiber for the probe towards the detection setup, as the detection setup is not polarization sensitive, and our analysis is based on the absolute number of detected photons.

In Fig. 4.8, we sketch the detection setup of the probe beam. After the single mode fiber, the probe beam is split into four parts in a Hanbury Brown and Twiss setup [155, 156]. Each output beam is coupled into a multimode fiber and onto a single photon counting module[16] (SPCM). The SPCMs have a specified quantum efficiency of 64 % at 780 nm. The transmission from the atomic cloud to the output of the multimode fiber is 55 %. We attenuate the probe beam to typically use photon count rates below 1 Mc/s, where the SPCMs are linear in their count rate response. The SPCM dark count

[15] Thorlabs 780HP-Custom Patch Cable Fiber: 780HP, Tubing: FT061PS, End Facets: FC/PC and FC/APC, Length: 2 m
[16] Excelitas SPCM-AQRH-23 FC

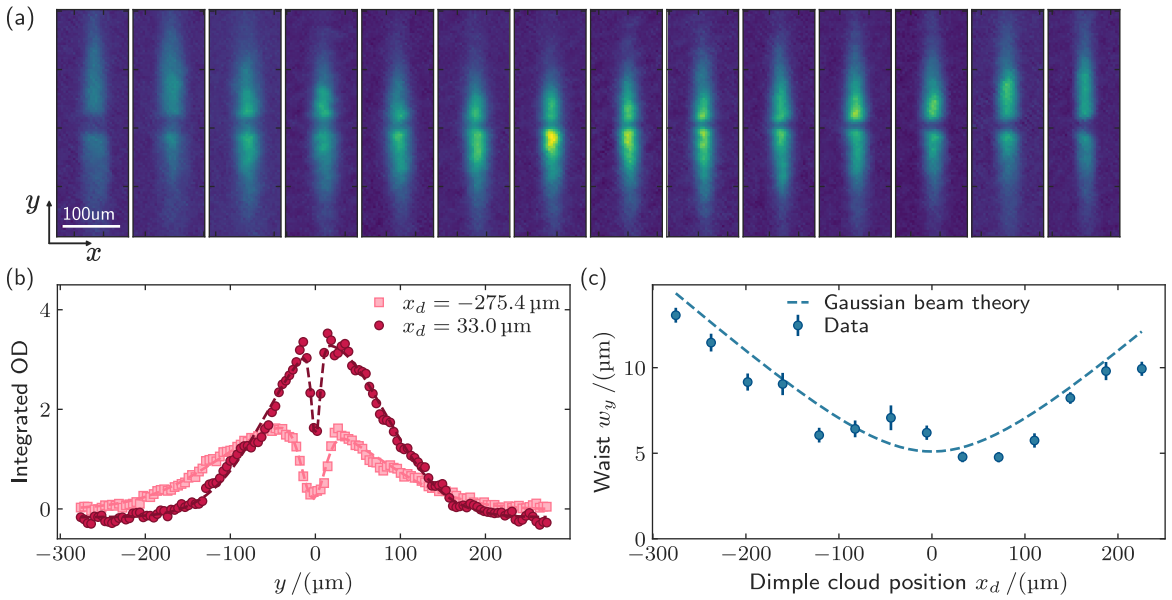

Figure 4.7: (a) Absorption images of the atomic cloud trapped in the dimple beam, where a center fraction of atoms is removed by resonant probe light. The position of the cloud is varied along the x-axis to determine the focal point of the probe beam. (b) Integrated optical depth for two different dimple cloud positions x_d. The dashed lines show the double Gaussian fits that are used to extract the width from where atoms are pushed away from the probe beam. (c) The probe beam waist as a function of the dimple cloud position. Each data point is extracted from fits as in (b) and compared to the theoretical beam waist for a Gaussian beam as in Eq. 3.17. The images shown in (a) are measured for the different positions in (c).

rate of 731(3) Hz in the worst of the four counters is well below the used signal count rates in the experiment. We use two transmission band-pass filters to block all other light except for the 780 nm probe photons. The Semrock FF01-780/12-25 and the Semrock LL01-780 create a combined optical density of 6.6 for the 480 nm control light and of 10.9 for the 1064 nm crossed dipole trap light. To reduce standing-wave interference between the two filters, the first is mounted before and the latter after the single mode fiber.

The setup is almost identical for the probe 1 beam that is counter-propagating with probe 2. A beam for the hyperfine optical pumping is overlapped with the probe 1 beam on a non-polarizing beam splitter. We ensure the overlap between both probe beams by cross-coupling one into the out-coupling fiber of the other.

4.1.3 Few-Photon Transmission through the Atomic Cloud

The detection of probe pulse transmission through the atomic ensemble is our essential tool to investigating the coupling of photons to matter. As an alkali atom with a single outer electron and a nuclear spin of $I = 3/2$, rubidium-87 has multiple hyperfine states.

Figure 4.9(a) shows the optical probing transition close to 780 nm in the hyperfine state basis. The weak probe light is σ^+ polarized to drive the closed transition $|F = 2, m_F = 2\rangle \leftrightarrow |F = 3, m_F = 3\rangle$. We define the quantization axis of our system along a magnetic field that can be generated with the bias coils. This magnetic field is along the probe direction.

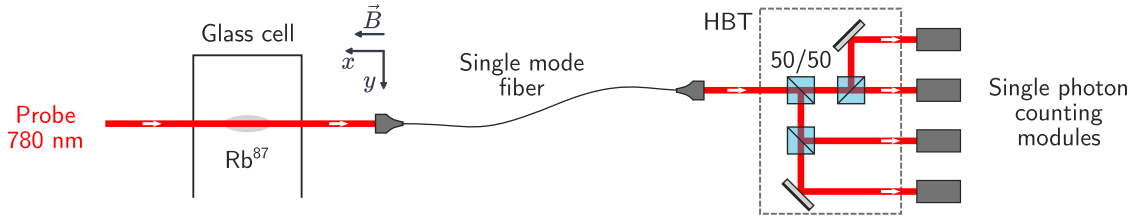

Figure 4.8: Schematic of the few-photon transmission measurement setup. The transmission of the 780 nm probe beam is coupled into a single-mode fiber. In a Hanbury Brown Twiss (HBT) setup, the transmitted photons are split into four paths using three 50/50 beamsplitters and detected on single photon counting modules.

Figure 4.9(b) shows the timing sequence for the probing measurements performed on the cold rubidium atoms in the crossed dipole trap. In each experiment, the crossed dipole trap is turned off as depicted in Fig. 4.9(c) to avoid inhomogeneous broadening of the probing transition due to the trapping beam. In this example, a single 8 µs long probe pulse is sent onto the released atoms.

In the rest of this thesis, we denote the experiments with the released atoms as free-space experiments. It has to be noted that the probe pulses in the bottom of Fig. 4.9(c) are averages over many repetitions to show the overall pulse shape. A single pulse only contains ten to one hundred photons, depending on the specific experiment. The few photons are detected with the setup shown in Fig. 4.8.

After the probe pulse, the dipole trap is turned back on to recapture the atomic cloud. The same atomic cloud is probed 1000 times, where two probe pulse measurements are repeated every 100 µs. At the end of the 1000 measurements, the atomic cloud is released by turning of the dipole trap for 10 ms as marked in Fig. 4.9(a). During this period, the atoms leave the optical dipole trap crossing region due to their kinetic energy and acceleration by gravity. Therefore, the atoms are not recaptured when the crossed trap is turned back on.

We subsequently perform a second set of 1000 probe pulse measurements to reference the transmission with and without atoms. We extract one thousand measurements per experiment cycle, which corresponds to 1000 data points in 1.7 s.

Figure 4.9(d) shows the transmission as a function of the probe beam detuning. The theoretical transmission can be calculated with the susceptibility of a two-level system given in Eq. 2.2. The probe transmission through the atomic cloud is given by

$$T(\Delta_p) = \exp\left(\frac{-\mathrm{OD}}{1 + 4 \cdot \left(\Delta_p/\Gamma_{\mathrm{D2}}\right)^2}\right), \tag{4.4}$$

with Γ_{D2} as the natural linewidth of the D2 line in rubidium-87, and OD as the optical density of the atomic cloud.

However, the fast switching of the trap intensity leads to a heating associated with parametric excitation of the oscillatory atomic motion [56, 157]. The effect is increased by the small standing wave nature of the two crossed trap beams as discussed in Section 4.1.1. The increase in temperature reduces the atomic density in the crossed trap. The optical density OD decreases by a factor of 2 from the first to the last one hundred measurement pulses.

The measurements presented in this thesis do not depend on the exact optical density, and it is justified to consider the mean transmission across the 1000 pulses.

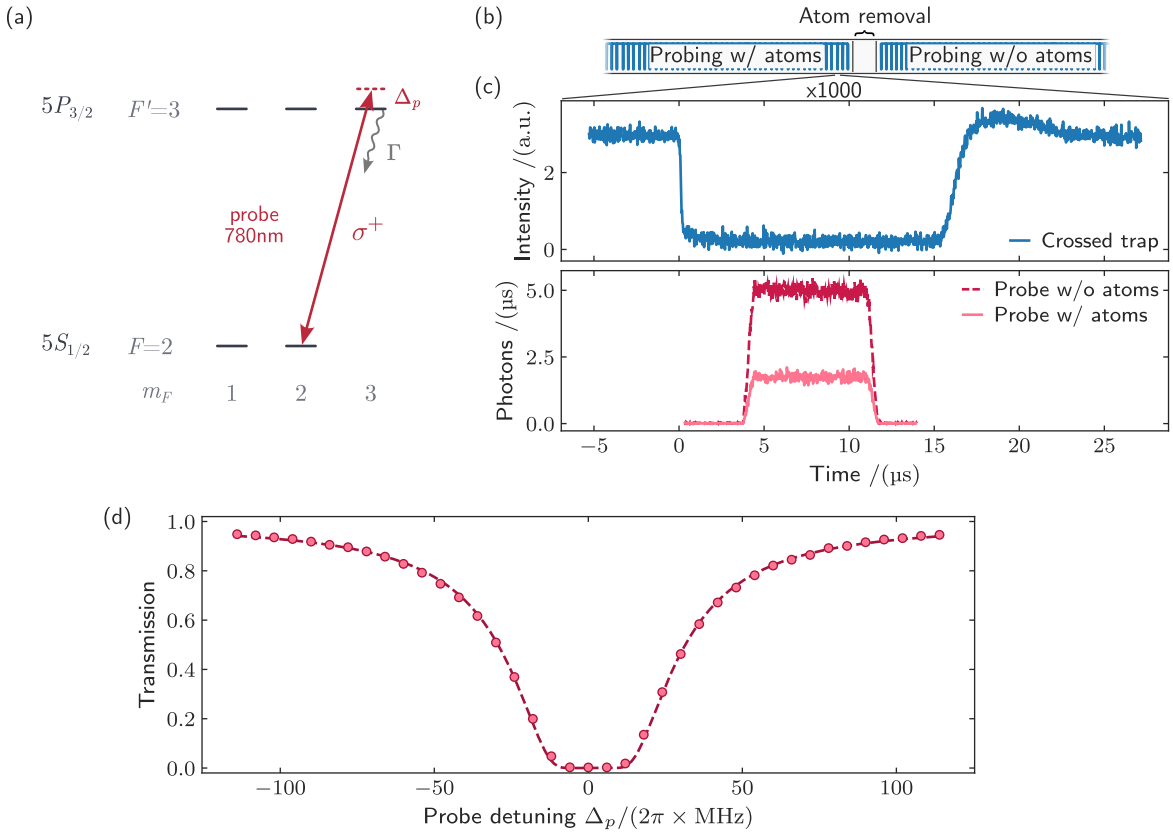

Figure 4.9: (a) The optical transition used for the few-photon probing experiments. The probe laser with frequency ω_p is detuned by $\Delta_p = \omega_p - \omega_0$ from the D2-line in rubidium-87, with transition frequency ω_0. The indicated spontaneous decay rate Γ_{D2} is given by the natural lifetime of the excited state $5P_{3/2}$. (b) The timing sequence for transmission measurements that are performed after the atom preparation steps shown in Fig. 4.5(a) and 4.5(b). One thousand pulses are measured with atoms and, after removing the atoms, one thousand reference pulses are recorded. (c) The sequence for the 1000-times repeated probe transmission measurement. The first set is measured with the atoms in the probe beam path and the second set is measured afterward without the atoms. The beam power of the crossed trap (top) is switched off to release the atoms during the probing. The probe pulses are averages over 40000 repetitions. (d) Transmission of the probe beam as function of the probe detuning Δ_p. Each data point is the ratio between the recorded probe photons with and without atoms on the single photon detectors, as the example in (b). The transmission for each detuning is averaged over 95000 single measurements. The dashed line shows a fit of the saturated absorption line model in Eq. 4.4.

4.2 Atomic State Preparation

The experimental setup to measure the probe transmission of the cold atomic cloud allows us to investigate and control the internal state of the rubidium atoms. For our quantum optics experiments, we require stable and identical conditions from one experimental cycle to the next. In this section, we explain how we compensate for external magnetic fields by using the atomic cloud as a sensor. We furthermore discuss the method of optical pumping to prepare all atoms in a desired atomic state.

In order to drive the probing transition with a σ^+ polarized photon as introduced in the previous

section, we require a magnetic field pointing along the probe beam axis. Such a quantization axis is shifted away from the probe beam axis by stray magnetic fields. A large source of stray magnetic fields is the earth magnetic field, with a magnitude of about 0.5 G [158]. Furthermore, we have other sources of magnetic fields in the lab, including but not limited to power supplies and an ion vacuum pump about 50 cm away from the atoms.

According to the Zeeman effect, the hyperfine state energy is shifted in energy due to a weak external magnetic field. The magnitude of this shift is given by [159, p. 669]

$$\Delta E_{F,m_F} = \mu_\mathrm{B}\, g_F\, m_F\, B_z. \tag{4.5}$$

The probe transition in our experiments shifts by 1.39 MHz/G due to the Zeeman effect. Therefore, the earth magnetic field creates a shift of around 700 kHz $\cdot\, h$. Any such constant energy shift can be compensated by detuning the excitation laser in frequency by the same amount.

Our experiment relies on passive stability of the local magnetic field inside the vacuum chamber over the course of weeks.

The Zeeman shift does not scale with the principal quantum number n, because the magnetic moment primarily depends on the angular momentum quantum numbers. Therefore, the Zeeman shift is a relevant effect for both ground and Rydberg states.

During the initial setting up of the experiment, the orientation and magnitude of the total stray magnetic field inside the vacuum chamber is unknown. To begin with, we compensate for any stray magnetic fields to bring the hyperfine states into degeneracy. We extract the local stray magnetic fields from microwave spectroscopy. Figure 4.10(a) shows the two hyperfine ground states of rubidium-87 including their magnetic substates in the presence of an external field.

The three coil pairs in Helmholtz configuration outside the vacuum chamber can compensate for external homogenous magnetic fields. The magnetic substates in the atom are degenerate in the case of zero magnetic field, where the Zeeman energy shift vanishes.

We use the atoms to measure the present magnetic field by detecting the energy splitting between the magnetic substates. Therefore, we detect the population of the $F = 2$ state in probe beam transmission measurements. We start our sequence by transferring all atoms into the $F = 1$ states. Afterward, we apply a 2 ms long microwave pulse at 6.8 GHz with a microwave horn[17] to transfer atoms into the $F = 2$ states.

In Fig. 4.10(c), we show the transmission of our probe beam as a function of the microwave frequency. We detect a reduced transmission for microwave frequencies at which we drive $F = 1 \rightarrow F = 2$ transitions. For the applied magnetic field along the three dimensions of $\vec{B} = (22, 104, 316)$ mG in Fig. 4.10(c), we observe the seven expected microwave transitions indicated on the left side in Fig. 4.10(b). We fit Gaussian peaks to the transmission dips and extract a common splitting for this non-optimal compensation case.

The magnetic field gives rise to a residual level splitting of 16.4(1) kHz. These magnetic fields are already quite close to the optimal condition, as we started with a Zeeman splitting of ~ 300 kHz (not shown here). The different depths of the transmission dips comes from the inhomogeneous distribution of atoms across the initial magnetic substates. Imperfect depumping of the $F = 2$ manifold, gives rise to residual absorption of probe photon detuned from any microwave resonance. For $\vec{B} = (7, 123, 316)$ mG, we find a splitting of 3.53(4) kHz in Fig. 4.10(d).

[17] Flann Microwave 15094-SF40

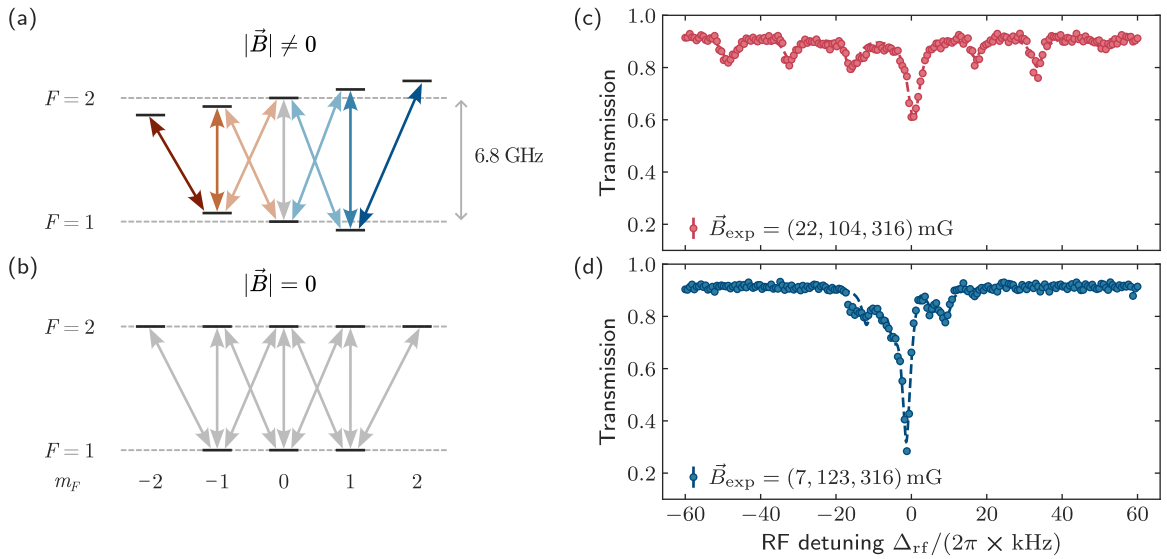

Figure 4.10: Hyperfine ground states of rubidium-87 in (a) the presence of external fields and (b) with compensated external fields. All possible microwave transitions around the 6.8 GHz ground state splitting are marked with arrows. (c), (d) Microwave spectroscopy for two different applied magnetic fields. The dashed lines show a model with seven Lorentzian absorption lines. Figure (c) and (d) adapted from Ref. [153].

With this almost vanishing magnetic field inside the vacuum chamber, we have a starting point to apply well-known magnetic fields pointing along the x-axis to define a quantization axis for the atoms.

After the compensation of stray magnetic fields, we create a magnetic field pointing in the x direction of Fig. 4.6(a). Thereby, the degeneracy of the magnetic substates in the hyperfine ground state of rubidium-87 is lifted. We define the quantization axis along this magnetic field to describe our atomic states in the hyperfine basis and drive $\sigma^{+(-)}$ transitions.

Figure 4.11(a) shows the hyperfine states relevant for the rubidium D2 line. In order to describe the atoms as a two-level system and describe the transmission by Eq. 4.4, the atoms have to be prepared in the target state $|F = 2, m_F = 2\rangle$. From this state, the probing transition $|F = 2, m_F = 2\rangle \rightarrow |F' = 3, m_F = 3\rangle$ is a closed transition. However, the atoms are distributed over the different magnetic substates after the initial trapping and cooling steps. Atom preparation in the target state is done by optically pumping the atoms with two σ^+ polarized beams. The beam on the $F = 2 \rightarrow F' = 2$ transition increases the magnetic quantum number by one, with $\Delta m_F = +1$ upon excitation. Afterward, the atom can spontaneous decay with $\Delta m_F = 0, \pm 1$. Over time, all the atoms will accumulate in the dark state $|F = 2, m_F = 2\rangle$ from where no excitation is possible. The atoms can fall from the $F' = 2$ manifold into the states with $F = 1$, which would remove them from the pumping cycle. A second beam, that is detuned by 6.8 GHz, is used to repump the atoms out of the $F = 1$ manifold. In the experimental setup, both beams are overlapped and denoted in the following as the optical pumping beam. We optimize the optical pumping into the dark state by adjusting the detuning of the optical pumping and repumper beam as well as their optical power.

Figure 4.11(b) shows the optical density measurement performed on the $F = 2 \rightarrow F' = 2$ and $F = 2 \rightarrow F' = 3$ transition. We calculate a state preparation in the state $|F = 2, m_F = 2\rangle$ with respect to the other $|F = 2\rangle$ states of 99.6 % from the respective optical densities. After the atoms are prepared

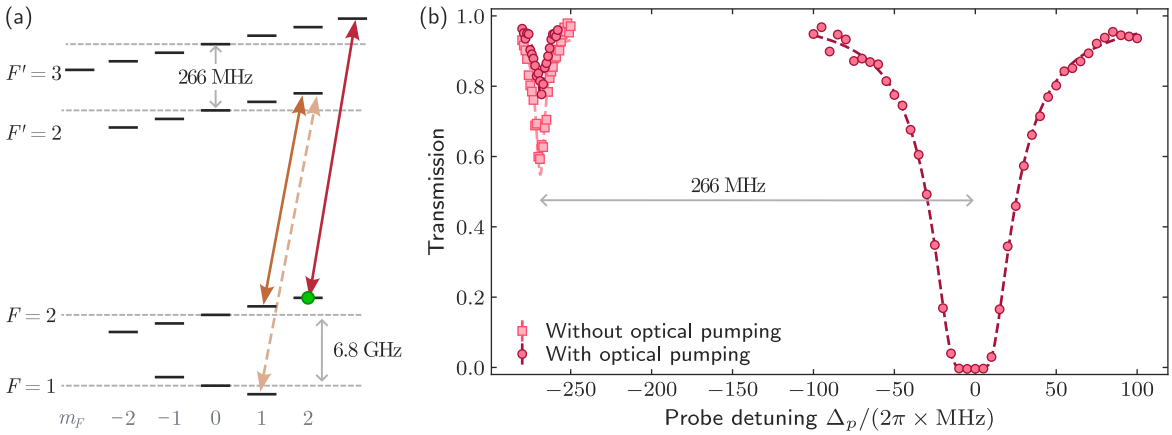

Figure 4.11: (a) Relevant hyperfine states of rubidium-87 D2 line with a small magnetic field applied. The atoms are optically pumped by a polarizer beam (orange, solid arrow) and a repumper beam (orange, dashed arrow). (b) Transmission through the atomic cloud as function of the probe beam detuning Δ_p. The atoms absorb the probe light at $\Delta_p/2\pi = 0$ MHz on the $F = 2 \rightarrow F' = 3$ transition and at $\Delta_p/2\pi = -266$ MHz on the $F = 2 \rightarrow F' = 2$ transition. The absorption on the latter with optical pumping (dark red, circles) is significantly reduced compared to the case without optical pumping (light red, squares) applied.

in the state $|F = 2, m_F = 2\rangle$ in the experimental cycle, we can excite them into Rydberg states.

4.3 Excitation and Detection of Rydberg Atoms

In this section, we discuss the implementation of the Rydberg experiments introduced in Chapter 2. All the experiments are performed with the un-trapped cloud of atoms in accordance with the transmission measurements in Fig. 4.9.

First, we present the measurements for EIT, slow light, and photon storage and retrieval experiments as introduced in Chapter 2. In the end, we outline how we detect and compensate stray electric fields in the vacuum chamber.

4.3.1 Measurements of Electromagnetically Induced Transparency

Figure 4.12(a) shows the two-photon excitation scheme to excite a rubidium-87 atom into the Rydberg state nS. The excitation scheme follows the idea of the ladder EIT system discussed in Fig. 2.1, where we detect the transmission of the few 780 nm probe photons.

In the Rydberg experiments, the control laser couples the intermediate state $5P_{3/2}$ to a Rydberg state. The exact wavelength of the control laser depends on the principal quantum number n of the Rydberg state. In our experiments, we address Rydberg states from $45S$ to $108S$. Between these Rydberg states, the excitation wavelength from the $5P_{3/2}$ state changes from 480.5 nm to 479.3 nm.

We find the exact wavelength for one specific Rydberg state by intentionally degrading the MOT loading. For that purpose, the MOT is monitored in the fluorescence imaging without cycling the experiment. The control laser wavelength is changed until the MOT signal gets fainter, and that is exactly at a wavelength when the control laser couples the excited state of the MOT cooling transition, $5P_{3/2}$, to a Rydberg state and interrupts the MOT cooling cycle. The wavelength of the laser is

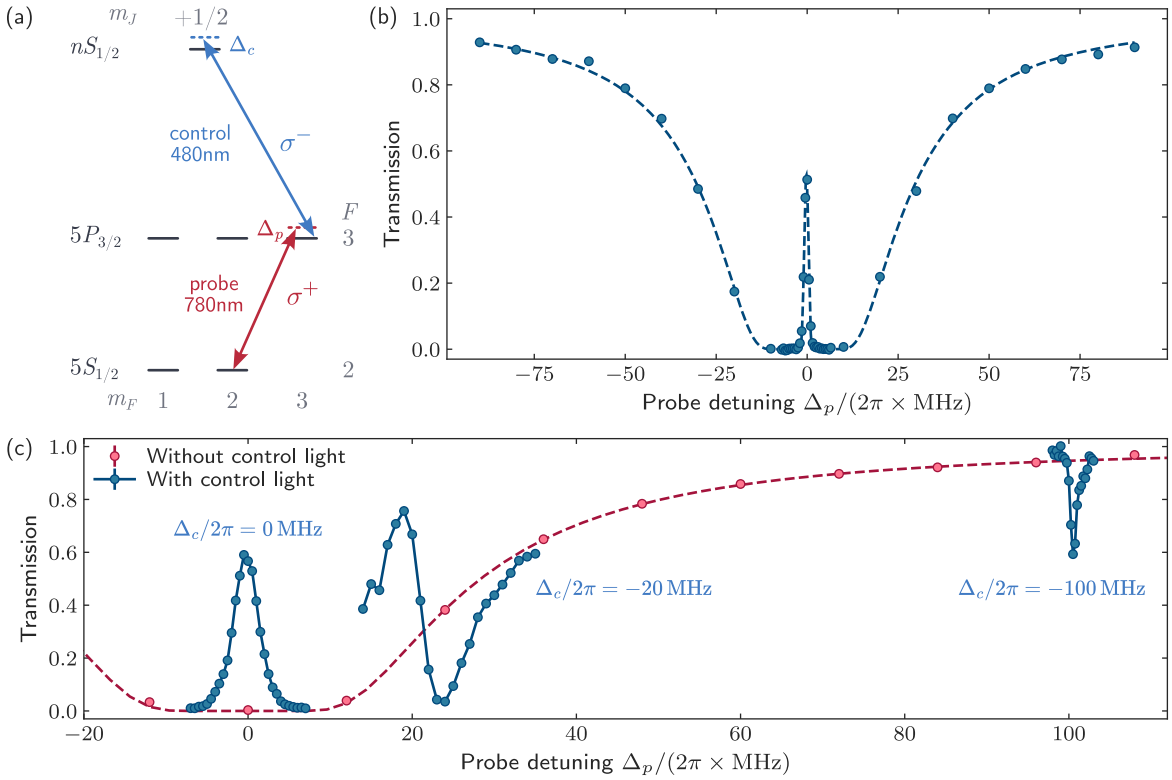

Figure 4.12: (a) Relevant energy levels in rubidium-87 for our two-photon transition. The probe and control beam have a single-photon detuning of Δ_p and Δ_c, respectively, and the two-photon transition has a two-photon detuning of $\delta = \Delta_c - \Delta_p$. (b) Electromagnetically induced transparency for the $89S$ Rydberg state. Each detuning data point is an average over 7000 repetitions. The dashed line fit is given by the transmission in Eq. 2.2 and the susceptibility in Eq. 2.1. (c) Transmission of probe photons in the absence (red) and presence (blue) of the control light. The control detuning $\Delta_c/2\pi$ is set to 0 MHz, −20 MHz, and −100 MHz with respect to the resonance of the Rydberg state $108S$.

monitored with the wavelength meter to an absolute accuracy of 200 MHz. Thereby, we can resolve e.g. the Rydberg state $108S$ from neighboring states, which are detuned by 5.6 GHz according to Eq. 2.10.

Figure 4.12(b) shows the EIT transmission window, where the probe photons can pass the atomic cloud on two-photon resonance with $\delta = \Delta_c - \Delta_p = 2\pi \times 0\,\mathrm{MHz}$ to Rydberg state $89S$. The detuning dependence follows the theoretical transmission shape with the susceptibility given in Eq. 2.1. We extract a control Rabi frequency of $\Omega_c/2\pi = 9.2\,\mathrm{MHz}$ and an optical depth of OD = 64. In Fig. 4.12(c), the power-broadened EIT window is measured with Rydberg state $108S$. Additionally, in Fig. 4.12(c), the two-photon excitation is measured for the same three values of the control detuning Δ_c as shown in Fig. 2.1(b). The three cases match with theoretical transition from the EIT case towards the two-photon Raman resonance.

4.3.2 Photon Storage Experiments with Atoms in Free Space

In our experiments, photon storage allows us to measure the temporal decay of collective Rydberg excitations within the atomic ensemble. We later use this decay behavior to investigate the conditions for magic trapping of these excitations.

During photon storage and retrieval, probe photons propagate through the trapped atomic cloud as Rydberg polaritons under Rydberg electromagnetically induced transparency (EIT), as introduced in Section 2.1.1. To ensure EIT resonance, both the probe detuning and the two-photon detuning are set to $\Delta_p/2\pi = \delta/2\pi = 0\,\mathrm{MHz}$.

The insert in Fig. 4.13(a) shows the measurement procedure: A probe pulse propagates through the atomic ensemble under EIT resonance conditions. The control field is then switched off and kept off for a variable duration, during which the probe pulse is stored within the ensemble. When the control field is turned back on, the probe pulse resumes its propagation through the medium.

Furthermore, Figure 4.13(a) shows the recorded single photon probe trace and timing for the control light in a typical photon storage and retrieval experiment. The incoming probe pulse is stored inside the atomic cloud, when the control laser is switched off. A small amount of probe photons is already transmitted during the storage process, where the control light is still on. No probe photons are detected until the control light is turned back on after a storage duration t_s. The control light converts the stored spin wave back into a propagating polariton, where the atomic coherence is mapped into a light field that leaves the cloud.

From the measured data in Figure 4.13(a), the retrieval efficiency η is calculated as

$$\eta(t_s) = \frac{S_{\mathrm{w/}}(t_s > 0.25\,\mu\mathrm{s})}{S_{\mathrm{w/o}}(t_s) - S_{\mathrm{w/}}(t_s < 0.25\,\mu\mathrm{s})}. \tag{4.6}$$

Here, $S_{\mathrm{w/}}$ denotes the summed probe photon trace recorded with atoms in the path, and $S_{\mathrm{w/o}}$ the trace without atoms. We only consider storage durations $> 0.25\,\mu\mathrm{s}$, to clearly distinguish the stored and retrieved photons from the transmitted photons during the storage process. Figure 4.13(b) shows the measured retrieval efficiency η as function of storage duration t_s, extracted from the measurement presented in Fig. 4.13(a).

It can be seen that the fraction of the stored probe pulse that is successfully retrieved decreases with increasing storage time, indicating that the collective excitation undergoes dephasing. Section 2.1.1 discussed various dephasing mechanisms, including motional dephasing caused by the thermal motion of the atoms. The temperature of the free-space atomic cloud is determined using a time-of-flight measurement to be approximately $T = 6.0(2)\,\mu\mathrm{K}$. For this temperature, the thermal decay model given in Eq. 2.7 yields a decay time constant of $\tau_{\mathrm{T},0} = 8.3(1)\,\mu\mathrm{s}$ for counter-propagating probe and control beams. For the measurement with the counter-propagating configuration, we extract a decay constant of $\tau_{\mathrm{T}} = 8.44(4)\,\mu\mathrm{s}$ from a fit to find a good match with the theoretical model. For comparison, the expected decay constant for a co-propagating configuration of probe and control beam would be $\tau_{\mathrm{T},0} = 1.97(3)\,\mu\mathrm{s}$.

In Fig. 4.13(b), a small oscillation of the retrieval efficiency as a function of storage time is visible for $t_s < 5\,\mu\mathrm{s}$. In this case, the oscillation comes from high atomic density, and the exact mechanism will be discussed in Chapter 5.

However, similar oscillations can also arise from other effects, such as more complex decay dynamics associated with the internal states of the atomic cloud. Next, we present an example of beating arising

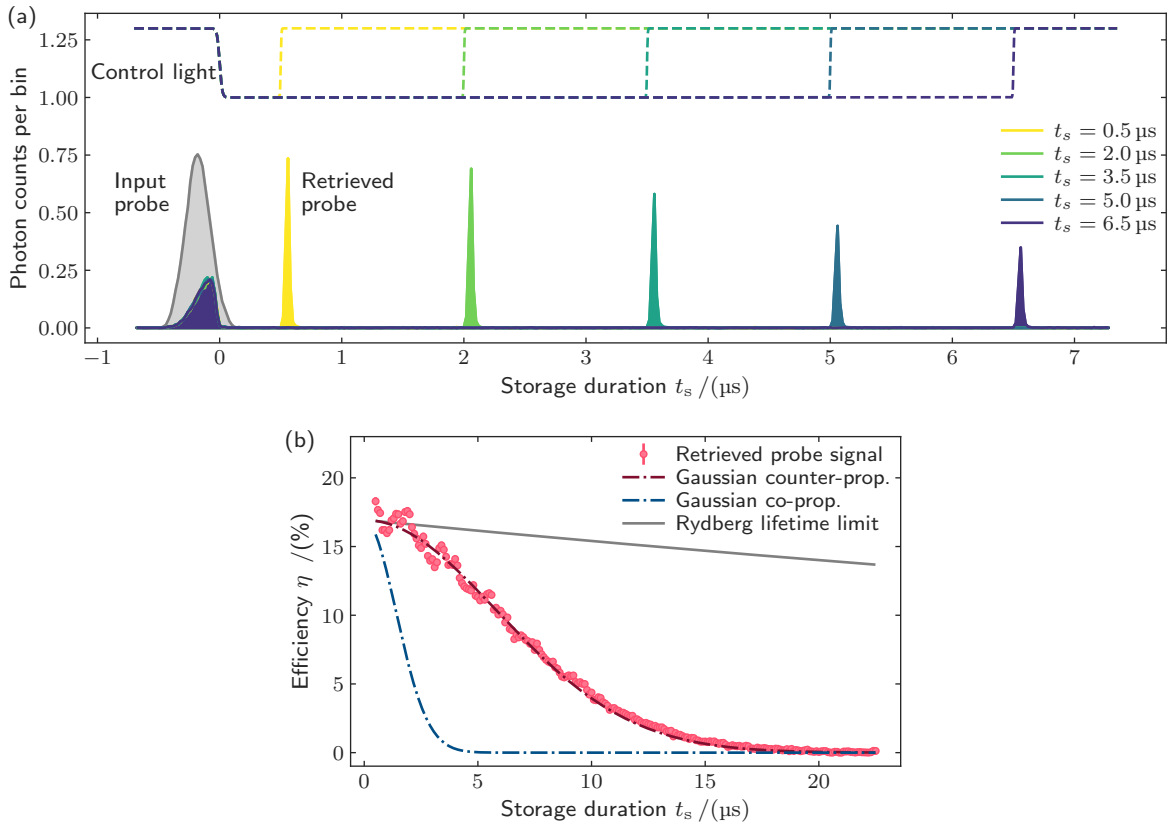

Figure 4.13: (a) Photon storage and retrieval measurement for Rydberg state $61S$. The input photon pulse (gray) is stored inside the atomic medium upon the switching off of the control light (dashed lines). The control light traces are not to scale and are only added for visualizing the sequence. A pulse of probe light is retrieved after the variable storage duration t_s by turning back on the control light. Each storage duration is measured separately, and the presented traces are averages of 71000 single measurements. The input probe pulse is recorded in the second half of our experiments without any trapped atoms. During the storage process, a small fraction of probe photons are simply transmitted or immediately read out. (b) Retrieval efficiency as function of storage duration t_s. The efficiency $\eta(t)$ is calculated with Eq. 4.6 from the data in (a). In this experiment, the atomic cloud is in free space and its temperature determined as $T = 6.0(2)\,\mu K$ by time-of-flight in absorption imaging. The two dash-dotted lines show the Gaussian decay envelope with the above temperature, assuming counter- (red) and co-propagating (blue) probe and control beams. The gray curve shows the coherence time limit given in Eq. 2.7 due to spontaneous decay and black-body induced transitions.

from different two-photon excitation pathways due to imperfect atomic state-preparation or imperfect probe and control polarization. If there are two or more possible two-photon transitions from the ground state towards the Rydberg state, a temporal beating in the retrieval efficiency $\eta(t_s)$ arises, and the beat frequency depends on the energy difference between the respective transitions. In our experiments, the atoms are prepared in the state $\left|5S_{1/2}, F = 2, m_F = 2\right\rangle$ to have a single excitation path towards the Rydberg state. However, in case of imperfect state preparation, the atoms are distributed over the different hyperfine states with quantum numbers m_F.

Figure 4.14(a) illustrates the excitation paths from different sublevels in the hyperfine ground state with the two-photon excitation towards a single Rydberg state. As discussed in Section 4.2, we apply

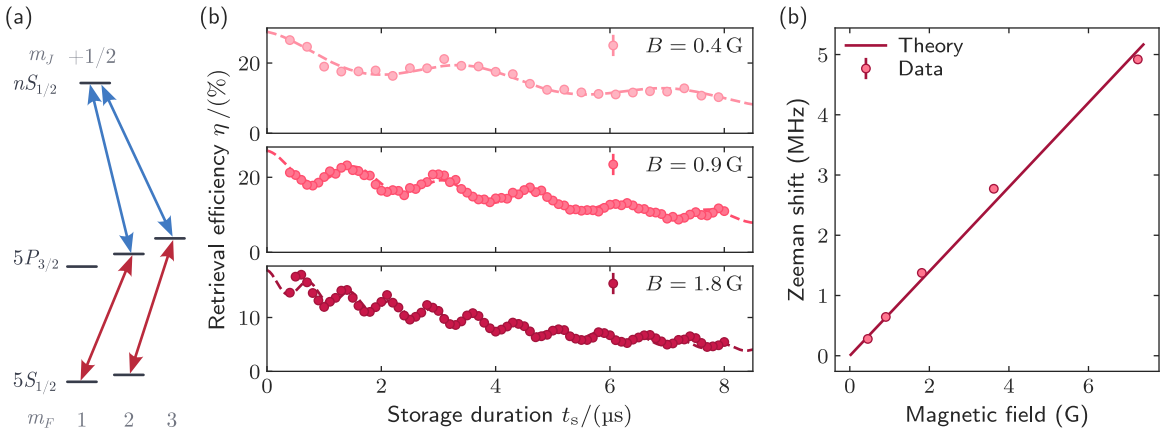

Figure 4.14: (a) Two different excitation paths from different Zeeman states towards the Rydberg state 45S. (b) Photon retrieval efficiency $\eta(t_s)$ for different external magnetic field strength and Rydberg state 45S. The dashed lines are fits of Eq. 4.7 with the envelope function discussed in the main text. (c) Zeeman shift extracted from fits in (b) as function of the applied magnetic field. The theoretical line follows the theoretical Zeeman splitting between two neighboring m_F ground states with a slope of 0.7 MHz/G.

a magnetic field to define a quantization axis and, to lift the degeneracy between the ground-state sublevels. This results in the Zeeman shifts of the different m_F states shown in Fig. 4.14(a), and the resulting energy differences lead to the observed beating. The two-photon excitation shows an interference between two neighboring hyperfine states.

Figure 4.14(b) shows the interference between two excitation pathways imprinted on the retrieved photon number. For this measurement, the atoms are distributed across multiple magnetic ground state states by deliberately using imperfect optical pumping. A similar beating in the retrieval efficiency as a function of storage duration has been observed in Ref. [43] and Ref. [160], where the collective state has been encoded in two different rubidium-87 hyperfine ground states. The decay signal involving states with a Zeeman splitting of Δ_{Zeeman} is given by [160]

$$\eta(t) = \eta_0 \cdot f(t) \cdot |u + (1-u)e^{-i2\pi\Delta_{\text{Zeeman}}t}|^2, \tag{4.7}$$

where u describes the population distribution between the different Zeeman states, and $f(t)$ is an overall decay envelope. For free space atoms, the decay envelope is given by a Gaussian function as discussed in Chapter 2. In the presented measurements, the atoms are not trapped in free space, but in a standing-wave trap that is covered later in Chapter 5. Due to the different trap, the model has an envelope of $f(t) = e^{-t/\tau_T}$.

From the retrieval efficiency data, the model can be used to extract the respective Zeeman splitting for a given applied magnetic field. Figure 4.14(c) shows the Zeeman shift Δ_{Zeeman} as function of magnetic field amplitude along the x direction. We observe a linear shift with the same slope as given by the theoretical Zeeman shift in Eq. 4.5 between two neighboring m_F states. For weak magnetic fields, the observed linear shift is only given by the ground state Zeeman splitting of 0.7 MHz/G. In the Rydberg state, the coupling between the nucleus and the outer electron is much lower compared to the ground or first excited states. Therefore, the energy levels and the respective Zeeman shift are described in the fine structure basis. The atoms are excited to a high-lying Rydberg state $|nS, J = 1/2, m_J = +1/2\rangle$,

which is the same final state for both excitation pathways in Fig. 4.14(a). The shift of the intermediate state $5P_{3/2}$ can be neglected in the two-photon excitation between a ground state and the Rydberg state. A slightly off-resonant excitation with respect to the intermediate state lowers the excitation probability from the secondary m_F state. As long as the ground state Zeeman shift is smaller than the intermediate state decay rate Γ_{D2}, the shift of the intermediate state does not change the beat frequency.

The optical pumping is optimized as discussed in Section 4.2 to not observe the interference of multiple Zeeman levels.

Figure 4.15 shows the difference that the correct state preparation has on the photon storage and retrieval experiments. In the measurement without optical pumping, a fit of Eq. 4.7 extracts a $u = 71.3(9)\,\%$. The relative population between the target ground state and the other Zeeman states is optimized by optical pumping to $u = 99.4(3)\,\%$, which is equal to the value derived from the measured residual absorption in Section 4.2. We attribute the overall increased retrieval efficiency to a more efficient storage and retrieval process starting from the target ground state.

Based on these measurements, we confirm the successful preparation of the same ground state across the whole atomic ensemble.

4.3.3 Compensation of External Electric Fields

Stray electric fields at the position of the atomic cloud can lead to inhomogeneous and instable energy shifts of the Rydberg state. This DC Stark shift [161] is driven by the interaction between the electric field and the dipole moment of the atom. The dipole moment is proportional to n^2 and makes Rydberg states especially sensitive to electrical fields. Here, we introduce this energy shift and explain our methods to detect and compensate for it.

We apply time independent perturbation theory to get the impact of a weak electric field on the atomic levels of Rydberg atoms. As outlined in Section 3.1.2, the energy correction δE_q for the state $|q\rangle$ subject to a perturbation $\hat{V}$ is expressed as

$$\delta E_q = \langle q|\hat{V}|q\rangle + \sum_{j\neq q} \frac{\left|\langle q|\hat{V}|j\rangle\right|^2}{E_q^{(0)} - E_j^{(0)}}. \tag{4.8}$$

The perturbation Hamiltonian for a Rydberg atom placed in a weak electric field $\boldsymbol{E}$ is given by $\hat{V} = e|\boldsymbol{E}|x$ as function of position x. We calculate the two terms in Eq. 4.8 for this perturbation. The first term evaluates the expectation value for an antisymmetric function, which vanishes for identical states. The coupling between different Rydberg states in the second term in Eq. 4.8 leads to a quadratic scaling of the energy correction with the electric field amplitude. For non-degenerate S-states, we write the energy shift due to an electric field E as

$$\delta E_{\mathrm{Stark}} = \frac{1}{2}\alpha_{\mathrm{static}} E^2, \tag{4.9}$$

where the static polarizability α_{static} is given by Eq. 2.12. In the presence of an external field E_{ext}, a controlled electric field E_{comp} can be applied for compensation with

$$\delta E_{\mathrm{Stark}} = \frac{1}{2}\alpha_{\mathrm{static}} (E_{\mathrm{ext}} - E_{\mathrm{comp}})^2. \tag{4.10}$$

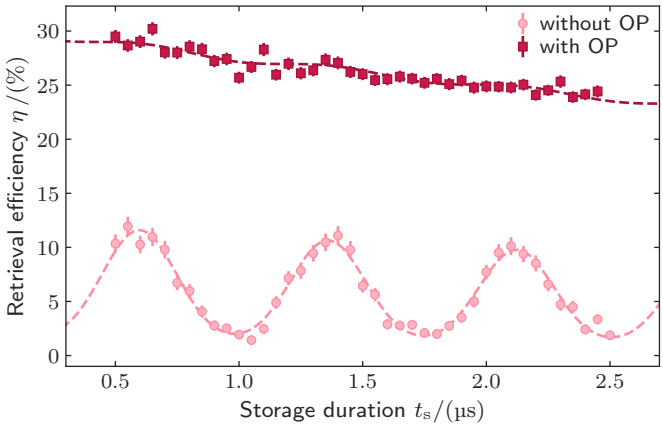

Figure 4.15: Photon storage and retrieval performed on an atomic cloud without (light red, circles) and with (dark red, squares) optical pumping. The dashed lines are fits of Eq. 4.7 with the envelope function discussed in the main text.

For a compensated external field, the two-photon transition is to first order insensitive to changes in the external electric field.

We utilize the atoms themselves as a probing device for the presence of external electric fields. In Fig. 4.16(a), we show the shift of the two-photon Raman resonance as function of an applied electric field E_z in the z direction. The local electric field is generated with in-vacuum electrodes [129]. We shift the two-photon Raman resonance by applying the electric field. From the scaling, we can extract the degree of electric field compensation as well as the static polarizability α_{static} for the given Rydberg state. In the upper panel, we show the Stark map in the presence of a not perfectly compensated external field. The compensation field E_{comp} does not cancel the external field as visualized by the vectors in the small inset. In the lower panel, we apply the correct compensation field, denoted as $E_{i,0}$, for the direction i. The compensation of external fields makes the two-photon Raman resonance less sensitive to electric fields and ensures that the two-photon excitation stays on resonance.

In Fig. 4.16(b), we show the compensation electric field magnitude $E_{i,0}$ in the three spatial directions over the period of four months.

Any dust close to the vacuum chamber can carry electrical charges and changes the local electric field inside the vacuum chamber. To keep a stable and clean environment, we have a laminar flow of dust-filtered air coming in through the top of the optical table enclosure. The inflow of air keeps a slight overpressure on the optical table and prevents dust from settling close to the vacuum chamber.

Figure 4.16(c) shows the scalar polarizability α_{Stark} for Rydberg states $nS_{1/2}$ as function of the principal quantum number n. Each data point and uncertainty is derived from the average and the standard deviation of at least four measurements as shown in Fig. 4.16(a). We find a good agreement with the calculated polarizabilities in Eq. 2.12.

4.3.4 Field Ionization of Rydberg Atoms

The compensation of stray electric fields described in the previous section requires that the fields created by residual charges varies only on much longer time scales than our experiments. On the much shorter timescale from probe pulse to probe pulse, any residual Rydberg atoms from previous

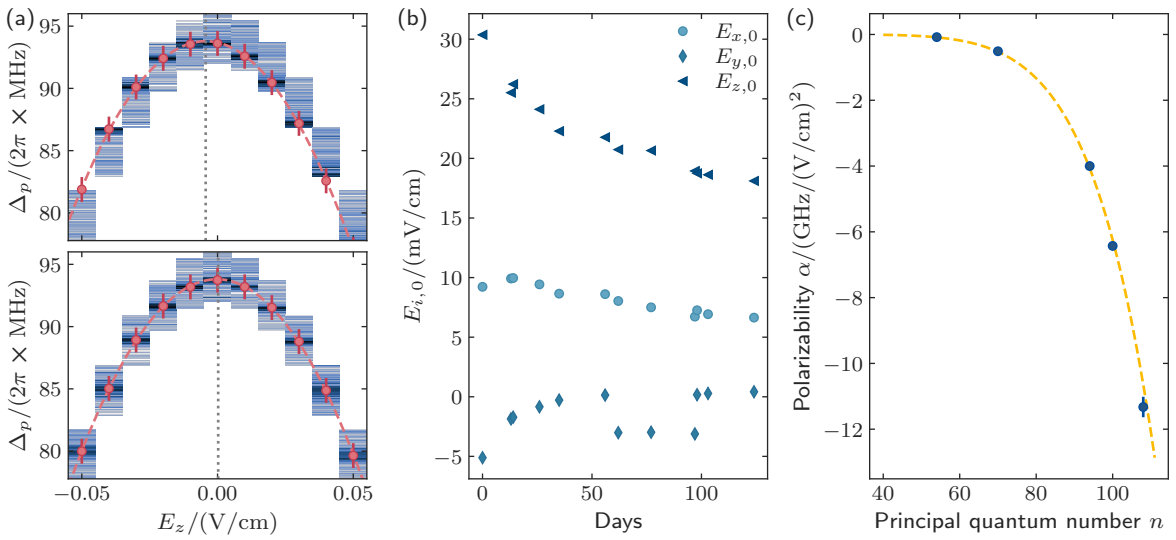

Figure 4.16: (a) Stark maps of the two-photon Raman resonance to Rydberg state 108S. The red markers show the two-photon Raman resonance detuning determined from Lorentzian fits to the transmission along the probe detuning Δ_p axis. The upper map shows the case with a residual external electric field of 4 mV/cm, indicated by the vertical gray dotted line. In the lower map, the correct compensation field $E_{z,0}$ is applied to cancel an electric field. The red dashed lines are fits of Eq. 4.10 to the two-photon Raman resonance shifting with respect to the applied electric field to extract the static polarizability α_{static} and residual electric fields E_{res}. (b) The change of applied electric field components $E_{i,0}$ to compensate external electric fields. (c) The static polarizability α_{static} as function of principal quantum number n. The yellow dashed line shows the expected polarizability according to Eq. 2.12.

transmission measurements can influence subsequent measurements. The interaction between two Rydberg atoms is required and favorable for the Rydberg quantum optics experiments discussed in Section 2.3, but can hinder high repetition rate experiments. The timescale is limited on one hand by the lifetime of the Rydberg state.

In our experiments is the duration between two probe pulse experiments at least 50 µs. This is too short in comparison to the effective Rydberg state lifetimes in Eq. 2.16. On the other hand, the dipole trap that confines the ground-state atoms between each probe experiment repels the Rydberg atoms as discussed in Chapter 3.

In order to further ensure the reproducibility of the 1000 experiment pulses, we remove any remaining Rydberg atoms by field ionization with the in-vacuum electrodes [129].

The required electric field to ionize a Rydberg atom in a Rydberg S-state with effective principal quantum number n^* is given by [101]

$$|E| = \frac{\pi \epsilon_0 R_{\text{Ryd}}^2}{e^3 n^{*4}}. \tag{4.11}$$

This ionization electric field is shown Figure 4.17(a) together with the highest ionization field V_{ion} that can be produced in our setup. Due to the geometry of the electric field electrodes and the voltage supply, Rydberg states as low as $n = 47$ can be ionized. The ionization voltage V_{ion} is applied generally after 21 µs in Fig. 4.9(c). We measured a minimal ionization duration of 0.4 µs to ionize Rydberg

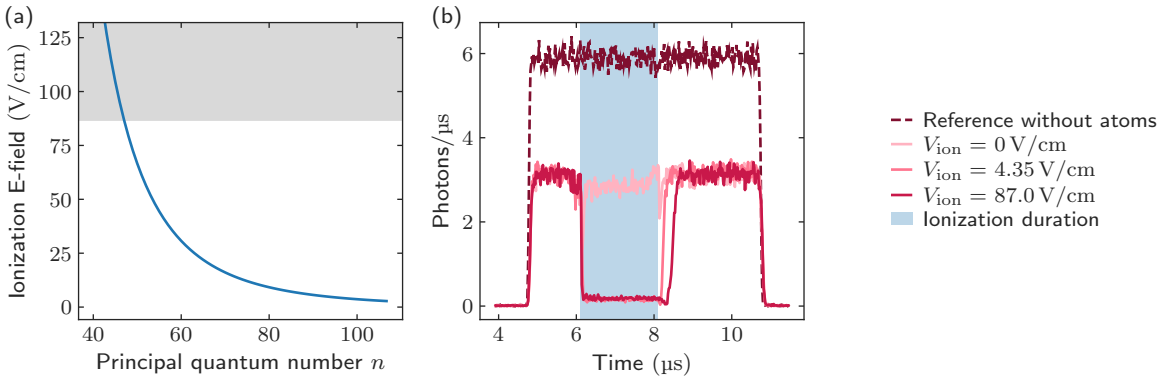

Figure 4.17: (a) The electric field strength that is required to ionize a Rydberg state with principal quantum number n as given in Eq. 4.11. The gray shaded area marks the fields that cannot be achieved with our experimental setup. (b) Probe transmission pulses with Rydberg state 61S for different peak ionization voltages V_{ion}. The probe laser is detuned by 4 MHz to the side of the EIT window in Fig. 4.12. The dashed line is a reference pulse measured without atoms. An electrical field with different strength is applied during the blue shaded ionization duration.

state 61S.

The large ionization fields in Fig. 4.17(a) can themselves disturb the subsequent probe pulse measurement. A moderate field of 30 mV/cm shifts the Rydberg resonance by 5 MHz, as shown in Fig. 4.16(a).

In Fig. 4.17(b), the recovery of an EIT condition is observed after an ionization pulses ended. The three measurements with the atoms (solid lines) are performed with a probe detuning of $\Delta/2\pi = 4\,\mathrm{MHz}$, which corresponds to the slope of the EIT window and makes the measurements more sensitive for electric field changes. Even for the highest ionization fields of 87 V/cm, the EIT condition is recovered after less than 0.4 µs. The measurement in Fig. 4.17(b) is performed with Rydberg state 61S, with a static polarizability of $\alpha_{\mathrm{static}} = 201.4\,\mathrm{MHz}/(\mathrm{V/cm})^2$. In a measurement for Rydberg state 89S with $\alpha_{\mathrm{static}} = 2764\,\mathrm{MHz}/(\mathrm{V/cm})^2$, we find a recovery of the EIT condition within 1.5 µs. This longer settling time can be avoided by applying a lower ionization fields V_{ion}, shown in Fig. 4.17(b), while the higher Rydberg states still are ionized according to Fig. 4.17(a). From this data, we conclude that the electric fields from the ionization pulse are not influencing our measurements.

CHAPTER 5

Collective Rydberg Excitations in Magic Traps

In the photon storage and retrieval experiments presented in Chapter 4, the atoms were released from the optical trapping potential during the measurement sequence. However, it is also possible to create an optical potential that confines the atoms in both their ground state and the relevant Rydberg state by coupling the Rydberg state to lower-lying states.

This chapter describes our experimental implementation of two such magic traps: a running-wave and a standing-wave configuration. We present the characterization of these traps and the procedure used to determine the magic wavelengths experimentally. Throughout this chapter, the formalism developed in Chapter 3 is applied to evaluate the differential light shifts between the ground and Rydberg states. For clarity, we use the term *one-dimensional trap* to refer to the traps formed by a single beam propagating along the x-axis.

5.1 Near-Resonant Trap for Rydberg Atoms

For the magic one-dimensional trap for rubidium-87, we use a laser at a wavelength of around 1012 nm. This laser is far off-resonance with respect to the lowest two transitions from the ground state in rubidium-87 at 795 nm (D1-line) and 780 nm (D2-line) [131, 132]. For the purpose of magic trapping, the laser is tuned close to the resonance between the Rydberg state and the lower-lying $6P_{3/2}$ state.

5.1.1 Optical Setup for the One-Dimensional Traps

Figure 5.1(a) shows the arrangements of optics around the experimental chamber to realize the one-dimensional traps. Both one-dimensional traps are aligned along the probing axis as shown in Fig. 4.6. The beam is coupled out of a single mode fiber and linearly polarized by a PBS. To control the beam waist and focal position inside the vacuum chamber, a demagnifying telescope with two plano-convex lenses in a $4f$ configuration and focal lengths of 400 mm and 50 mm is employed. The trap beam is overlapped with the probe beam on a dichroic mirror as shown in Fig. 4.6. The combined beam is focused into the vacuum chamber with the 50 mm lens.

Figure 5.1(b) shows the calculated radial beam waist for the incident trap beam. As the trap beam waist at the atoms cannot be measured directly, we use the calculated value of 24 µm in rest of this thesis. For the beam path after the atoms, an identical optical setup is placed behind the vacuum chamber. The 50 mm lens collimates the beams again, and the trap light is focused with a

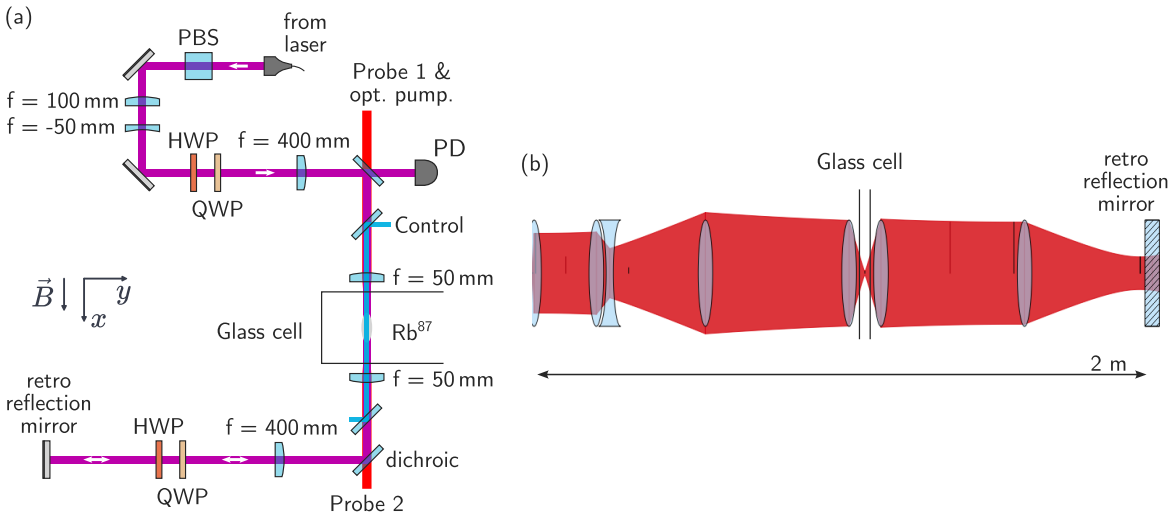

Figure 5.1: (a) Optical setup to create a one-dimensional trap in vacuum chamber. The trap is overlapped with the probe beam on two dichroic mirrors, as also indicated in Fig. 4.6. The laser intensity is stabilized using feedback from a signal detected by a photodiode (PD). (b) Theoretically calculated beam waist along the optical path. The first lens on the left is the fiber out-coupling lens and the trap light is retro-reflected on the mirror on the right side. The center $4f$ setup creates a focus at the same spot as the probe beam. An additional demagnifying telescope allows adjusting the waist size in the focal point.

400 mm lens onto a retro-reflection mirror. This setup allows the creation of the two different trapping geometries, that are relevant in this thesis. To create a standing-wave trap, the retro-reflection mirror is positioned such that the reflected beam is focused at the same position in the vacuum chamber. For the running-wave trap configuration, the trap beam is blocked in front of the retro-reflection mirror.

The electric field of one trapping beam, with polarization vector $\boldsymbol{\epsilon}_{\rightleftarrows}$, is given by

$$\boldsymbol{E}_{\rightleftarrows}(\rho,x) = E_{0,\rightleftarrows}\boldsymbol{\epsilon}_{\rightleftarrows}\frac{w_0}{w(x)}\exp\left(-\frac{\rho^2}{w(x)^2}\right)\exp\left(\mp ikx\right),$$

where the direction of the subscript arrow denotes the direction of the beam as introduced in Chapter 3. $\rightarrow$ denotes the case of the incoming beam, and $\leftarrow$ denotes the retro-reflected beam. The intensity profile of the running-wave trap is given by

$$I_{\mathrm{rw}}(\rho,x) \propto |\boldsymbol{E}_{\rightarrow}(\rho,x)|^2 = E_{0,\rightarrow}^2\frac{w_0^2}{w^2(x)}\exp\left(-\frac{2\rho^2}{w(x)^2}\right).$$

For two counter-propagating electric fields, the intensity distribution is given by

$$\begin{aligned} I(\rho,x) &\propto |\boldsymbol{E}_{\rightarrow}(\rho,x) + \boldsymbol{E}_{\leftarrow}(\rho,x)|^2 \\ &= |E_{0,\rightarrow}|^2 + |E_{0,\leftarrow}|^2 + E_{0,\rightarrow}E_{0,\leftarrow}\left[\boldsymbol{\epsilon}_{\rightarrow}\boldsymbol{\epsilon}_{\leftarrow}^*\exp(-2ikx) + \boldsymbol{\epsilon}_{\rightarrow}^*\boldsymbol{\epsilon}_{\leftarrow}\exp(2ikx)\right]. \end{aligned} \tag{5.1}$$

The intensity of the standing wave shows an interference pattern depending on the polarization products. To form a standing-wave trap, we require $\boldsymbol{\epsilon}_{\rightarrow}\boldsymbol{\epsilon}_{\leftarrow}^* = \boldsymbol{\epsilon}_{\rightarrow}^*\boldsymbol{\epsilon}_{\leftarrow} > 0$. In the ideal case of maximal

interference, the intensity distribution of the standing wave is given by

$$I_{\mathrm{sw}}(\rho, x) \propto \left[E_{0,\rightarrow} - E_{0,\leftarrow}\right]^2 + 4E_{0,\rightarrow}E_{0,\leftarrow}\cos^2(kx).$$

Figure 5.1(a) shows our optical setup to control the polarization of the one-dimensional trapping beams. The polarization of the incoming beam is set to right-handed circular (resulting in σ^- at the atoms) with a combination of half-wave plate and quarter-wave plate, as shown in Fig. 5.1(a). To meet the constructive interference condition for a standing wave in Eq. 5.1, we set the polarization of the retro-reflected beam as left-handed circular (resulting in σ^- at the atoms) by a second set of wave plates. If the retro-reflected beam is set to be right-handed circularly polarized instead, it will not interfere with the incoming beam. This results in a running-wave trap with doubled intensity.

During the experimental cycle, atoms can be transferred into the one-dimensional trap from the crossed optical dipole trap. The loading of the crossed trap is discussed in Chapter 4. Figure 5.2(a) shows the timing sequence for the transfer of atoms from the crossed trap into the one-dimensional trap. The timing sequence is the same for the running-wave and standing-wave trap configuration. After the evaporation step in Fig. 5.2(a), the incoming beam power of the one-dimensional trap is increased linearly over 10 ms. The atoms are fully transferred into the one-dimensional trap by ramping the intensity of the crossed trap to zero linearly over 10 ms. During the ramp-down of the crossed trap, the power of the one-dimensional trap is also reduced to its final value. Then, we optically pump the atoms into the target state $\left|5S_{1/2}, F = 2, m_F = 2\right\rangle$. To verify that optical pumping works in the running- and standing-wave trap, we use the methods discussed in Chapter 4.

The resulting atom distributions in the different traps are illustrated by the absorption images in Fig. 5.2(b)-(e), where each image is recorded after sufficient holding time in each trap to capture the steady state distribution of the atomic cloud. To be specific, Figure 5.2(b) shows the atoms confined in the crossed trap, while Fig. 5.2(c) shows the atoms in the running-wave trap. Here, the atoms spread out from the initial position in the crossed trap. The shift of the atomic distribution is caused by an offset of the waist position of the one-dimensional trap beam by 600 µm from the position of the crossed optical dipole trap. To avoid the spread of atoms due to the focus offset, the crossed trap is pulsed on between the Rydberg experiments, as shown in Fig. 4.9(b), for Rydberg experiments with atoms confined in the running-wave trap. The resulting atom distribution of the running-wave and the crossed trap is shown in Fig. 5.2(d). Figure 5.2(e) shows the atomic cloud confined in the standing-wave trap. The shape is very similar to the one in the crossed trap, as the lattice wells prevent the atoms from spreading along the beam axis. This is only true if the standing-wave trap depth is higher than the kinetic energy of the atoms, which is the case for all the experiments presented in this thesis.

In the absorption images presented in Fig. 5.2(b-e), we demonstrate trapping of ground-state atoms in the one-dimensional trap, in both the running-wave and the standing-wave configuration.

5.1.2 Near-Resonant Coupling between the Rydberg and the 6P3/2 State

In order to create a magic trap, the trapping potential of the Rydberg state can be matched to the potential experienced by the ground-state atoms. Figure 5.3(a) shows how the 1012 nm light creates a near-resonant trap for the Rydberg atoms by coupling the Rydberg state $\left|nS_{1/2}\right\rangle$ to the hyperfine manifold of the $\left|6P_{3/2}\right\rangle$ state. The trap beam couples the Rydberg state to one or three hyperfine states in the $\left|6P_{3/2}\right\rangle$ states depending on its polarization. The quantization axis of our system, defined by

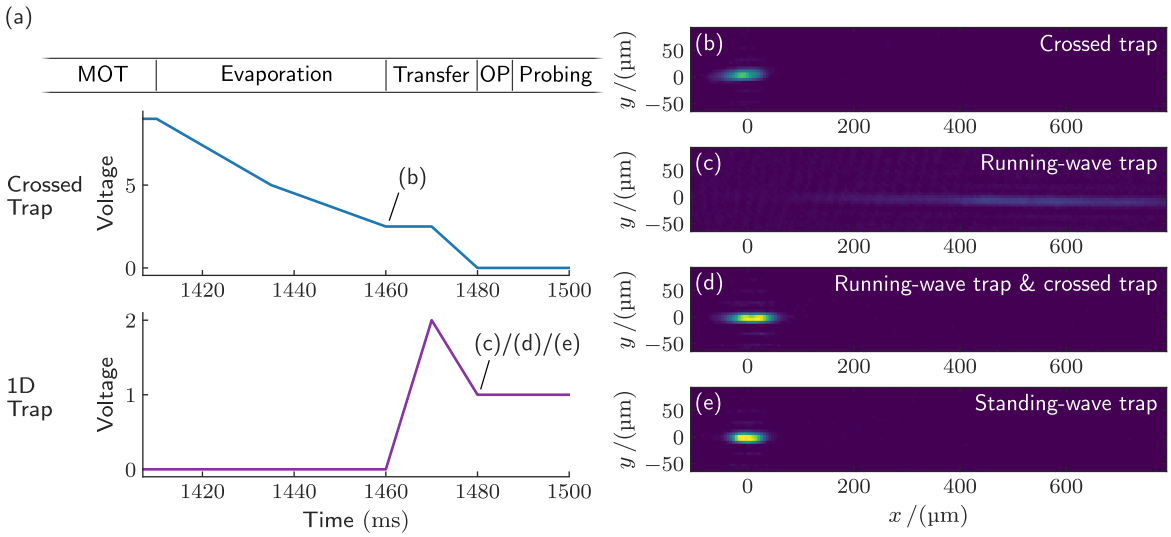

Figure 5.2: (a) Timing sequence used to load the atoms from the crossed optical dipole trap (blue) into the one-dimensional trap (purple). The voltage is proportional to the optical beam powers. (b)-(e) Absorption image of atoms recorded at $t = 1460\,\mathrm{ms}$, where (b) the atoms are trapped in the crossed optical dipole trap. Subsequently, the atoms are transferred into (c) the running-wave trap, (d) the running-wave together with the crossed trap or (e) the standing-wave trap. See main text for further details. The presented images are averaged over 20 shots.

the magnetic field along the y axis, restricts the trap beam to couple with transitions with σ^+, σ^- or a combination of the two. We define the trap laser detunig as $\Delta = \omega - \omega_{6n}$, where ω is the trap laser frequency and ω_{6n} is the transition frequency between the Rydberg state $|nS_{1/2}\rangle$ and the state $|6P_{3/2}, F = 3, m_F = 3\rangle$. Figure 5.3(b) and 5.3(c) shows the light shift of the two-photon resonance due to the coupling of the one-dimensional trap laser to the Rydberg state for σ^- and σ^+ polarization respectively. We observe the near-resonant coupling to the expected number of atomic levels as indicated in Fig. 5.3(a). The spacing between the levels matches with the known $6P_{3/2}$ hyperfine splitting [162]. For the rest of this thesis, we are working with the σ^- polarized trap, and the trap detunings will be given relative to the transition $|6P_{3/2}, F = 3, m_F = 3\rangle \leftrightarrow |nS_{1/2}, F = 3, m_F = 3\rangle$ as shown in Fig. 5.3(a).

The two-photon resonance shift presented here is given by the differential energy shift between the ground and Rydberg states. To be specific, the resonance features in Fig. 5.3(b) and 5.3(c) are given by the near-resonant energy shift of the Rydberg state in Eq. 3.29. The energy shift of the Rydberg state in can be used to match the shift of the ground state. This matching of trap potentials realizes a magic trapping condition between the two atomic states.

5.2 Magic Wavelength for the Ground-Rydberg transition

Figure 5.3 shows the tunability of the Rydberg state trapping potential. Thereby, we can minimize the differential light shift between the ground and Rydberg states. The differential light shift is generally

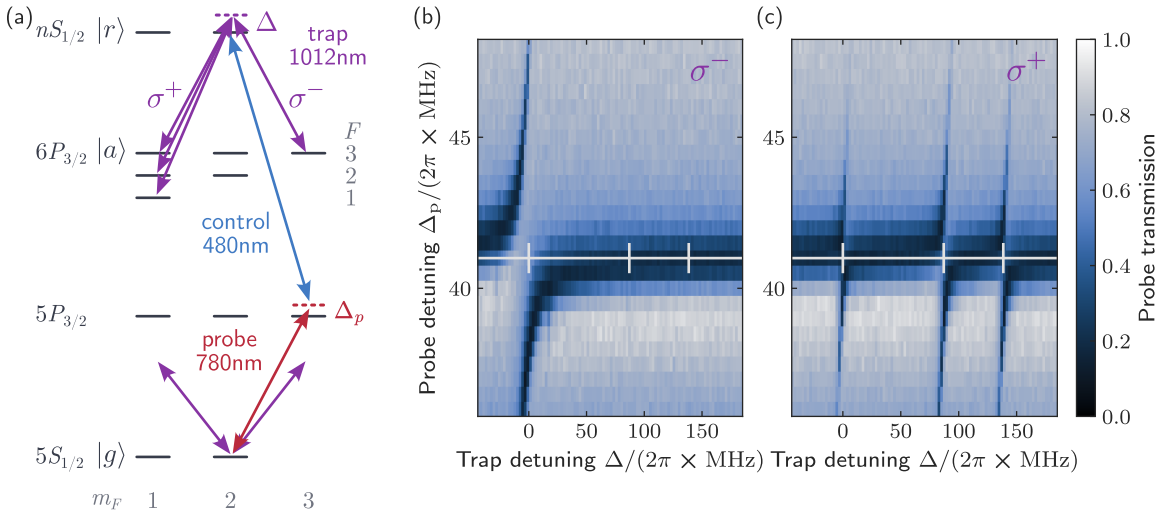

Figure 5.3: (a) Relevant level scheme of rubidium-87 for the two-photon excitation (red probe, and blue control) and the near-resonant trap laser (purple). The polarization of the incident trap beam defines the number of hyperfine states in the $|6P_{3/2}\rangle$ manifold the Rydberg state $nS_{1/2}$ is coupled to. (b), (c) Two-photon spectroscopy of the 108S Rydberg state level shift as function of the trap laser detuning Δ. The horizontal white line marks the probe detuning required to excite to the Rydberg state in the absence of the trap beam. The three small vertical lines show the hyperfine splitting between $|6P_{3/2}, F = 1, 2, 3\rangle$ [162]. We observe one or three avoided crossings, when the incident trap beam drives (b) σ^- or (c) σ^+ transitions, respectively. Figure adapted from Ref. [1].

given by

$$\begin{aligned}\delta U(\boldsymbol{r}, \Delta) &= U_n(\boldsymbol{r}, \Delta) - U_g(\boldsymbol{r}) \\ &= U_n(\rho, x, \Delta) - U_g(\rho, x),\end{aligned} \tag{5.2}$$

where we decompose the position $\boldsymbol{r}$ for parts of the following analysis into the radial coordinate ρ and the axial coordinate x. To calculate Eq. 5.2, the ground and Rydberg state trapping potentials from Chapter 3 are used. Specifically, we derive theoretical magic trapping conditions from the calculated potentials in Eqs. 3.25-3.27 and Eqs. 3.31-3.33. A similar analysis has been done in Ref. [60] for an almost perfect periodic potential.

For our experimental parameters and Rydberg state 76S, the differential light shift $\delta U(\boldsymbol{r}, \Delta)$ in a running-wave and a standing-wave trap are shown in Fig. 5.4. For the three different trap laser detunings Δ, the ground state polarizability shown in Fig. 3.2(a) is almost constant, and, thereby, the ground state trapping potential as well. It follows that the spatial distribution of ground-state atoms is not changing with the trap laser detuning. For the running-wave trap, the ground-state atoms form a continuous distribution, and for the standing-wave trap many flat disc-like distributions.

The investigation of the different rows in Fig. 5.4 allows the identification of the trap detuning at which the differential light shift $\delta U(\boldsymbol{r}, \Delta)$ is minimized. For the running-wave trap and Rydberg state 76S, the differential light shift vanishes for all positions at the detuning $\Delta_{76}^{\mathrm{rw}}$. For the running wave, it is possible to find a detuning Δ_n^{rw} for any Rydberg state with principal quantum number n,

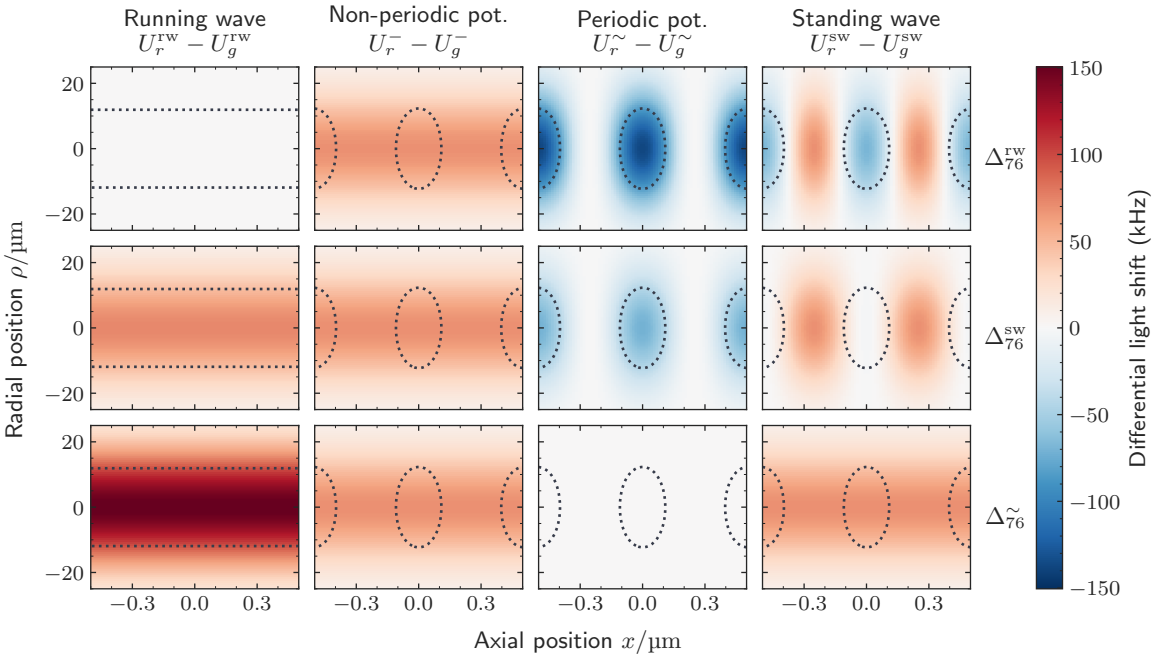

Figure 5.4: Differential light shift between the ground state and the Rydberg state 76S for different trap detunings Δ (rows) and trap shape (columns). The light shifts are calculated for the running-wave trap with Eqs. 3.25-3.27 and for the standing-wave trap with Eqs. 3.31-3.33 for radial position ρ and axial position x relative to the trap center. The gray dotted lines highlight the extent of the atomic cloud. They mark the positions where the mean thermal energy of the atoms is half of the ground state trapping potential. The first column shows the running-wave case. For the standing wave, we separately show the nonperiodic (–) (second column) and the periodic (~) (third column) contribution as well as the full standing wave case (fourth column). At the detuning $\Delta_{76}^{\mathrm{rw}}/2\pi$ = 336 MHz (top row), the differential light shift in the running wave case vanishes at every position. The same occurs for the periodic contribution at a detuning of $\Delta_{76}^{\sim}/2\pi$ = 548 MHz (bottom row). In the full standing wave, the differential light shift is minimized at $\Delta_{76}^{\mathrm{sw}}/2\pi$ = 413 MHz (center row), but does not vanish everywhere. Figure adapted from Ref. [1].

where $\delta U^{\mathrm{rw}}(\boldsymbol{r}, \Delta_n^{\mathrm{rw}}) = 0$. The magic detunings Δ_n^{rw} for the running wave satisfies

$$\frac{D_{an}^2}{4\hbar\Delta_n^{\mathrm{rw}}} + \alpha_f = \alpha_g, \tag{5.3}$$

where the ground state polarizability α_g is equal to the Rydberg state polarizability. This magic condition is only valid under the assumption that the electric field amplitudes do not vary over the size of the Rydberg atom given in Chapter 3. The scaling of magic detuning with n is determined by the $\propto (n^*)^{-3/2}$ scaling of the reduced dipole matrix element D_{an}, as discussed in Section 2.2. Therefore, to make a running-wave trap magic for higher Rydberg states, the trap laser has to be closer in frequency to the $6P_{3/2}$–$nS_{1/2}$ transition. For detunings larger than Δ_n^{rw}, the trap is more attractive for the ground state than for the Rydberg state. In contrast, the trap is more attractive for the Rydberg state than for the ground state for smaller detunings.

For the standing-wave trap, the differential light shift can be decomposed into components that are (non-)periodic along the x-axis as identified in Section 3.2.2. Figure 5.4 shows the nonperiodic

$\delta U^{-}(\boldsymbol{r},\Delta)$, periodic $\delta U^{\sim}(\boldsymbol{r},\Delta)$ and full standing wave differential light shift $\delta U^{\mathrm{sw}}(\boldsymbol{r},\Delta)$. The periodic potential contribution shown in the third column of Fig. 5.4 is zero for the detuning $\Delta^{\sim}_{76}$ independent of position. As for the running-wave configuration, we can identify the trap detuning, that fulfills $\delta U^{\sim}(\boldsymbol{r},\Delta^{\sim}_n) = 0$, as

$$\frac{D^2_{an}}{4\hbar\Delta^{\sim}_n} + \alpha_f \cdot \theta_n = \alpha_g. \tag{5.4}$$

The difference between the magic condition for a running wave (Eq. 5.3) and the magic condition for the periodic potential contribution is the landscape factor θ_n introduced in Section 3.2.2. For low principal quantum numbers with $\theta_n \approx 1$, the two conditions are the same, but they differ more for higher principal quantum number, where $\theta_n \to 0$ as already shown in Fig. 3.5(b). The magic detuning for the periodic potential contribution $\Delta^{\sim}_n$ has to be adapted for trapping a high n Rydberg atom in the periodic potential.

While it is possible to zero the differential light shift for a perfect periodic potential, this is not the case for the standing-wave trap used in the experiment. For a standing-wave trap, the differential light shifts are not only given by the periodic potential contributions $\delta U^{\sim}(\boldsymbol{r},\Delta)$, but also the nonperiodic contributions $\delta U^{-}(\boldsymbol{r},\Delta)$. The fourth column in Fig. 5.4 shows the full standing wave differential light shift $\delta U^{\mathrm{sw}}(\boldsymbol{r},\Delta)$, which is a sum of the periodic and nonperiodic contributions for Rydberg state $76S$. There is no trap detuning Δ, where the differential light shifts vanish for all positions. Therefore, we cannot find an analytic condition for the standing-wave trap magic detuning Δ^{sw}_n that fulfills $\delta U^{\mathrm{sw}}(\boldsymbol{r},\Delta) = 0$ independently of position. It is however possible to minimize the differential light shifts across the atomic cloud distribution, as visible in the middle row of Fig. 5.4.

To determine such optimal detunings, we turn to an experimental investigation for the running-wave and the standing-wave trap in the next section.

5.2.1 Measuring the Differential Light Shift on the Two-Photon Resonance

To investigate the effects of differential light shifts, we perform spectroscopy measurements. They can be understood as probing of the ground-to-Rydberg transition frequency for a single atom in the atomic cloud.

For the standing-wave configuration, we investigate how the two-photon resonance between ground and Rydberg state shifts as a function of the trap laser detuning Δ, as illustrated for Rydberg state $70S$ in Fig. 5.5(a). The probe detuning to address the two-photon Raman resonance $\Delta_{p,\mathrm{R}}$ are extracted with Lorentzian fits from spectroscopy measurements similar to the one shown in Fig. 4.12(c) with $\Delta_c = -2\pi \times 100\,\mathrm{MHz}$. The gray horizontal line in Fig. 5.5(a) shows the probe detuning required to drive the two-photon Raman transition in a measurement with un-trapped atoms. The magic detuning $\Delta^{\mathrm{sw}}_{70}$ for the standing-wave trap can be identified as the detuning where the red data points match the free-space resonance line. At this trap detuning, the trapping potentials for the atoms in the ground and Rydberg states $70S$ are equalized. This experimentally determined magic detuning can be compared to the detunings identified by the analytical conditions in Eq. 5.3, and Eq. 5.4. The magic detunings for the running wave $\Delta^{\mathrm{rw}}_{70}$ and the periodic potential $\Delta^{\sim}_{70}$ are marked as the blue and the yellow line, respectively.

From the experimental results of the standing wave, it can be seen that the measured optimal detuning is between the two analytical magic conditions. In an independent measurement, we identify the trap detuning $\Delta = 2\pi \times 453(1)\,\mathrm{MHz}$ where the two-photon Raman resonance becomes independent

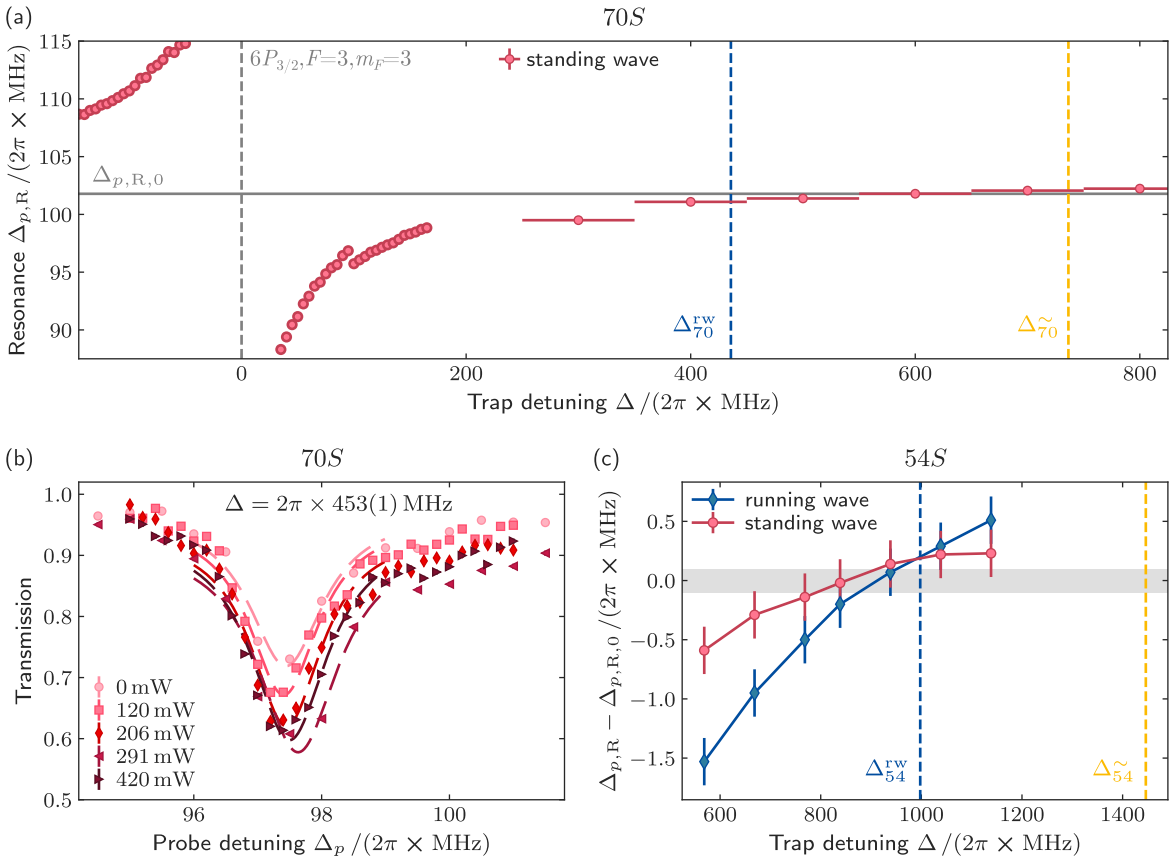

Figure 5.5: (a) Two-photon Raman resonance $\Delta_{p,\mathrm{R}}$ to Rydberg state $70S$ as function of trap detuning Δ, for atoms confined in the standing-wave trap. The red data points are measured similar to Fig. 5.3(a), with each data point extracted as the resonance center along the probe detuning axis. The higher trap detuning was set by monitoring the trap laser wavelength with a wavelength meter, while the lower trap detunings were measured after stabilizing the trap laser onto the reference cavity discussed in Section 4.1. The solid gray horizontal line shows the probe detuning for the two-photon Raman resonance $\Delta_{p,\mathrm{R},0}$ measured with free-space atoms. The gray dashed vertical line marks the resonance of $|6P_{3/2}, F = 3, m_F = 3\rangle$ for the σ^- polarized trap. The blue and yellow dashed lines mark the theoretical magic detuning of the running wave $\Delta^{\mathrm{rw}}_{70} = 2\pi \times 436\,\mathrm{MHz}$ and the periodic potential $\Delta^{\sim}_{70} = 2\pi \times 736\,\mathrm{MHz}$, respectively. (b) Two-photon Raman resonance to the Rydberg state $70S$ for different standing-wave trap beam powers. The atoms are confined in the standing-wave trap and the trap laser wavelength is set to a detuning of $\Delta = 2\pi \times 453(1)\,\mathrm{MHz}$. The dashed lines are Gaussian fits to visualize that the two-photon Raman resonance between the ground and Rydberg states does not shift with increasing beam power. (c) Two-photon Raman resonance shift for Rydberg state $54S$ with respect to the free-space-atoms resonance $\Delta_{p,\mathrm{R},0}$. The blue diamonds and the red circles show the running-wave and standing-wave trap measurements, respectively. The gray shaded area shows the standard deviation of the measurement with free-space atoms.

of the trap beam power. At this detuning, Figure 5.5(b) shows that the two-photon Raman resonance for the Rydberg state $70S$ becomes independent of the trap beam power. It is possible to find such an optimal detuning for all Rydberg states.

The shift of the two-photon Raman resonance can be used to measure the individual atom differential light shift created by the running-wave and the standing-wave trap. Figure 5.5(c) shows how the

two-photon Raman resonance frequency depends on the trap detuning for the Rydberg state $54S$. To make the resonance shift measurements in the two different traps comparable, the beam power is adjusted to have similar maximum light intensities at the atoms. Nevertheless, we observe a different Δ-dependency of the two-photon Raman resonance for the two trap configurations. The difference can possibly be attributed to an incorrect consideration of the losses in the retro-reflection beam path. For both trap configurations, the two-photon Raman resonance coincides with the un-trapped atom resonance for the same trap detuning Δ. Investigation of the effects of differential light shifts on collective Rydberg excitations require the consideration of differential light shift influencing effectively many atoms across the atomic ensemble.

5.2.2 Estimation of the Differential Light Shift across the Atomic Cloud

For the determination of the magic detunings for collective Rydberg excitations, it is necessary to take into account the spatial distribution of the atoms in the potential landscape given by the trapping beam shape. As already discussed, it is only possible to cancel differential light shifts independently of position in the running wave and in the periodic potential case. For both, we derived analytical expressions for the magic detunings (Eqs. 5.3 and 5.4). In this section, we turn our attention to the case of the full standing wave by considering the combined nonperiodic and periodic potential contributions. Therefore, we consider the trapping beam shapes and the spatial atom distribution, and discuss two methods to estimate the differential light shift across the atomic ensemble.

A standing-wave trap at detuning $\Delta_n^{\sim}$, where there is no differential light shift from the periodic potential contribution, gives rise to a differential light shift arising purely from the nonperiodic potential $U_q^-(\boldsymbol{r}, \Delta)$. This residual differential light shift $U_{\text{residual}}^-(\boldsymbol{r}, \Delta)$ is given by

$$U_{\text{residual}}^-(\boldsymbol{r}, \Delta_n^{\sim}) = U_n^-(\boldsymbol{r}, \Delta_n^{\sim}) - U_g^-(\boldsymbol{r}) = -\frac{\alpha_f}{4}(1-\theta_n)\left[E_{\rightarrow}^2(\boldsymbol{r}) + E_{\leftarrow}^2(\boldsymbol{r})\right].$$

For Rydberg states with low principal quantum number ($n < 25$), this differential light shift contribution vanishes because $\theta_n \simeq 1$. In the case of high principal quantum numbers with θ_n significantly smaller than one, the residual potential only vanishes in the trivial case of no trapping laser ($E_{\rightarrow(\leftarrow)}(\boldsymbol{r}) = 0$). The residual differential light shift from the nonperiodic potential $U_{\text{residual}}^-(\boldsymbol{r}, \Delta)$ can be reduced, if the addressed atoms only sample the center part in the trapping beam Gaussian envelopes $E_{\rightarrow(\leftarrow)}(\boldsymbol{r})$ given in Eq. 3.20. Thereby, the total differential light shift becomes independent of the position, and the common light shift for all atoms across the ensemble does not influence the collective state coherence.

For our experimental setup, not all the positions within the Gaussian envelope of the trapping beam $E_{\rightarrow(\leftarrow)}(\boldsymbol{r})$ have to be considered for the residual differential light shift calculation. In the following, we separately discuss the case for the axial and the radial direction. In the axial direction, $E_{\rightarrow(\leftarrow)}(\boldsymbol{r})$ has to be compared to the size of the atomic cloud. Figure 5.6(a) and 5.6(b) show the small variation of the trapping beam radius $w_t(x)$ over the length scale of the atomic cloud. The atom cloud distribution is given by the shape of the crossed trap shown in Fig. 4.5. The Rayleigh length of the trapping beam $X_R = 1365\,\mu\text{m}$ is much larger than half the cloud length $40.8\,\mu\text{m}$. Therefore, the intensity variation in the axial direction is negligible for the calculation of differential light shifts.

In the radial direction, the atoms that contribute to the collective excitation are only those that are addressed with the two-photon excitation lasers. The probe beam with its smaller waist determines the relevant radial length scale. Figure 5.6(c) shows the normalized intensity of the trap and the probe beam in their focal plane. The square of the electric field amplitude $E_{\rightarrow(\leftarrow)}^2(\boldsymbol{r})$ drops in the radial

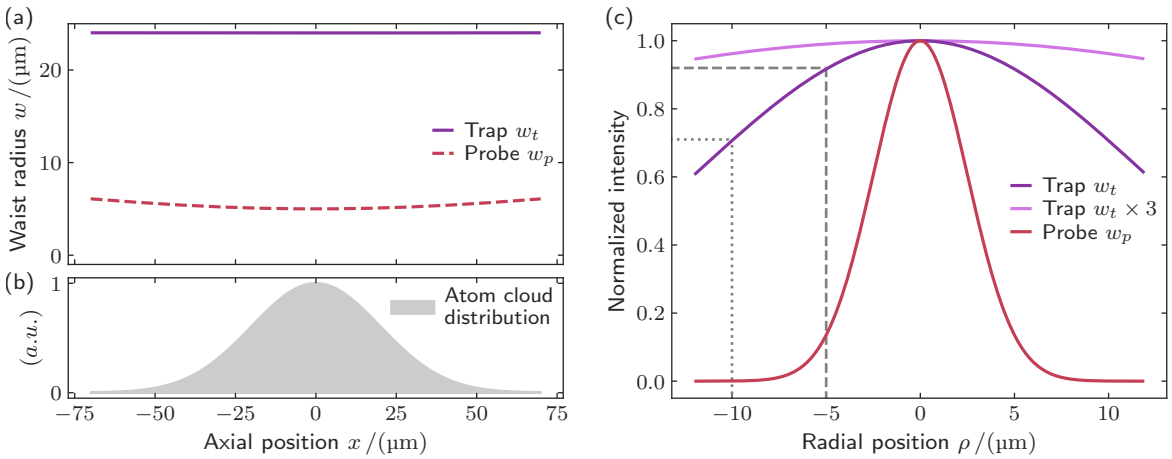

Figure 5.6: (a) Beam waist radius of probe (red, dashed) and trap (purple, solid) laser, with their respective $1/e^2$ waist radii of $w_{p,0} = 5\,\mu\text{m}$ and $w_{t,0} = 24\,\mu\text{m}$. (b) The axial extent of the atomic cloud with length $L = 81.6\,\mu\text{m}$. (c) Normalized radial intensity distribution for the probe beam (red), and the trapping beam (purple). The latter is shown for waist radii $w_{t,0}$ and three times $w_{t,0}$. The intensity is calculated from Eq. 3.20 in the focal plane. The dashed lines mark the position at $\rho = -w_{p,0}$ and the dotted lines mark the position at $\rho = -2 \cdot w_{p,0}$, as well as the respective normalized intensity for the trap beam waist $w_{t,0}$ in the experiment.

direction to 92 % at the probe radius $w_{p,0}$. This probe radius covers 95 % of the atoms in one direction. At a radius of $2w_{p,0}$, the intensity drops to 71 %, while including with 99.7 % a larger fraction of the atoms. This intensity variation can be reduced by choosing e.g. choosing a larger trap beam waist, as indicated in Fig. 5.6(c). However, a larger trap beam waist results in a reduced atomic density, when assuming that the same amount of atoms is loaded initially. Therefore, a trade-off depending on the requirements for specific experiments has to be made. For the trap beam waists in our experiment, we are limited by spatial constraints in the optical setup.

In order to understand the effects of differential light shifts, we now introduce two methods to estimate the differential light shifts created by trapping beams of any shape.

First, one can estimate the differential light shift across the atomic cloud by calculating the standard deviation over all spatial positions, as done in Ref. [1]. Based on the given experimental geometry, only a subset of atoms should be included into the calculation. For our experimental setup, only atoms within the radial waist of the probe beam are contributing to the collective excitations, and, hence, to the variation of the differential light shift. Inside this excitation volume, we consider furthermore only positions where $U_g(\rho, x) \leq U_g(0,0) + 2 \cdot k_B T$. This condition is motivated by the fact that the mean kinetic energy of the atoms, here approximated by $k_B T$, limits the volume where the atoms are moving. Figure 5.7(a) shows the standard deviation of the differential light shift $\delta U_{\text{std}}(\boldsymbol{r}, \Delta)$ in Eq. 5.2 with the discussed considerations. The vertical dashed lines mark the positions of the analytically determined magic conditions in Eq. 5.3 and 5.4. The standard deviation of the differential light shift in the running wave and periodic potential vanishes at these trap detunings. The standing wave optimal detuning lies in between the dashed lines at Δ_{76}^{sw}. Note that the standard deviation for our experimental parameters is not zero.

In the second method, we extend the analysis discussed in the previous paragraph by assigning a weight to each differential light shift contribution before calculating the standard deviation, which

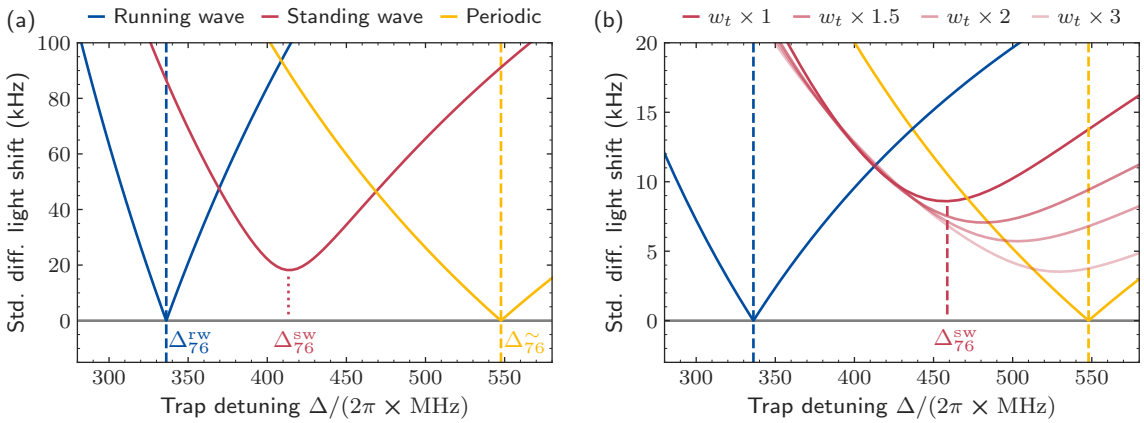

Figure 5.7: (a) Calculated standard deviation of the differential light shift between ground state and Rydberg state 76S. For the parameters of our experiment, only differential light shifts inside the indicated volumes in Fig. 5.4 are taken into account. The two detunings calculated from the analytical magic conditions in Eq. (5.3) and Eq. (5.4) are shown as vertical dashed lines. The optimal detunings for the running wave (blue), the standing wave (red), and the periodic potential (yellow) are where the respective standard deviation is minimized. These are denoted by $\Delta_{76}^{\mathrm{rw}}$ for the running wave, $\Delta_{76}^{\sim}$ for the periodic potential, and $\Delta_{76}^{\mathrm{sw}}$ for the full standing wave. (b) Standard deviation calculated with weighted contribution for each position as described in the main text. The red solid lines are calculated for different trap beam waists. The red dashed line marks the optimal detuning for the trap beam waist implemented in the experiment. Figure (a) adapted from Ref. [1] and (b) adapted from Ref. [114].

follows the idea of Ref. [163]. Each position is weighted by the probe beam amplitude and a Boltzmann distribution with a given temperature T [114]. Therefore, we write the weighted differential light shift as

$$\delta U_{\mathrm{weighted}}(\boldsymbol{r},\Delta) = p(\boldsymbol{r},w_{p,0}) \cdot n(\boldsymbol{r},T) \cdot \left[U_n(\boldsymbol{r},\Delta) - U_g(\boldsymbol{r})\right],$$

where $p(\boldsymbol{r},w_{p,0})$ is a weighing factor defined by the probe beam shape and $n(\boldsymbol{r},T)$ is the atomic density distribution of ground-state atoms. The weighing factor $p(\boldsymbol{r},w_{p,0})$ is a normalized Gaussian beam as in Eq. 3.20. By the second factor, we approximate the thermal distribution of the ground-state atoms in the respective potential landscape. The weights for each position in the ground state potential landscape are given by a Boltzmann distribution as [164]

$$n(\boldsymbol{r},T) = \frac{\exp\left(-U_g(\boldsymbol{r})/(k_B T)\right)}{\int d\boldsymbol{r}^3 \exp\left(-U_g(\boldsymbol{r})/(k_B T)\right)}.$$

The standard deviation over this weighed differential light shift is shown in Fig. 5.7(b) for the different trap configurations. As for the calculation with simpler approximations in Fig. 5.7(a), the standard deviation of the running wave and the periodic potential are minimized at the analytic magic conditions. Comparison of Fig. 5.7(a) and 5.7(b) shows that detuning where the standard deviation is minimized shifts towards the periodic potential, when the positions are weighed. In the rest of this thesis, the detuning Δ_n^{sw} refers to trap detuning with the lowest standard deviation calculated by the weighed differential light shift contributions.

Figure 5.7(b) shows the standard deviation of the differential light shift for different trapping beam waists. As the trapping beam waist is increased, the optimal detuning in the standing-wave trap $\Delta_{76}^{\mathrm{sw}}$ shifts towards the magic detuning in the periodic potential $\Delta_{76}^{\sim}$. This is caused by a more homogeneous trap intensity across the probe beam, as presented in Fig. 5.6(b). The increased trap beam waist reduces the contribution of the nonperiodic potential to the total differential light shift.

5.2.3 Determination of Magic Detunings by Photon Storage Experiments

As shown in Fig. 5.7(b), the exact shape of the trap determines the magic detunings. In order to analyze our theoretical calculation, the trap-induced decoherence of the collective Rydberg excitations introduced in Section 2.1.1 is measured. For this investigation, the photon storage and retrieval experiments described in Section 4.3.2 are used. The differential light shifts in the running- and standing-wave trap cause a dephasing in the retrieval efficiency $\eta(t_s)$ as discussed in Section 2.1.1.

The magic detuning can be determined as the trap detuning, that allows the longest coherence times in the photon storage and retrieval experiments.

Figure 5.8(a) and (b) show the photon retrieval efficiency for two different trap detunings, where we normalized the efficiency to the value for the shortest storage time of 0.5 µs. The decays are not just simple exponential or Gaussian decay curves, but have features of additional oscillations, which will be discussed in Section 5.3. Here, we focus on an overall damping of the retrieval efficiency and use a simple exponential fit with the function

$$f(t_s) = A \cdot e^{-t_s/t_c}$$

to extract a coherence time t_c as single parameter.

In Fig. 5.8(c), the measured coherence time t_c is presented as function of trap detuning Δ for the Rydberg state $76S$. For the running wave, the coherence times are longest at the calculated magic detuning $\Delta_{76}^{\mathrm{rw}}$. The measurements in the standing-wave trap do not show the longest coherence times around the calculated magic detuning for a periodic potential $\Delta_{76}^{\sim}$. Instead, it matches better with the detunings having the lowest standard deviation of differential light shift calculated for our experimental parameters.

In the photon storage and retrieval experiments, it is only possible to identify an optimal detuning with minimized differential light shift dephasing, if all other dephasing mechanisms are comparably small. The only relevant detuning dependent dephasing mechanism is the decay of the Rydberg state due to the near-resonant coupling with the state $6P_{3/2}$. For our parameters, the coherence times are not limited by the lifetime of the Rydberg state as indicated in Fig. 5.8(c). Furthermore, the coherence time can be limited due to high atomic densities, as will be discussed later in detail in Section 5.3.

Figure 5.9(a) shows the coherence times measured for different number of atoms confined in a standing-wave trap. These measurements are performed with Rydberg state $89S$. The three datasets are labeled with an optical density measured in the crossed dipole trap, before transferring the atoms into the magic trap. By independently measuring atom number and temperature from absorption images, we estimate a peak atomic density in the standing wave potential. The atomic densities for the three presented datasets are $4.0(7) \times 10^{12}\,\mathrm{cm}^{-3}$, $7(1) \times 10^{12}\,\mathrm{cm}^{-3}$, and $17(1) \times 10^{12}\,\mathrm{cm}^{-3}$, respectively. At high atomic densities, the optimal detuning washes out and is harder to determine. Therefore, we generally adjust the number of loaded atoms such that the density caused dephasing does not limit the determination of the optimal detuning.

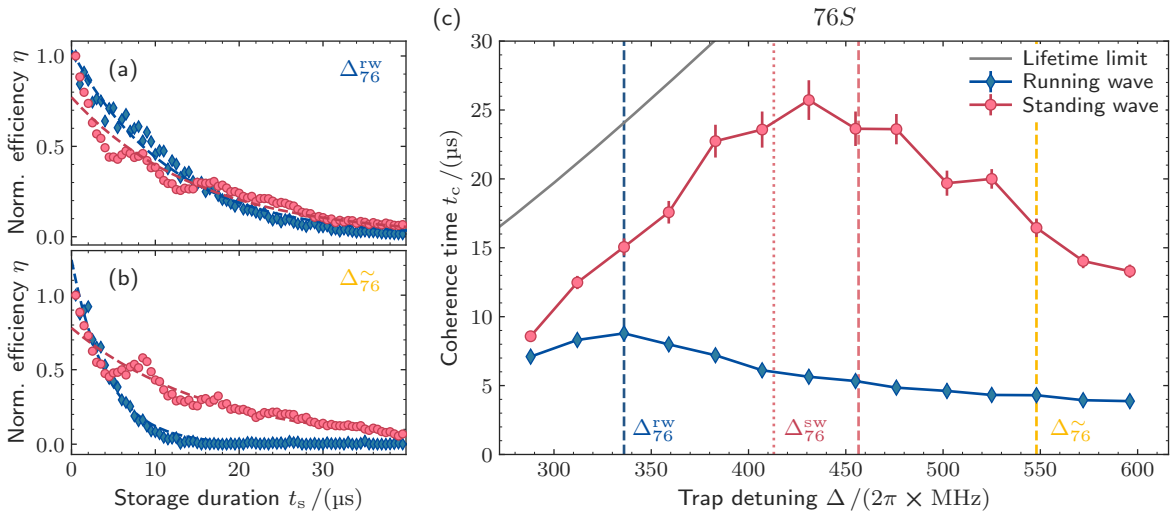

Figure 5.8: (a), (b) Normalized photon retrieval efficiency as function of storage time t_s. The atomic cloud is confined in the running-wave (blue) and a standing-wave (red) trap. The trap is set to the optimal detunings derived from the analysis shown in Fig. 5.7 for (a) the running wave case with $\Delta = \Delta_{76}^{rw}$ and (b) the standing wave case with $\Delta = \Delta_{76}^{\sim}$. The dashed lines show exponential fits to extract respective coherence times τ_c. (c) The coherence times τ_c measured in the running-wave and standing-wave trap as function of the trap laser detuning Δ. The vertical dotted and dashed lines show the optimal detunings from the analysis in Fig. 5.7. The gray curve shows the Rydberg state lifetime, that includes the effective lifetime due to blackbody radiation and the near-resonant coupling to the $6P_{3/2}$ state. Figure adapted from Ref. [1].

In contrast to the spectroscopy measurements in Section 5.2.1, the photon storage and retrieval experiments show a clear difference between the running-wave and the standing-wave trap. The two trap configurations differ experimentally by the amount of power in the retro-reflection beam.

Figure 5.9(b) shows the coherence time for different power balances in the optical trap for Rydberg state $54S$. The power of the retro-reflection is adjusted to change from a running wave (where $E_{\leftarrow}/E_{\rightarrow} = 0$) to our standing wave (where $E_{\leftarrow}/E_{\rightarrow} = 0.87$). For a very small amount of retro-reflected light, the coherence time improves, not only around the running wave case, but also around the standing wave optimal detuning. In such an imbalanced standing wave, only the very cold atoms are trapped in the periodic contribution of the standing-wave trap. Their contribution to the retrieval efficiency gives rise to the prolonged coherence times around Δ_{54}^{sw}. In contrast, the hotter atoms are not confined in the periodic contribution and experience a running-wave trap with a different optimal detuning. We can resolve a difference in optimal detuning between the running-wave and the standing-wave trap for the measurement with Rydberg state $76S$ (Fig. 5.8(c)) and with Rydberg state $54S$ (Fig. 5.9(b)). From these measurements, we conclude that we can find magic detunings over a large range of principal quantum numbers.

The two magic conditions in Eq. 5.3 and Eq. 5.4 both scale with the reduced dipole matrix element $D_{an} \propto (n^*)^{-3/2}$. For Rydberg states with higher principal quantum number n, we expect the optimal detunings Δ_n^{trap} to be closer to the $6P_{3/2}$ state. This is also visible in Fig. 5.8(c), Fig. 5.9(a) and Fig. 5.9(b).

Figure 5.10(a) shows the theoretically expected and experimentally determined optimal detuning as function of n for the different trap configurations. The scaling of the optimal detunings with the

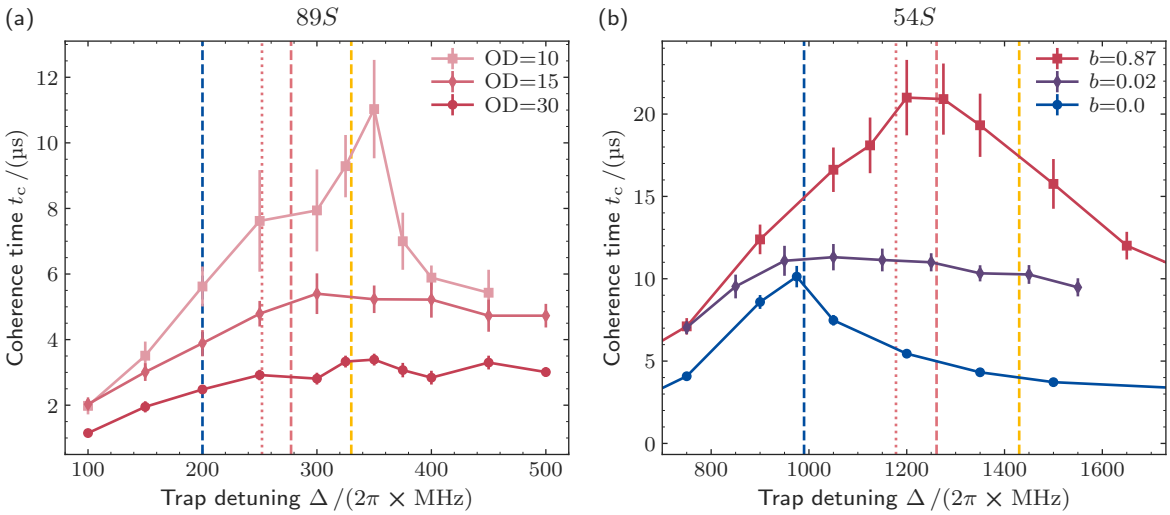

Figure 5.9: (a) Coherence time t_c as function of trap detuning Δ for three different atomic densities. The atomic density is given as optical depth (OD), see the main text for an estimation of peak atomic density. The measurements are performed with atoms confined in the standing-wave trap and excited to Rydberg state $89S$. (b) Coherence time t_c for Rydberg state $54S$ as function of trap detuning Δ for different ratios $b = E_{\leftarrow}/E_{\rightarrow}$ of incoming and retro-reflected trap beam electric field. The vertical dotted and dashed lines mark the optimal detunings found by the lowest differential light shift standard deviation for the respective trap configuration, see Fig. 5.7. Note the two different x-axis scales in (a) and (b).

principal quantum number is given by the reduced dipole matrix elements D_{an}. For the standing-wave trap in Ref. [60], this scaling of the reduced dipole matrix elements with principal quantum number has been observed. The measured optimal detunings show the same trend as the magic detunings for the running-wave trap (Eq. 5.3) and the periodic potential (Eq. 5.4), where the difference between the two detuning conditions is given by the landscape factor θ_n.

To emphasize the difference between the running-wave and standing-wave trap, an effective polarizability α_n^{trap} is calculated as

$$\alpha_n^{\text{trap}} := \frac{D_{an}^2}{4\hbar\Delta_n^{\text{trap}}}. \tag{5.5}$$

The effective polarizability removes the $(n^*)^{-3/2}$ scaling of the dipole matrix elements. Figure 5.10(b) shows the effective polarizability α_n^{trap} as function of principal quantum number n. The difference in effective polarizability between the running-wave and the standing-wave trap is directly visible for higher ($n > 30$) principal quantum numbers. To quantify this difference, the analytically determined magic conditions for the running wave and periodic potential can be reformulated with α_n^{trap} (Eq. 5.5) to

$$\alpha_n^{\text{rw}} = \alpha_g - \alpha_f \tag{5.6}$$

$$\alpha_n^{\sim} = \alpha_g - \alpha_f \cdot \theta_n, \tag{5.7}$$

where the difference follows the landscape factor θ_n in Eq. 3.30.

One can understand the difference by considering the size of the Rydberg atom with respect to the standing wave periodicity. In order to compare the two, the top axis in Fig. 5.10(b) shows the

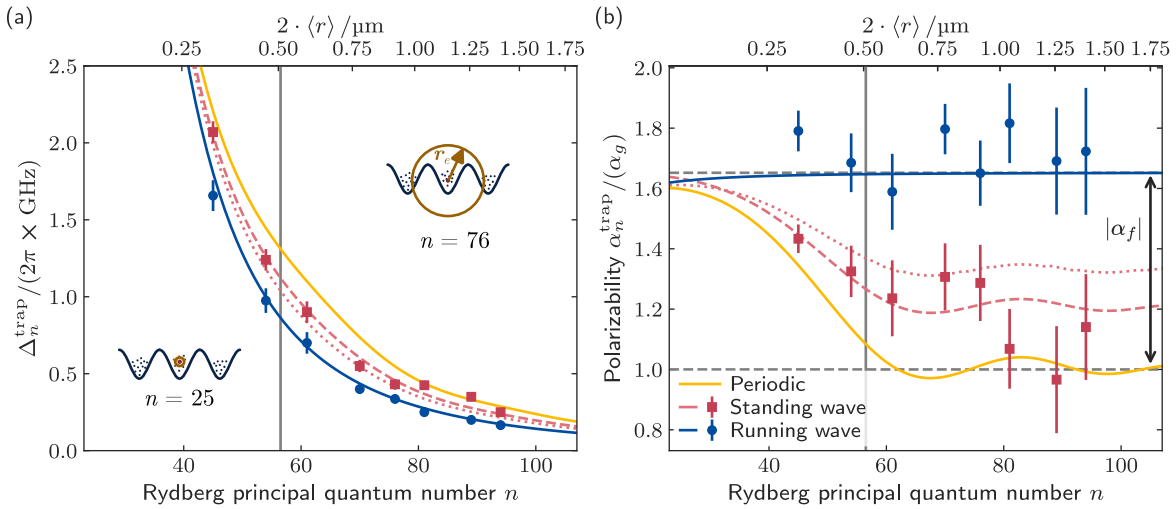

Figure 5.10: Scaling of the magic detunings in the different traps as function of principal quantum number n. (a) Optimal detunings Δ_n^{trap} in the running-wave (blue, circles) and standing-wave trap (red, squares) for different Rydberg states. The solid curves show the magic detunings for the running-wave (blue, Eq. 5.3) and periodic potential (yellow, Eq. 5.4). The red dashed line is the optimal detuning with the lowest standard deviation across the atomic cloud as shown in Fig. 5.7(a). The top axis shows the Rydberg electron orbital diameter $2 \cdot \langle r \rangle$ in Eq. 2.11 for the respective principal quantum number. The standing-wave trap periodicity of 506 nm is marked by the gray vertical line. The two schematic figures show the electron radius r_e for $n = 25$ and $n = 76$ in comparison to the standing wave. (b) Effective polarizability from Eq. 5.5 for the measured and calculated data in (a) as a function of principal quantum number. Figure adapted from Ref. [1].

Rydberg electron orbital diameter $2 \cdot \langle r \rangle$, and the solid vertical line marks the ~ 506 nm lattice spacing. For smaller Rydberg state with $n < 30$, the electron explores only a fraction of the standing wave as sketched in Fig. 5.10(a) for $n = 25$. However, for Rydberg states with $n > 30$, the two effective polarizabilities become significantly different.

In Fig. 5.10(b), the standing-wave periodicity can be seen as a ruler for the size of the Rydberg electron wave function. Our measurements highlight that the exact trapping potential modifies the effective polarizability for Rydberg states with high principal quantum number.

5.3 Challenges for Photon Storage Experiments with Atoms in the Standing-Wave Trap

The dynamics of the retrieval efficiency as function of the storage duration, given by $\eta(t_s)$ in Eq. 2.6, depend on the time evolution of the collective state $|\psi(t_s)\rangle$. In the standing-wave trap, the retrieval efficiency shows different dynamics compared to the Gaussian-shaped decay envelope given by the thermal motion of the atoms, as visible in Fig. 5.8(a) and 5.8(b).

In this section, we discuss two effects that add additional oscillations. For the experiments presented here, the trap detuning is set to the experimentally determined magic value as described in the previous section.

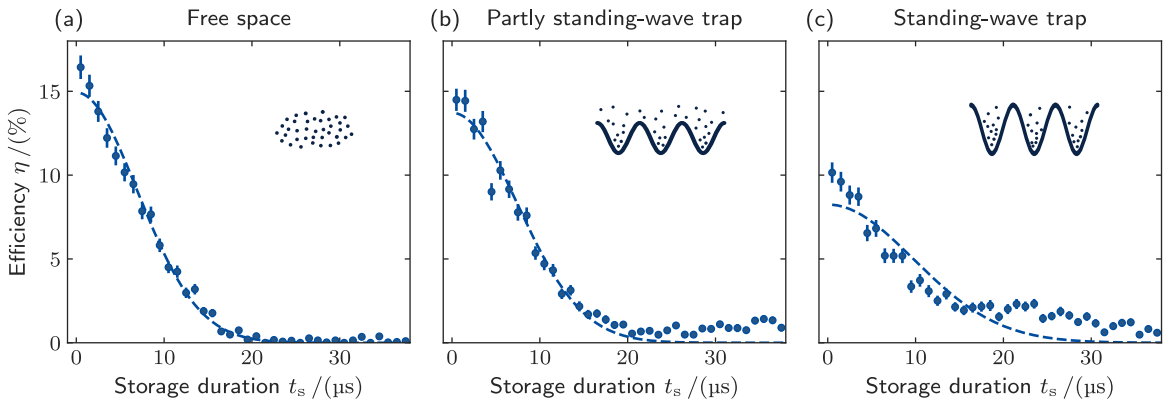

Figure 5.11: Photon retrieval efficiency for atoms in (a) free space, (b) partly confined in the standing-wave trap and (c) fully confined in the standing-wave trap. For the free space experiment, the crossed trap is pulsed as already shown in Fig. 4.9(b), while the standing-wave trap is set to zero intensity. The data presented in (b) and (c) are measured by increasing the intensity of the standing-wave trap while decreasing the intensity in the crossed trap. The inserts are schematics of the fraction of atoms in free space compared to confined in the standing wave. The dashed line is a Gaussian decay model fitted to the respective data, which are measured for Rydberg state 61S.

5.3.1 Atom Oscillations in Lattice Wells

The first effect that we discuss is the periodic motion of the ground-state atoms in the standing-wave trap. The ground-state atoms in the experiment have a finite temperature, $T = 2\,\mu\text{K}$. The trap depth in typical experiments is $13\,\mu\text{K}\,k_\text{B}$. This results in an axial trap frequency (Eq. 3.28) of $\nu_\text{ax} = 52\,\text{kHz}$. The resulting atomic oscillation period is 19 μs, which is on the timescale of the storage durations in our typical experiments. The exact oscillation period depends on the trap depth (Eq. 3.28), and the oscillation is expected to modify the dynamics.

Figure 5.11 shows the emergence of the modified temporal dynamics in the photon retrieval efficiency, when increasing the standing-wave trap intensity. For a one-dimensional trap with only a small periodic part, as indicated by the schematic in Fig. 5.11(b), the initial decay is still well described by the Gaussian envelope. However, a non-vanishing retrieval efficiency for storage durations longer than 20 μs emerges, that is attributed to a small fraction of very cold atoms confined in the standing-wave potential wells. The decay of retrieval efficiency with storage duration is not well described by the Gaussian-shaped envelope expected for a thermal atom cloud with the highest possible intensity in the retro-reflected beam, as sketched in Fig. 5.11(c). The temporal dynamics are given by motional rephasing of the atom cloud, which has been observed for photon storage and retrieval experiments with collective states involving atomic ground states [43, 70] as well as Rydberg states [60].

Next, we investigate the oscillation behavior of the retrieval efficiency depending on the trap depth and, hence, the trap frequency. Figure 5.12(a) shows the two photon storage and retrieval experiments for different depths of the standing-wave trap. The decays show oscillations with tens of microsecond periods, as well as a faster one on the microsecond timescale. To extract both oscillation periods, we

first fit a model as

$$\eta(t_s) = \exp(-t_s/\tau) \cdot [A + B \cdot \sin(2\pi\nu_{\mathrm{ax}} t_s + \phi_{\mathrm{ax}}) + C \cdot \exp(-t_s/\tau_{\mathrm{dimer}}) \cdot \sin(2\pi\Delta_{\mathrm{dimer}} t_s + \phi_{\mathrm{dimer}})], \tag{5.8}$$

where τ is an overall decay constant, ν_{ax} and ϕ_{ax} are the axial trapping frequency and an initial phase. The last term arises from additional excited states that lead to the fast oscillations in Fig. 5.12(a) visible for the deeper trap depth. Their origin will be discussed in the next section. To make the slower oscillation visible, an exponential fit is subtracted from the data and the residuals are shown as the open markers. The frequency components from the residual data are extracted with a Fourier transform and presented for the different trap depths in Fig. 5.12(b). The slow oscillation component ($f_{\mathrm{Fourier}} < 100\,\mathrm{kHz}$) increases in frequency with trap depth and is associated with the periodic atomic motion in the standing-wave potential wells. The secondary peak at around 500 kHz corresponds to the fast oscillations.

The axial trap frequency of the standing-wave trapping potential ν_{ax} can be determined independently by parametric heating [157, 165]. For that purpose, we modulate the standing-wave trap intensity with a given modulation frequency f_{mod}.

Figure 5.12(c) shows how the probe beam transmission through the atomic cloud changes as function of modulation frequency. The transmission is a measure for the atom number inside the standing-wave trap. When the standing-wave well depth is modulated at twice the trap frequency ν_{ax}, the atoms are heated whereby some atoms escape from the trap and hence reduce the probe beam absorption. In order to measure the harmonic part of the standing-wave potential, the standing-wave trap is during the atom cloud preparation lowered such that most of the hot atoms can escape and only the coldest atoms remain. The intensity modulation is applied for 10 ms to an atomic ensemble with a temperature of approximately $T = 1\,\mu\mathrm{K}$, which is small compared to typical trap depths in our experiments.

To compare the different methods for measuring trap frequencies described above, the obtained trap frequencies as function of standing-wave trap depth U_0 are shown in Fig. 5.12(d). The figure gives the trap frequency extracted from fits like the ones in Fig. 5.12(a), from Fourier spectra like in 5.12(b) and from parametric heating as shown in panel 5.12(c). The trap frequencies extracted from the photon storage and retrieval match well with the theoretical trap frequency, that is calculated with Eq. 3.28. The parametric heating method likely underestimates the trap frequencies, as the addressing of the highest trap frequencies does not necessarily heat the atoms enough to cause significant atom loss. Instead, lower trap frequencies address hotter atoms, that are then more likely to leave the trapping potential.

In essence, the periodic motion of the atoms in the standing-wave potential wells strongly modifies the temporal dynamics in the storage and retrieval process. In Ref. [70], the atoms are considered to perform a classical motion in the standing-wave potential. This model does not apply when the two states involved experience different trapping potentials. The different trap potential for atoms in the ground and Rydberg states has been considered in Ref. [60], where the retrieval efficiency is modeled by quantizing the motion of the ground and the Rydberg atoms inside the optical standing-wave trap.

5.3.2 Formation of Rydberg Molecules in Dense Atom Clouds

In addition to the thermal rephasing described in the previous section, the photon storage and retrieval is modified by the increased local density inside the standing-wave trap wells. The large density results

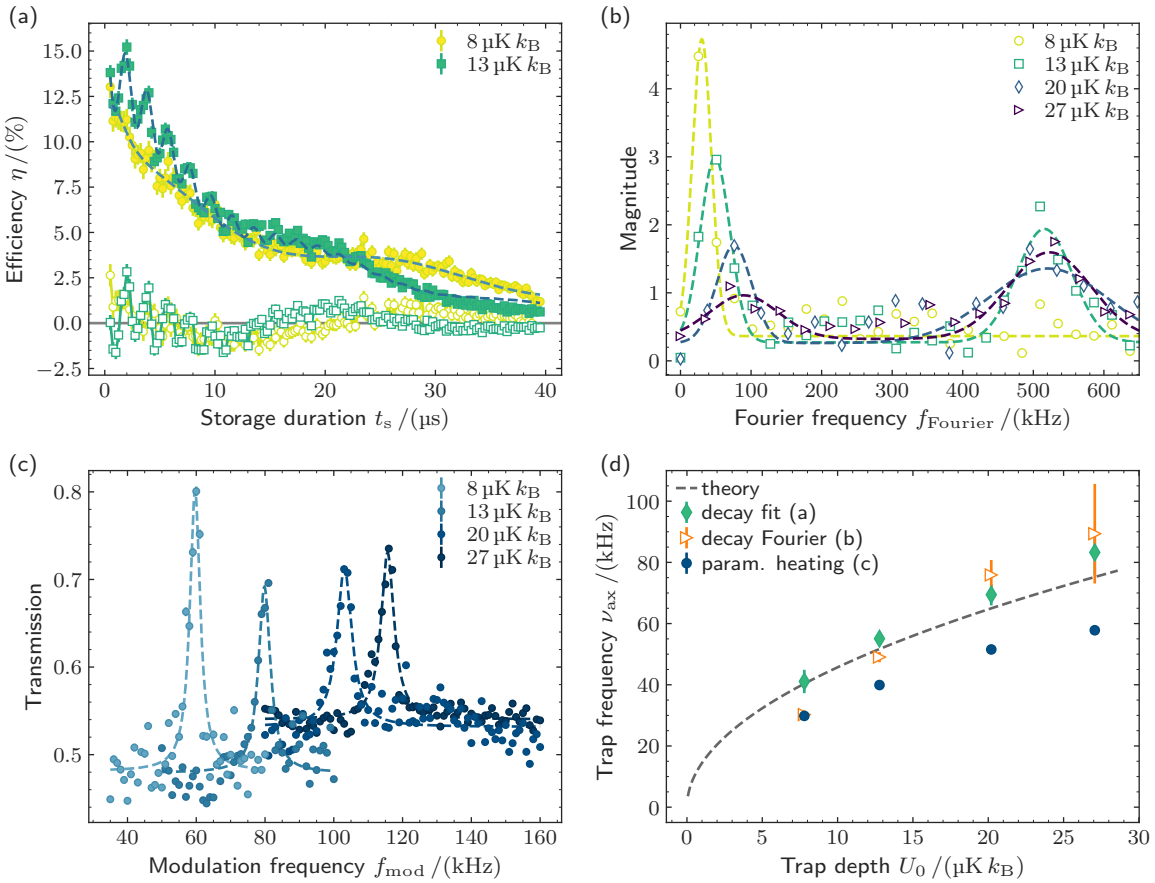

Figure 5.12: (a) Photon storage and retrieval experiment at 61S for two different standing-wave trap depth U_0. The filled markers are the retrieval efficiency to which a function (dashed) with the slow lattice oscillations and secondary faster oscillations is fitted. The open markers are the same data with an exponential fit subtracted, see main text for details. (b) Fourier spectrum of the open marker data in (a) for different trap depths. The center positions of two different Fourier components are extracted by Gaussian fits (dashed lines). (c) Probe beam transmission through the atomic cloud as function of the modulation frequency f_{mod} of the standing-wave trap depth U_0. The dashed lines show Lorentzian functions to determine the center frequency. (d) Axial trap frequency ν_{ax} in the standing-wave trap as function of the trap depth U_0. The trap frequency from the photon storage experiments is extracted from the fits in (a) (green diamonds) and from the center Fourier frequency in (b) (orange open triangles). The trap frequency from parametric heating in (c) is determined for two different atom temperatures (blue circles and red squares), see main text for details. The black solid curve shows the expected trap frequency.

in the formation of ultralong-range Rydberg molecules [166, 167]. These molecules are created when one or more ground-state atom form bound states with a Rydberg atom, where the bound states arise from a scattering-induced interaction between the ground-state atoms and the Rydberg electron. The ultralong-range Rydberg molecules form in very dense media, where the mean distance between atoms is comparable to the Rydberg electron radius.

In this section, we discuss how these Rydberg molecules influence the dynamics of the photon retrieval efficiency.

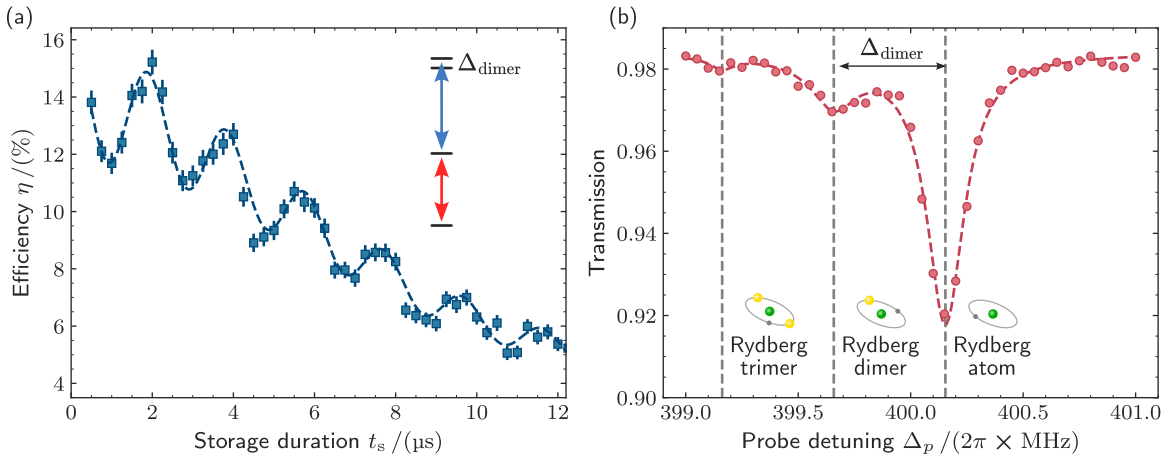

Figure 5.13: (a) Photon retrieval efficiency measured for Rydberg state $61S$ in a dense atomic cloud. The data is the same as the first 12 µs in Fig. 5.12(a). The dashed line shows a fit (Eq. 5.8) to extract the dimer frequency Δ_{dimer}. The dimer frequency is the difference in binding energy between the Rydberg atom and Rydberg dimer, as shown in the schematic. (b) Two-photon Raman transition, with excitation resonances of Rydberg atoms, dimers and trimers. The resonance centers are extracted by a triple Lorentzian fit (dashed line).

Figure 5.13(a) shows the fast oscillation visible in the first 12 µs of the photon storage and retrieval experiments in Fig. 5.12(a). The oscillation arises from the interference between these two excitation paths ways, where the Rydberg dimer is an additional state detuned by Δ_{dimer} from the two-photon resonance [168].

The two-photon transition with two excited states is sketched in Fig. 5.13(a). It should be noted, that the oscillation in the efficiency originates from the same kind of excitation path interference as presented for multiple populated ground states in Fig. 4.14. With the fit of Eq. 5.8, the frequency of the fast oscillation is extract as $\Delta_{dimer} = 514(3)$ kHz. This is similar to the value measured in Ref. [168]. The dimer frequency Δ_{dimer} determines the Rydberg dimer binding energy, given by $-h\Delta_{dimer}$, where the scaling with the principal quantum number is approximately given as $\Delta_{dimer} \propto (n^*)^{-6.3}$ [168, 169]. The ultralong-range molecules can be detected in probe beam transmission measurements independently of the photon storage and retrieval experiments.

Figure 5.13(b) shows the transmission spectrum for Rydberg state $61S$, where the excitation resonances for the Rydberg atom and Rydberg dimer are separated by Δ_{dimer}. The secondary red-shifted resonance at $2 \times \Delta_{dimer}$ is related to the formation of trimer states [170], where the Rydberg electron interacts with two ground-state atoms. A fit of three Lorentzian line shapes to the data gives a dimer frequency of $\Delta_{dimer} = 496(12)$ kHz, that is close to the value extracted from the photon storage and retrieval measurement.

Despite the motional rephasing and ultralong-range Rydberg molecule formation, the standing-wave trap enables the storage of single photons in collective Rydberg excitations for tens of microseconds.

CHAPTER 6

Conclusion and Outlook

In this thesis, I presented a theoretical and experimental study on magic trapping conditions for atoms involved in collective ground-state–Rydberg-state excitations, which are used for photon storage in an ensemble of ultracold atoms. The main focus of my work was to investigate how the geometry of the optical trap influences the ensemble dephasing rate and how the wavelength corresponding to the magic trapping condition is determined by the trap configuration.

Before discussing the magic trap, I introduced the theoretical concepts used throughout the thesis and described the experimental apparatus [61, 129, 152, 171]. A significant part of the work involved reconstructing the experimental apparatus following its relocation from the University of Southern Denmark to the University of Bonn in May 2021.

This thesis documents key aspects of the setup characterization and outlines selected steps in the preparation of an ultracold ensemble of rubidium-87 atoms. The preparation sequence includes trapping of ultracold rubidium atoms in various optical trap geometries and aligning the atomic cloud with the focus of the probe beam. As the final step in the atom cloud preparation, the atoms were optically pumped into a single magnetic substate. Successful state preparation, with 99.5 % of the atoms in the desired substate, was independently confirmed through transmission measurements and photon storage and retrieval experiments.

In addition to reconstructing the experimental setup, I implemented a new one-dimensional optical trap that can be operated in two configurations, either as a running-wave trap or as a standing-wave trap. The standing-wave configuration is particularly valuable, as it enables spatial confinement of atomic motion along the axis of the trap, which is relevant for suppressing motional dephasing in collective Rydberg excitations.

The trap is formed using a laser with a wavelength of 1012 nm. This wavelength is chosen because it forms a far-off-resonant dipole trap for the rubidium ground state. The laser can be tuned close to resonance with the transition between the $6P_{3/2}$ state and a Rydberg state. This allows the creation of a near-resonant dipole trapping potential for that Rydberg state, while the ground state potential remains essentially unchanged.

By varying the detuning from the transition to the $6P_{3/2}$ state, the optical potential experienced by the Rydberg state can be strongly modified. To identify the magic trapping condition for the ground and Rydberg states—that is, when both optical potentials are equal—I calculated them as a function of laser detuning.

I used photon storage and retrieval experiments to measure the magic wavelength for a range of

principal quantum numbers ($45 \leq n \leq 94$). The experimentally determined values were in agreement with the calculated ones. We were able to experimentally observe distinct magic wavelength for the two trap geometries [1]. The difference in magic wavelengths between the running-wave and standing-wave traps is attributed to the repulsive force on the Rydberg atoms, which arise from the ponderomotive potential acting on the almost-free Rydberg electron within the given potential landscape [57, 58].

Using the standing-wave configuration, we observed 20 µs ground-to-Rydberg coherence time, similar to what has been reported by others [60]. This confirms that the standing-wave trap effectively restricts atomic motion, thereby reducing motional decoherence and highlighting the advantage of magic trapping.

The demonstration of the dependence of the magic wavelength on the trap geometry that I presented in this thesis shows that trapping of Rydberg atoms is not straightforward. One has to take the Rydberg electron wave function into account, when designing optical traps that are on the same size-scale as the wave function. The investigation of how to create magic traps for ground and Rydberg states can be applied to a range of different trapping beam shapes. The results in this thesis can help to find better ways of confining atoms, that are used as a platform for strong coupling of single-photons with atomic ensembles.

Outlook

The implementation of a new optical trap in the experimental setup presented in this thesis is directly applicable to future experiments aimed at spatially resolving photon–photon interactions mediated by Rydberg–Rydberg interactions, using an EMCCD camera [171].

While the work presented in this thesis indicates that it is possible to limit the motional dephasing of collective Rydberg excitations with the magic standing-wave trap, there are other effects that limit the coherence time. For example, high and spatially varying atomic densities as shown in Fig. 5.9(a). In a standing wave trap, the atomic density varies rapidly over short distances, leading to an additional limitation on the coherence time which is independent of whether the trap is magic or not.

This problem can generally be solved by reducing the atomic density in the trap [37]. However, a lower number of atoms contributing to the collective excitation also results in a reduced coupling of the atomic ensemble to single photons. As a result, the new one-dimensional trap may not be directly applicable for systems with a single or few Rydberg superatoms that require strong light-matter coupling. It is however possible to imagine a waveguide-like system with a higher number (on the order 10) dilute superatoms along the standing-wave trap, and, thereby, avoid the coherence time limitation by high densities.

An alternative approach would be to replace the existing dimple trap laser at 805 nm with a laser operating at 1012 nm. This substitution would enable the creation of magic dimple traps, significantly reducing dephasing caused by differential light shifts. Such a dimple trap could potentially be combined with a one-dimensional trap aligned along the probe beam axis, offering improved control over atomic motion and coherence.

The ability demonstrated in this thesis to modify the trapping potential experienced by the Rydberg state without affecting the ground state potential has broader applicability in experiments involving Rydberg atoms. It provides a means to engineer tailored trapping potentials specifically for Rydberg states or to exploit the differential light shift for fine control over the two-photon transition frequency into Rydberg states.

APPENDIX A

Gauge Invariance of the Dynamic Polarizability

The energy corrections in Eq. 3.14 and Eq. 3.15 from the main text are calculated in the Coulomb gauge. In the literature, polarizabilities are often calculated by a sum-over-states approach [59, 112, 113, 127]. In this appendix, we calculate and visualize the dynamic polarizabilities in two different gauges [51].

The energy corrections from the interaction Hamiltonians proportional to $\boldsymbol{A}(\boldsymbol{r}+\boldsymbol{r}_\mathrm{e},t)\cdot\hat{\boldsymbol{p}}_\mathrm{e}$ and $\boldsymbol{A}^2(\boldsymbol{r}+\boldsymbol{r}_\mathrm{e},t)$ are given in the main text as

$$
\begin{aligned}
U_q^{(1)}(\boldsymbol{r}) &= -\left[-\sum_{j\neq q}\frac{\omega_{qj}^2}{\omega^2}\frac{1}{\hbar}\left(\frac{\left|\langle q|e\,\boldsymbol{\epsilon}\cdot\boldsymbol{r}_\mathrm{e}|j\rangle\right|^2}{\omega_{qj}-\omega}+\frac{\left|\langle q|e\,\boldsymbol{\epsilon}^*\cdot\boldsymbol{r}_\mathrm{e}|j\rangle\right|^2}{\omega_{qj}+\omega}\right)\right]\cdot\omega^2|\boldsymbol{A}(\boldsymbol{r})|^2,\\
U_q^{(2)}(\boldsymbol{r}) &= -\alpha_f\omega^2\left\langle q|\boldsymbol{A}(\boldsymbol{r}+\boldsymbol{r}_\mathrm{e})\boldsymbol{A}^*(\boldsymbol{r}+\boldsymbol{r}_\mathrm{e})|q\right\rangle,
\end{aligned}
$$

with the free-electron polarizability $\alpha_f=-e^2/m_\mathrm{e}\omega^2$. For the following calculation, we only consider the polarizability-like terms

$$
\begin{aligned}
\alpha_{q,\mathrm{CG}}^{(1)} &= -\sum_{j\neq q}\frac{\omega_{qj}^2}{\omega^2}\frac{1}{\hbar}\left(\frac{\left|\langle q|e\,\boldsymbol{\epsilon}\cdot\boldsymbol{r}_\mathrm{e}|j\rangle\right|^2}{\omega_{qj}-\omega}+\frac{\left|\langle q|e\,\boldsymbol{\epsilon}^*\cdot\boldsymbol{r}_\mathrm{e}|j\rangle\right|^2}{\omega_{qj}+\omega}\right),\\
\alpha_{q,\mathrm{CG}}^{(2)} &= \alpha_f,
\end{aligned}
\tag{A.1}
$$

where the subscript in $\alpha_{q,\mathrm{CG}}^{(1)}$ denotes that the polarizability for state q is calculated in the Coulomb gauge (CG). The denominator in Eq. A.1 can be rewritten to

$$
\begin{aligned}
\alpha_{q,\mathrm{CG}}^{(1)} &= -\sum_{j\neq q}\frac{\omega_{qj}^3}{\omega^2}\frac{2}{\hbar}\frac{\left|\langle q|e\,\boldsymbol{\epsilon}\cdot\boldsymbol{r}_\mathrm{e}|j\rangle\right|^2}{\omega_{qj}^2-\omega^2},\\
\alpha_{q,\mathrm{CG}}^{(2)} &= \alpha_f.
\end{aligned}
$$

The contribution from $\alpha_{q,\mathrm{CG}}^{(1)}$ can be decomposed in a scalar, a vector and a tensor part [113]. Here,

we only consider the scalar part and write the polarizabilities as

$$\alpha^{(1)}_{q,\mathrm{CG}} = -\sum_{j\neq q} \frac{2}{3\hbar}\frac{\omega^3_{qj}}{\omega^2}\frac{|\langle q|e\,\boldsymbol{r}_\mathrm{e}|j\rangle|^2}{\omega^2_{qj}-\omega^2},$$
$$\alpha^{(2)}_{q,\mathrm{CG}} = \alpha_f.$$

The total polarizability for state q from our calculation in the Coulomb gauge is given by

$$\begin{aligned}\alpha_{q,\mathrm{CG}} &= \alpha^{(1)}_{q,\mathrm{CG}} + \alpha^{(2)}_{q,\mathrm{CG}},\\ &= -\sum_{j\neq q} \frac{2}{3\hbar}\frac{\omega^3_{qj}}{\omega^2}\frac{|\langle q|e\,\boldsymbol{r}_\mathrm{e}|j\rangle|^2}{\omega^2_{qj}-\omega^2} + \alpha_f.\end{aligned} \tag{A.2}$$

This equation can be reformulated by including the term $\alpha_f = -e^2/m_\mathrm{e}\omega^2$ into the sum as shown in Ref. [51]. The calculation uses the oscillator sum rule given by

$$-\frac{m_\mathrm{e}}{3e^2}\sum_{j\neq q}\frac{\omega_{qj}}{\hbar}|\langle q|e\,\boldsymbol{\epsilon}\cdot\boldsymbol{r}_\mathrm{e}|j\rangle|^2 = 1. \tag{A.3}$$

Figure A.1(a) shows the cumulative sum over coupled states $5 \leq j \leq 130$ for different states $|q\rangle$. The resulting polarizability is given by [51]

$$\alpha_{q,\mathrm{LG}} = -\sum_{j\neq q}\frac{2\omega_{qj}}{3\hbar}\frac{|\langle q|e\,\boldsymbol{\epsilon}\cdot\boldsymbol{r}_\mathrm{e}|j\rangle|^2}{\omega^2_{qj}-\omega^2}, \tag{A.4}$$

which matches with the calculation for the polarizability in the length gauge.

Figure A.1(b) and A.1(c) shows the contributions in Eq. A.2 and Eq. A.4 for the ground state $5S_{1/2}$ and the Rydberg state $45S_{1/2}$ in rubidium-87, respectively. For the ground state, the length gauge polarizability $\alpha_{g,\mathrm{LG}}$ is the generally used polarizability [79]. In the Coulomb gauge, the polarizability $\alpha^{(1)}_{g,\mathrm{CG}}$ diverges for long wavelength. The experimentally observed polarizability α_g is recovered only by also considering the free-electron contribution α_f. The Rydberg state polarizability $\alpha_{r,\mathrm{CG}}$ in Fig A.1(c) is well described by the free-electron polarizability, as the contribution $\alpha^{(1)}_{r,\mathrm{CG}}$ is vanishingly small. The negative polarizability originates from the $\boldsymbol{A}^2(\boldsymbol{r}+\boldsymbol{r}_\mathrm{e},t)$ term, which sometimes is called diamagnetic term. The movement of the Rydberg electron in the non-uniform electromagnetic field leads to a repulsive force onto the entire Rydberg atom [49]. This phenomenon is similar to the diamagnetic behavior of atoms in a magnetic field [172]. Diamagnetism refers to the property of materials to be repelled by external magnetic fields. The material creates an induced magnetic dipole moment that is oriented opposite of the external field. The resulting force pushes a diamagnetic object away from high field intensities.

The overall negative dynamic polarizability of the Rydberg state in Fig. A.1(c) can be perturbed by the near-resonant coupling to lower-lying atomic states. The near-resonant coupling is used to form the magic trap discussed in Chapter 5.

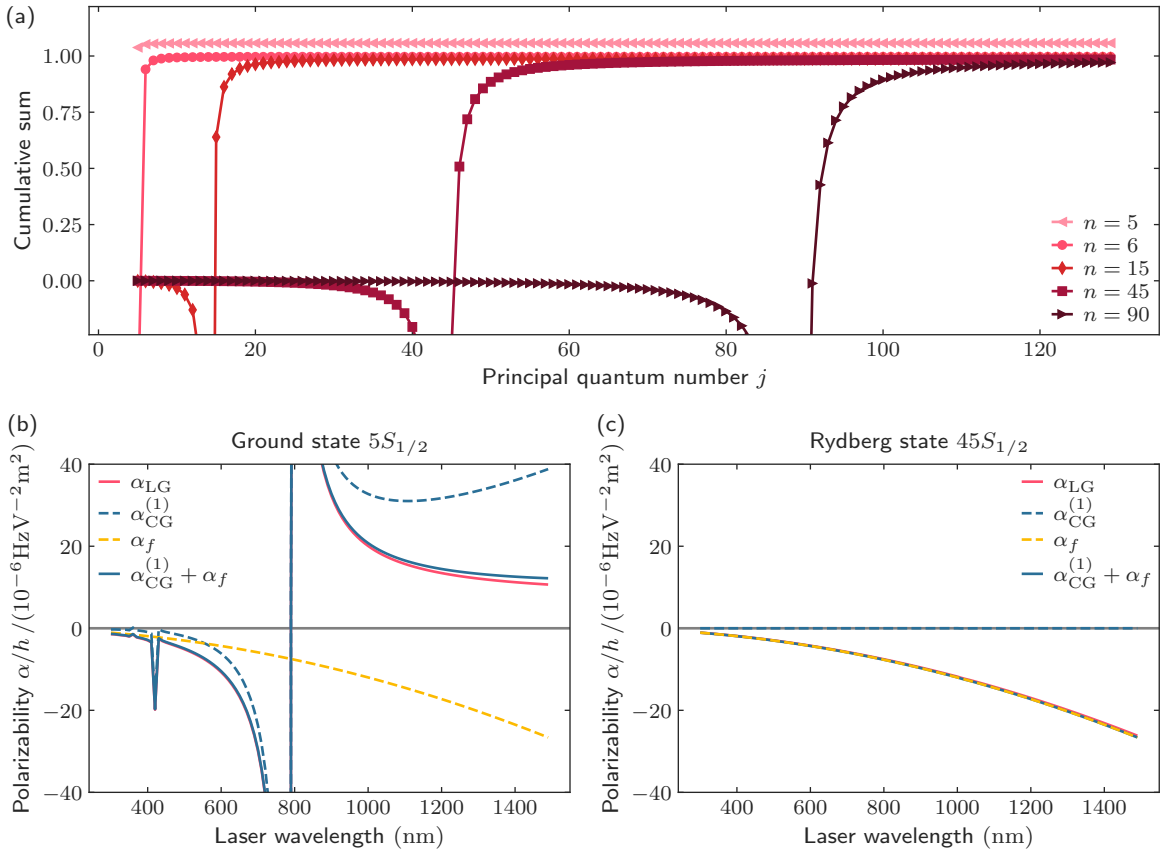

Figure A.1: (a) The cumulative sum over the states with principal quantum number j in Eq. A.3 for different atomic states $|n\rangle$. The sum approaches unity, when considering enough states j above the target state n. (b), (c) The different scalar polarizability contributions for (b) the ground state $5S$ and (c) the Rydberg state $45S$, from the calculation in the Coulomb gauge (CG) and in the length gauge (LG). For the ground state polarizability, the first two resonances to the states $5P$ and $6P$ are visible. For the Rydberg state, no resonances are visible as they are not resolved by the coarse wavelength axis.

Bibliography

[1] L. Ahlheit, C. Nill, D. Svirskiy, J. de Haan, S. Schroers, W. Alt, N. Stiesdal, I. Lesanovsky, and S. Hofferberth, *Magic running- and standing-wave optical traps for Rydberg atoms*, Physical Review A **111** (2025) 013115.

[2] J. I. Cirac, P. Zoller, H. J. Kimble, and H. Mabuchi, *Quantum State Transfer and Entanglement Distribution among Distant Nodes in a Quantum Network*, Physical Review Letters **78** (1997) 3221.

[3] T. E. Northup and R. Blatt, *Quantum information transfer using photons*, Nature Photonics **8** (2014) 356.

[4] T. F. Walsh and P. Zerwas, *Two-photon processes in the parton model*, Physics Letters B **44** (1973) 195.

[5] J. M. Raimond, M. Brune, and S. Haroche, *Manipulating quantum entanglement with atoms and photons in a cavity*, Reviews of Modern Physics **73** (2001) 565.

[6] A. Reiserer and G. Rempe, *Cavity-based quantum networks with single atoms and optical photons*, Reviews of Modern Physics **87** (2015) 1379.

[7] A. Boca, R. Miller, K. M. Birnbaum, A. D. Boozer, J. McKeever, and H. J. Kimble, *Observation of the Vacuum Rabi Spectrum for One Trapped Atom*, Physical Review Letters **93** (2004) 233603.

[8] P. Maunz, T. Puppe, I. Schuster, N. Syassen, P. W. H. Pinkse, and G. Rempe, *Normal-Mode Spectroscopy of a Single-Bound-Atom–Cavity System*, Physical Review Letters **94** (2005) 033002.

[9] T. G. Tiecke, J. D. Thompson, N. P. de Leon, L. R. Liu, V. Vuletić, and M. D. Lukin, *Nanophotonic quantum phase switch with a single atom*, Nature **508** (2014) 241.

[10] I. Shomroni, S. Rosenblum, Y. Lovsky, O. Bechler, G. Guendelman, and B. Dayan, *All-optical routing of single photons by a one-atom switch controlled by a single photon*, Science **345** (2014) 903.

[11] B. Hacker, S. Welte, G. Rempe, and S. Ritter, *A photon–photon quantum gate based on a single atom in an optical resonator*, Nature **536** (2016) 193.

[12] K.-J. Boller, A. Imamoğlu, and S. E. Harris, *Observation of electromagnetically induced transparency*, Physical Review Letters **66** (1991) 2593.

[13] M. Bajcsy, A. S. Zibrov, and M. D. Lukin, *Stationary pulses of light in an atomic medium*, Nature **426** (2003) 638.

[14] M. Fleischhauer and M. D. Lukin, *Dark-State Polaritons in Electromagnetically Induced Transparency*, Physical Review Letters **84** (2000) 5094.

[15] D. F. Phillips, A. Fleischhauer, A. Mair, R. L. Walsworth, and M. D. Lukin, *Storage of Light in Atomic Vapor*, Physical Review Letters **86** (2001) 783.

[16] C. Liu, Z. Dutton, C. H. Behroozi, and L. V. Hau, *Observation of coherent optical information storage in an atomic medium using halted light pulses*, Nature **409** (2001) 490.

[17] M. Fleischhauer and M. D. Lukin, *Quantum memory for photons: Dark-state polaritons*, Physical Review A **65** (2002) 022314.

[18] B. Zhao, Y.-A. Chen, X.-H. Bao, T. Strassel, C.-S. Chuu, X.-M. Jin, J. Schmiedmayer, Z.-S. Yuan, S. Chen, and J.-W. Pan, *A millisecond quantum memory for scalable quantum networks*, Nature Physics **5** (2009) 95.

[19] A. I. Lvovsky, B. C. Sanders, and W. Tittel, *Optical quantum memory*, Nature Photonics **3** (2009) 706.

[20] S. Zhang, J. Shi, Z. Cui, Y. Wang, Y. Wu, L. Duan, and Y. Pu, *Realization of a Programmable Multipurpose Photonic Quantum Memory with Over-Thousand Qubit Manipulations*, Physical Review X **14** (2024) 021018.

[21] F. Hoffet, J. Lowinski, L. Heller, A. Padrón-Brito, and H. de Riedmatten, *Near-Unity Indistinguishability of Single Photons Emitted from Dissimilar and Independent Atomic Quantum Nodes*, PRX Quantum **5** (2024) 030305.

[22] T. F. Gallagher, *Rydberg Atoms*, Cambridge Monographs on Atomic, Molecular and Chemical Physics, Cambridge: Cambridge University Press, 1994, ISBN: 978-0-521-02166-1.

[23] M. D. Lukin, M. Fleischhauer, R. Cote, L. M. Duan, D. Jaksch, J. I. Cirac, and P. Zoller, *Dipole Blockade and Quantum Information Processing in Mesoscopic Atomic Ensembles*, Physical Review Letters **87** (2001) 037901.

[24] M. Saffman and T. G. Walker, *Creating single-atom and single-photon sources from entangled atomic ensembles*, Physical Review A **66** (2002) 065403.

[25] D. Tong, S. M. Farooqi, J. Stanojevic, S. Krishnan, Y. P. Zhang, R. Côté, E. E. Eyler, and P. L. Gould, *Local Blockade of Rydberg Excitation in an Ultracold Gas*, Physical Review Letters **93** (2004) 063001.

[26] E. Urban, T. A. Johnson, T. Henage, L. Isenhower, D. D. Yavuz, T. G. Walker, and M. Saffman, *Observation of Rydberg blockade between two atoms*, Nature Physics **5** (2009) 110.

[27] A. Gaëtan, Y. Miroshnychenko, T. Wilk, A. Chotia, M. Viteau, D. Comparat, P. Pillet, A. Browaeys, and P. Grangier, *Observation of collective excitation of two individual atoms in the Rydberg blockade regime*, Nature Physics **5** (2009) 115.

[28] J. D. Pritchard, D. Maxwell, A. Gauguet, K. J. Weatherill, M. P. A. Jones, and C. S. Adams, *Cooperative atom-light interaction in a blockaded rydberg ensemble*, Physical Review Letters **105** (2010).

[29] Y. O. Dudin, L. Li, F. Bariani, and A. Kuzmich, *Observation of coherent many-body Rabi oscillations*, Nature Physics **8** (2012) 790.

[30] A. Paris-Mandoki, C. Braun, J. Kumlin, C. Tresp, I. Mirgorodskiy, F. Christaller, H. P. Büchler, and S. Hofferberth, *Free-space quantum electrodynamics with a single rydberg superatom*, Physical Review X **7** (2017) 041010.

[31] J. Lowinski, L. Heller, F. Hoffet, A. Padrón-Brito, K. Theophilo, and H. de Riedmatten, *Strongly Nonlinear Interaction between Nonclassical Light and a Blockaded Rydberg Atomic Ensemble*, Physical Review Letters **132** (2024) 053001.

[32] T. Peyronel, O. Firstenberg, Q.-Y. Liang, S. Hofferberth, A. V. Gorshkov, T. Pohl, M. D. Lukin, and V. Vuletić, *Quantum nonlinear optics with single photons enabled by strongly interacting atoms*, Nature **488** (2012) 57.

[33] B. Kim, K.-T. Chen, K.-Y. Chen, Y.-S. Chiu, C.-Y. Hsu, Y.-H. Chen, and I. A. Yu, *Experimental demonstration of stationary dark-state polaritons dressed by dipole-dipole interaction*, Physical Review Letters **131** (2023) 133001.

[34] O. Firstenberg, T. Peyronel, Q.-Y. Liang, A. V. Gorshkov, M. D. Lukin, and V. Vuletić, *Attractive photons in a quantum nonlinear medium*, Nature **502** (2013) 71.

[35] S. H. Cantu, A. V. Venkatramani, W. Xu, L. Zhou, B. Jelenković, M. D. Lukin, and V. Vuletić, *Repulsive photons in a quantum nonlinear medium*, Nature Physics **16** (2020) 921.

[36] H. Gorniaczyk, C. Tresp, J. Schmidt, H. Fedder, and S. Hofferberth, *Single-Photon Transistor Mediated by Interstate Rydberg Interactions*, Physical Review Letters **113** (2014) 053601.

[37] S. Baur, D. Tiarks, G. Rempe, and S. Dürr, *Single-Photon Switch Based on Rydberg Blockade*, Physical Review Letters **112** (2014) 073901.

[38] D. Tiarks, S. Schmidt, G. Rempe, and S. Dürr, *Optical π phase shift created with a single-photon pulse*, Science Advances **2** (2016) e1600036.

[39] T. Stolz, H. Hegels, M. Winter, B. Röhr, Y.-F. Hsiao, L. Husel, G. Rempe, and S. Dürr, *Quantum-Logic Gate between Two Optical Photons with an Average Efficiency above 40%*, Physical Review X **12** (2022) 021035.

[40] Y. Lei, F. K. Asadi, T. Zhong, A. Kuzmich, C. Simon, and M. Hosseini, *Quantum optical memory for entanglement distribution*, Optica **10** (2023) 1511.

[41] C. Mewes and M. Fleischhauer, *Decoherence in collective quantum memories for photons*, Physical Review A **72** (2005) 022327.

[42] F. Bariani, Y. O. Dudin, T. A. B. Kennedy, and A. Kuzmich, *Dephasing of Multiparticle Rydberg Excitations for Fast Entanglement Generation*, Physical Review Letters **108** (2012) 030501.

[43] R. Zhao, Y. O. Dudin, S. D. Jenkins, C. J. Campbell, D. N. Matsukevich, T. a. B. Kennedy, and A. Kuzmich, *Long-lived quantum memory*, Nature Physics **5** (2009) 100.

[44] L. Li and A. Kuzmich, *Quantum memory with strong and controllable Rydberg-level interactions*, Nature Communications **7** (2016) 13618.

[45] Y. O. Dudin, L. Li, and A. Kuzmich, *Light storage on the time scale of a minute*, Physical Review A **87** (2013) 031801.

[46] Y. Jiao, C. Li, X.-F. Shi, J. Fan, J. Bai, S. Jia, J. Zhao, and C. S. Adams, *Suppression of Motional Dephasing Using State Mapping*, Physical Review Letters **134** (2025) 053604.

[47] C. P. Sun, S. Yi, and L. You, *Decoherence of collective atomic spin states due to inhomogeneous coupling*, Physical Review A **67** (2003) 063815.

[48] S. Schmidt-Eberle, T. Stolz, G. Rempe, and S. Dürr, *Dark-time decay of the retrieval efficiency of light stored as a Rydberg excitation in a noninteracting ultracold gas*, Physical Review A **101** (2020) 013421.

[49] M. Saffman and T. G. Walker, *Analysis of a quantum logic device based on dipole-dipole interactions of optically trapped Rydberg atoms*, Physical Review A **72** (2005) 022347.

[50] S. K. Dutta, J. R. Guest, D. Feldbaum, A. Walz-Flannigan, and G. Raithel, *Ponderomotive Optical Lattice for Rydberg Atoms*, Physical Review Letters **85** (2000) 5551.

[51] T. Topcu and A. Derevianko, *Dynamic polarizability of Rydberg atoms: Applicability of the near-free-electron approximation, gauge invariance, and the Dirac sea*, Physical Review A **88** (2013) 042510.

[52] H. Katori, T. Ido, and M. Kuwata-Gonokami, *Optimal Design of Dipole Potentials for Efficient Loading of Sr Atoms*, Journal of the Physical Society of Japan **68** (1999) 2479.

[53] F. Le Kien, V. I. Balykin, and K. Hakuta, *State-Insensitive Trapping and Guiding of Cesium Atoms Using a Two-Color Evanescent Field around a Subwavelength-Diameter Fiber*, Journal of the Physical Society of Japan **74** (2005) 910.

[54] L. Isenhower, W. Williams, A. Dally, and M. Saffman, *Atom trapping in an interferometrically generated bottle beam trap*, Optics Letters **34** (2009) 1159.

[55] S. Zhang, F. Robicheaux, and M. Saffman, *Magic-wavelength optical traps for Rydberg atoms*, Physical Review A **84** (2011) 043408.

[56] M. S. Safronova, C. J. Williams, and C. W. Clark, *Optimizing the fast Rydberg quantum gate*, Physical Review A **67** (2003) 040303.

[57] T. Topcu and A. Derevianko, *Intensity landscape and the possibility of magic trapping of alkali-metal Rydberg atoms in infrared optical lattices*, Physical Review A: Atomic, Molecular, and Optical Physics **88** (2013) 043407.

[58] T. Topcu and A. Derevianko, *Tune-out wavelengths and landscape-modulated polarizabilities of alkali-metal Rydberg atoms in infrared optical lattices*, Physical Review A **88** (2013).

[59] E. A. Goldschmidt, D. G. Norris, S. B. Koller, R. Wyllie, R. C. Brown, J. V. Porto, U. I. Safronova, and M. S. Safronova, *Magic wavelengths for the* $5s$–$18s$ *transition in rubidium*, Physical Review A **91** (2015) 032518.

[60] J. Lampen, H. Nguyen, L. Li, P. R. Berman, and A. Kuzmich, *Long-lived coherence between ground and Rydberg levels in a magic-wavelength lattice*, Physical Review A **98** (2018) 033411.

[61] N. Stiesdal, *Collective atom-light interactions with Rydberg superatoms*, PhD thesis: University of Southern Denmark, 2022.

[62] S. E. Harris, J. E. Field, and A. Imamoğlu, *Nonlinear optical processes using electromagnetically induced transparency*, Physical Review Letters **64** (1990) 1107.

[63] G. Alzetta, A. Gozzini, L. Moi, and G. Orriols, *An experimental method for the observation of r.f. transitions and laser beat resonances in oriented Na vapour*, Il Nuovo Cimento B (1971-1996) **36** (1976) 5.

[64] M. Fleischhauer, A. Imamoglu, and J. P. Marangos, *Electromagnetically induced transparency: Optics in coherent media*, Reviews of Modern Physics **77** (2005) 633.

[65] J. Deiglmayr, M. Reetz-Lamour, T. Amthor, S. Westermann, A. L. de Oliveira, and M. Weidemüller, *Coherent excitation of Rydberg atoms in an ultracold gas*, Optics Communications, Quantum Control of Light and Matter **264** (2006) 293.

[66] L. V. Hau, S. E. Harris, Z. Dutton, and C. H. Behroozi, *Light speed reduction to 17 metres per second in an ultracold atomic gas*, Nature **397** (1999) 594.

[67] L.-M. Duan, M. D. Lukin, J. I. Cirac, and P. Zoller, *Long-distance quantum communication with atomic ensembles and linear optics*, Nature **414** (2001) 413.

[68] R. H. Dicke, *Coherence in Spontaneous Radiation Processes*, Physical Review **93** (1954) 99.

[69] M. O. Scully, E. S. Fry, C. H. R. Ooi, and K. Wódkiewicz, *Directed Spontaneous Emission from an Extended Ensemble of N Atoms: Timing Is Everything*, Physical Review Letters **96** (2006) 010501.

[70] S. D. Jenkins, T. Zhang, and T. A. B. Kennedy, *Motional dephasing of atomic clock spin waves in an optical lattice*, Journal of Physics B: Atomic, Molecular and Optical Physics **45** (2012) 124005.

[71] T. W. Hänsch and A. L. Schawlow, *Cooling of gases by laser radiation*, Optics Communications **13** (1975) 68.

[72] D. Wineland and H. Dehmelt, *Proposed* 10^{14} $\nu/\Delta\nu$ *laser fluorescence spectroscopy on* $T1^{+}$ *monoion oscillator II*, Bull. Am. Phys. Soc. **20** (1975) 60.

[73] A. L. Migdall, J. V. Prodan, W. D. Phillips, T. H. Bergeman, and H. J. Metcalf, *First Observation of Magnetically Trapped Neutral Atoms*, Physical Review Letters **54** (1985) 2596.

[74] Y. He, L. Ji, Y. Wang, L. Qiu, J. Zhao, Y. Ma, X. Huang, S. Wu, and D. E. Chang, *Geometric Control of Collective Spontaneous Emission*, Physical Review Letters **125** (2020) 213602.

[75] J. R. Boon, E. Zekou, D. McGloin, and M. H. Dunn, *Comparison of wavelength dependence in cascade-, Λ-, and Vee-type schemes for electromagnetically induced transparency*, Physical Review A **59** (1999) 4675.

[76] A. K. Mohapatra, T. R. Jackson, and C. S. Adams, *Coherent Optical Detection of Highly Excited Rydberg States Using Electromagnetically Induced Transparency*, Physical Review Letters **98** (2007) 113003.

[77] M. Saffman, T. G. Walker, and K. Mølmer, *Quantum information with Rydberg atoms*, Reviews of Modern Physics **82** (2010) 2313.

[78] S. Weber, C. Tresp, H. Menke, A. Urvoy, O. Firstenberg, H. P. Büchler, and S. Hofferberth, *Calculation of Rydberg interaction potentials*, Journal of Physics B: Atomic, Molecular and Optical Physics **50** (2017) 133001.

[79] E. J. Robertson, N. Šibalić, R. M. Potvliege, and M. P. A. Jones, *ARC 3.0: An expanded Python toolbox for atomic physics calculations*, Computer Physics Communications **261** (2021) 107814.

[80] M. S. O'Sullivan and B. P. Stoicheff, *Scalar polarizabilities and avoided crossings of high Rydberg states in Rb*, Physical Review A **31** (1985) 2718.

[81] R. Löw, H. Weimer, J. Nipper, J. B. Balewski, B. Butscher, H. P. Büchler, and T. Pfau, *An experimental and theoretical guide to strongly interacting Rydberg gases*, Journal of Physics B: Atomic, Molecular and Optical Physics **45** (2012) 113001.

[82] I. I. Beterov, I. I. Ryabtsev, D. B. Tretyakov, and V. M. Entin, *Quasiclassical calculations of blackbody-radiation-induced depopulation rates and effective lifetimes of Rydberg nS, nP, and nD alkali-metal atoms with $n < 80$*, Physical Review A **79** (2009) 052504.

[83] M. Mack, F. Karlewski, H. Hattermann, S. Höckh, F. Jessen, D. Cano, and J. Fortágh, *Measurement of absolute transition frequencies of ^{87}Rb to nS and nD Rydberg states by means of electromagnetically induced transparency*, Physical Review A **83** (2011) 052515.

[84] K. Singer, J. Stanojevic, M. Weidemüller, and R. Côté, *Long-range interactions between alkali Rydberg atom pairs correlated to the ns–ns, np–np and nd–nd asymptotes*, Journal of Physics B: Atomic, Molecular and Optical Physics **38** (2005) S295.

[85] A. Reinhard, T. C. Liebisch, B. Knuffman, and G. Raithel, *Level shifts of rubidium Rydberg states due to binary interactions*, Physical Review A **75** (2007) 032712.

[86] A. Browaeys, D. Barredo, and T. Lahaye,
Experimental investigations of dipole–dipole interactions between a few Rydberg atoms,
Journal of Physics B: Atomic, Molecular and Optical Physics **49** (2016) 152001.

[87] J. Zeiher, P. Schauß, S. Hild, T. Macrì, I. Bloch, and C. Gross,
Microscopic Characterization of Scalable Coherent Rydberg Superatoms,
Physical Review X **5** (2015) 031015.

[88] N. Stiesdal, H. Busche, J. Kumlin, K. Kleinbeck, H. P. Büchler, and S. Hofferberth,
Observation of collective decay dynamics of a single Rydberg superatom,
Phys. Rev. Research 2, 043339 (2020) (2020), arXiv: 2005.05089 [quant-ph].

[89] B. Yang, Y. Li, S. Nie, Y. Mei, H. Nguyen, P. R. Berman, and A. Kuzmich,
Dipole Moment of a Superatom, Physical Review Letters **133** (2024) 213601.

[90] C. Tresp, C. Zimmer, I. Mirgorodskiy, H. Gorniaczyk, A. Paris-Mandoki, and S. Hofferberth,
Single-Photon Absorber Based on Strongly Interacting Rydberg Atoms,
Physical Review Letters **117** (2016) 223001.

[91] N. Stiesdal, H. Busche, K. Kleinbeck, J. Kumlin, M. G. Hansen, H. P. Büchler, and S. Hofferberth, *Controlled multi-photon subtraction with cascaded Rydberg superatoms as single-photon absorbers*, Nature Communications **12** (2021) 4328.

[92] I. Lesanovsky and J. P. Garrahan,
Out-of-equilibrium structures in strongly interacting Rydberg gases with dissipation,
Physical Review A **90** (2014) 011603.

[93] A. Urvoy, F. Ripka, I. Lesanovsky, D. Booth, J. P. Shaffer, T. Pfau, and R. Löw,
Strongly correlated growth of rydberg aggregates in a vapor cell,
Physical Review Letters **114** (2015) 203002.

[94] M. M. Valado, C. Simonelli, M. D. Hoogerland, I. Lesanovsky, J. P. Garrahan, E. Arimondo, D. Ciampini, and O. Morsch,
Experimental observation of controllable kinetic constraints in a cold atomic gas,
Physical Review A **93** (2016) 040701.

[95] C. Pérez-Espigares, M. Marcuzzi, R. Gutiérrez, and I. Lesanovsky,
Epidemic Dynamics in Open Quantum Spin Systems,
Physical Review Letters **119** (2017) 140401.

[96] T. M. Wintermantel, M. Buchhold, S. Shevate, M. Morgado, Y. Wang, G. Lochead, S. Diehl, and S. Whitlock,
Epidemic growth and Griffiths effects on an emergent network of excited atoms,
Nature Communications **12** (2021) 103.

[97] D. Brady and M. Fleischhauer,
Mean-field approach to Rydberg facilitation in a gas of atoms at high and low temperatures,
Physical Review A **108** (2023) 052812.

[98] D. Brady, J. Bender, P. Mischke, S. Ohler, T. Niederprüm, H. Ott, and M. Fleischhauer,
Griffiths phase in a facilitated Rydberg gas at low temperatures,
Physical Review Research **6** (2024) 013052.

[99] H. Busche, P. Huillery, S. W. Ball, T. Ilieva, M. P. A. Jones, and C. S. Adams, *Contactless nonlinear optics mediated by long-range Rydberg interactions*, Nature Physics **13** (2017) 655.

[100] D. Maxwell, D. J. Szwer, D. Paredes-Barato, H. Busche, J. D. Pritchard, A. Gauguet, K. J. Weatherill, M. P. A. Jones, and C. S. Adams, *Storage and Control of Optical Photons Using Rydberg Polaritons*, Physical Review Letters **110** (2013) 103001.

[101] P. Lunt, *Design and Construction of a New Ultracold Ytterbium Experiment for Rydberg Physics*, MA thesis: University of Southern Denmark, 2019.

[102] X.-F. Shi, *Suppressing Motional Dephasing of Ground-Rydberg Transition for High-Fidelity Quantum Control with Neutral Atoms*, Physical Review Applied **13** (2020) 024008.

[103] S. Kuhr, W. Alt, D. Schrader, I. Dotsenko, Y. Miroshnychenko, W. Rosenfeld, M. Khudaverdyan, V. Gomer, A. Rauschenbeutel, and D. Meschede, *Coherence Properties and Quantum State Transportation in an Optical Conveyor Belt*, Physical Review Letters **91** (2003) 213002.

[104] S. Kuhr, W. Alt, D. Schrader, I. Dotsenko, Y. Miroshnychenko, A. Rauschenbeutel, and D. Meschede, *Analysis of dephasing mechanisms in a standing-wave dipole trap*, Physical Review A **72** (2005) 023406.

[105] J. Simon, H. Tanji, J. K. Thompson, and V. Vuletić, *Interfacing Collective Atomic Excitations and Single Photons*, Physical Review Letters **98** (2007) 183601.

[106] M. O. Scully and M. S. Zubairy, *Quantum Optics*, Cambridge: Cambridge University Press, 1997, ISBN: 978-0-521-43595-6.

[107] K. Rzążewski and R. W. Boyd, *Equivalence of interaction hamiltonians in the electric dipole approximation*, Journal of Modern Optics **51** (2004) 1137.

[108] P. W. Milonni, *The Quantum Vacuum: An Introduction to Quantum Electrodynamics*, Elsevier Science, 1994, ISBN: 978-0-12-498080-8.

[109] F. Le Kien, P. Schneeweiss, and A. Rauschenbeutel, *Dynamical polarizability of atoms in arbitrary light fields: general theory and application to cesium*, The European Physical Journal D **67** (2013).

[110] S. Chu, J. E. Bjorkholm, A. Ashkin, and A. Cable, *Experimental Observation of Optically Trapped Atoms*, Physical Review Letters **57** (1986) 314.

[111] J. D. Miller, R. A. Cline, and D. J. Heinzen, *Far-off-resonance optical trapping of atoms*, Physical Review A **47** (1993) R4567.

[112] R. Grimm, M. Weidemüller, and Y. B. Ovchinnikov, "Optical Dipole Traps for Neutral Atoms," *Advances In Atomic, Molecular, and Optical Physics*, ed. by B. Bederson and H. Walther, vol. 42, Academic Press, 2000 95.

[113] D. A. Steck, *Quantum and Atom Optics*, 2024.

[114] J. de Haan, *Characterization of a 1D magic wavelength lattice for increasing the coherence time of Rydberg superatoms*, MA thesis: University of Bonn, 2024.

[115] N. B. Delone and V. P. Kraĭnov, *Atoms in strong light fields*,
Rearranged, updated ed. of Russian orig., Springer series in chemical physics 28,
Berlin Heidelberg New York [etc.]: Springer-Verl, 1985,
ISBN: 978-3-540-12412-2 978-0-387-12412-4.

[116] E. A. Power and S. Zienau,
Coulomb gauge in non-relativistic quantum electro-dynamics and the shape of spectral lines,
Philosophical Transactions of the Royal Society of London. Series A, Mathematical and Physical Sciences **251** (1959) 427.

[117] J. D. Jackson, *Classical electrodynamics*, 3rd ed, New York: Wiley, 1999,
ISBN: 978-0-471-30932-1.

[118] H. A. Kramers and W. Heisenberg, *Über die Streuung von Strahlung durch Atome*,
Zeitschrift für Physik **31** (1925) 681.

[119] P. H. Bucksbaum, M. Bashkansky, and T. J. McIlrath,
Scattering of electrons by intense coherent light, Physical Review Letters **58** (1987) 349.

[120] J. J. Sakurai, *Modern Quantum Mechanics*, 3rd ed,
Cambridge: Cambridge University Press, 2020, ISBN: 978-1-108-64592-8.

[121] M. Aymar, C. H. Greene, and E. Luc-Koenig,
Multichannel Rydberg spectroscopy of complex atoms,
Reviews of Modern Physics **68** (1996) 1015.

[122] N. L. Manakov, V. D. Ovsiannikov, and L. P. Rapoport, *Atoms in a laser field*,
Physics Reports **141** (1986) 320.

[123] P. Rosenbusch, S. Ghezali, V. A. Dzuba, V. V. Flambaum, K. Beloy, and A. Derevianko,
ac Stark shift of the Cs microwave atomic clock transitions,
Physical Review A **79** (2009) 013404.

[124] L. D. Landau, *Quantum mechanics: non-relativistic theory*, 3d ed., rev. and enl,
Their Course of theoretical physics v. 3, Oxford New York: Pergamon Press, 1977,
ISBN: 978-0-08-020940-1.

[125] J. D. Jackson, *Classical Electrodynamics*, New York: John Wiley & Sons, 1962.

[126] M. Traini, *Electric polarizability of the hydrogen atom: a sum rule approach*,
European Journal of Physics **17** (1996) 30.

[127] J. Mitroy, M. S. Safronova, and C. W. Clark,
Theory and applications of atomic and ionic polarizabilities,
Journal of Physics B: Atomic, Molecular and Optical Physics **43** (2010) 202001.

[128] S. Friebel, C. D'Andrea, J. Walz, M. Weitz, and T. W. Hänsch,
CO_2*-laser optical lattice with cold rubidium atoms*, Physical Review A **57** (1998) R20.

[129] H. M. Gorniaczyk,
Single Photon Transistor mediated by electrically tunable Rydberg-Rydberg Interactions,
PhD thesis: Universität Stuttgart 5. Physikalisches Institut, 2016.

[130] E. L. Raab, M. Prentiss, A. Cable, S. Chu, and D. E. Pritchard,
Trapping of Neutral Sodium Atoms with Radiation Pressure,
Physical Review Letters **59** (1987) 2631.

[131] J. Ye, S. Swartz, P. Jungner, and J. L. Hall,
Hyperfine structure and absolute frequency of the $^{87}Rb\ 5P_{3/2}$ state,
Optics Letters **21** (1996) 1280.

[132] G. P. Barwood, P. Gill, and W. R. C. Rowley, *Frequency measurements on optically narrowed Rb-stabilised laser diodes at 780 nm and 795 nm*, Applied Physics B **53** (1991) 142.

[133] R. F. Gutterres, C. Amiot, A. Fioretti, C. Gabbanini, M. Mazzoni, and O. Dulieu,
Determination of the ^{87}Rb 5p state dipole matrix element and radiative lifetime from the photoassociation spectroscopy of the Rb_2 0_g^- $(P_{3/2})$ long-range state,
Physical Review A **66** (2002) 024502.

[134] E. D. Black, *An introduction to Pound–Drever–Hall laser frequency stabilization*,
American Journal of Physics **69** (2001) 79.

[135] J. A. Boyd and T. Lahaye,
A basic introduction to ultrastable optical cavities for laser stabilization,
American Journal of Physics **92** (2024) 50.

[136] U. Schünemann, H. Engler, R. Grimm, M. Weidemüller, and M. Zielonkowski,
Simple scheme for tunable frequency offset locking of two lasers,
Review of Scientific Instruments **70** (1999) 242.

[137] J. Appel, A. MacRae, and A. I. Lvovsky,
A versatile digital GHz phase lock for external cavity diode lasers,
Measurement Science and Technology **20** (2009) 055302.

[138] S. Schroers, *to be published*, MA thesis: University of Bonn, 2025.

[139] C. J. Foot, *Atomic Physics*, Oxford: Oxford University Press, U.S.A., 2005,
ISBN: 978-0-19-850696-6.

[140] T. Arpornthip, C. A. Sackett, and K. J. Hughes,
Vacuum-pressure measurement using a magneto-optical trap,
Physical Review A **85** (2012) 033420.

[141] R. W. G. Moore, L. A. Lee, E. A. Findlay, L. Torralbo-Campo, G. D. Bruce, and D. Cassettari,
Measurement of vacuum pressure with a magneto-optical trap: A pressure-rise method,
Review of Scientific Instruments **86** (2015) 093108.

[142] W. Alt, *Optical control of single neutral atoms*, PhD thesis: University of Bonn, 2004.

[143] G. Reinaudi, T. Lahaye, Z. Wang, and D. Guéry-Odelin,
Strong saturation absorption imaging of dense clouds of ultracold atoms,
Optics Letters **32** (2007) 3143.

[144] W. J. Hinze, R. R. von Frese, and A. H. Saad, *Gravity and Magnetic Exploration*, Cambridge University Press, 2013, ISBN: 978-0-521-87101-3.

[145] T. M. Brzozowski, M. Maczynska, M. Zawada, J. Zachorowski, and W. Gawlik, *Time-of-flight measurement of the temperature of cold atoms for short trap-probe beam distances*, Journal of Optics B: Quantum and Semiclassical Optics **4** (2002) 62.

[146] N. Masuhara, J. M. Doyle, J. C. Sandberg, D. Kleppner, T. J. Greytak, H. F. Hess, and G. P. Kochanski, *Evaporative Cooling of Spin-Polarized Atomic Hydrogen*, Physical Review Letters **61** (1988) 935.

[147] W. Petrich, M. H. Anderson, J. R. Ensher, and E. A. Cornell, *Stable, Tightly Confining Magnetic Trap for Evaporative Cooling of Neutral Atoms*, Physical Review Letters **74** (1995) 3352.

[148] S. E. Hamann, D. L. Haycock, G. Klose, P. H. Pax, I. H. Deutsch, and P. S. Jessen, *Resolved-sideband raman cooling to the ground state of an optical lattice*, Physical Review Letters **80** (1998) 4149.

[149] V. Vuletić, C. Chin, A. J. Kerman, and S. Chu, *Degenerate Raman Sideband Cooling of Trapped Cesium Atoms at Very High Atomic Densities*, Physical Review Letters **81** (1998) 5768.

[150] A. J. Kerman, V. Vuletić, C. Chin, and S. Chu, *Beyond optical molasses: 3D raman sideband cooling of atomic cesium to high phase-space density*, Physical Review Letters **84** (2000) 439.

[151] M. Gröbner, P. Weinmann, E. Kirilov, and H.-C. Nägerl, *Degenerate Raman sideband cooling of* ^{39}K, Physical Review A **95** (2017) 033412.

[152] C. Tresp, *Rydberg polaritons and Rydberg superatoms - Novel tools for quantum nonlinear optics*, PhD thesis: Universität Stuttgart 5. Physikalisches Institut, 2017.

[153] S. Schroers, *Raman-Seitenbandkühlung von Rubidiumatomen*, bachelor: University of Bonn, 2022.

[154] N. Stiesdal, *Intrinsic three photon correlations mediated by a single Rydberg superatom*, MA thesis: University of Southern Denmark, 2018.

[155] R. H. Brown and R. Twiss, *LXXIV. A new type of interferometer for use in radio astronomy*, The London, Edinburgh, and Dublin Philosophical Magazine and Journal of Science **45** (1954) 663.

[156] R. H. Brown and R. Q. Twiss, *Correlation between Photons in two Coherent Beams of Light*, Nature **177** (1956) 27.

[157] T. A. Savard, K. M. O'Hara, and J. E. Thomas, *Laser-noise-induced heating in far-off resonance optical traps*, Physical Review A **56** (1997) R1095.

[158] P. Alken et al., *International Geomagnetic Reference Field: the thirteenth generation*, Earth, Planets and Space **73** (2021) 49.

[159] A. Corney, *Atomic and Laser Spectroscopy*, Oxford Classic Texts in the Physical Sciences Ser, Oxford: Oxford University Press, Incorporated, 2006, ISBN: 978-0-19-921145-6 978-0-19-152633-6.

[160] B. Albrecht, P. Farrera, G. Heinze, M. Cristiani, and H. de Riedmatten, *Controlled Rephasing of Single Collective Spin Excitations in a Cold Atomic Quantum Memory*, Physical Review Letters **115** (2015) 160501.

[161] V. Davydkin, B. Zon, N. L. Manakov, and L. P. Rapoport, *Quadratic Stark Effect on Atoms*, Journal of Experimental and Theoretical Physics **33** (1971).

[162] C. Glaser, F. Karlewski, J. Kluge, J. Grimmel, M. Kaiser, A. Günther, H. Hattermann, M. Krutzik, and J. Fortágh, *Absolute frequency measurement of rubidium 5S-6P transitions*, Physical Review A **102** (2020) 012804.

[163] L. Li, Y. O. Dudin, and A. Kuzmich, *Entanglement between light and an optical atomic excitation*, Nature **498** (2013) 466.

[164] H. J. Metcalf and P. Van Der Straten, *Laser Cooling and Trapping*, ed. by R. S. Berry, J. L. Birman, J. W. Lynn, M. P. Silverman, H. E. Stanley, and M. Voloshin, Graduate Texts in Contemporary Physics, New York, NY: Springer, 1999, ISBN: 978-0-387-98728-6 978-1-4612-1470-0.

[165] B. J. Lester, A. M. Kaufman, and C. A. Regal, *Raman cooling imaging: Detecting single atoms near their ground state of motion*, Physical Review A **90** (2014) 011804.

[166] C. H. Greene, A. S. Dickinson, and H. R. Sadeghpour, *Creation of Polar and Nonpolar Ultra-Long-Range Rydberg Molecules*, Physical Review Letters **85** (2000) 2458.

[167] V. Bendkowsky, B. Butscher, J. Nipper, J. P. Shaffer, R. Löw, and T. Pfau, *Observation of ultralong-range Rydberg molecules*, Nature **458** (2009) 1005.

[168] I. Mirgorodskiy, F. Christaller, C. Braun, A. Paris-Mandoki, C. Tresp, and S. Hofferberth, *Electromagnetically induced transparency of ultra-long-range Rydberg molecules*, Physical Review A: Atomic, Molecular, and Optical Physics **96** (2017) 011402.

[169] A. Gaj, A. T. Krupp, J. B. Balewski, R. Löw, S. Hofferberth, and T. Pfau, *From molecular spectra to a density shift in dense Rydberg gases*, Nature Communications **5** (2014) 4546.

[170] V. Bendkowsky et al., *Rydberg Trimers and Excited Dimers Bound by Internal Quantum Reflection*, Physical Review Letters **105** (2010) 163201.

[171] I. Mirgorodskiy, *Storage and propagation of Rydberg polaritons in a cold atomic medium*, PhD thesis: Universität Stuttgart 5. Physikalisches Institut, 2017.

[172] Y. Y. Fein, A. Shayeghi, L. Mairhofer, F. Kiałka, P. Rieser, P. Geyer, S. Gerlich, and M. Arndt, *Quantum-Assisted Measurement of Atomic Diamagnetism*, Physical Review X **10** (2020) 011014.

Acknowledgements

Over the course of this thesis, I came to appreciate the value of leading by example. Many of the people I thank here have served as examples to me, not only through their expertise, knowledge, and skills, but also through their remarkable personalities.

First, I would like to thank Prof. Dr. Sebastian Hofferberth for guiding me through this four-year educational journey as part of the latest incarnation of your nonlinear quantum optics group. Starting with a pile of boxes in an empty lab was an exciting challenge, and your trust gave me the opportunity to grow—not only in building the lab, but also personally. Thank you for the thoughtful and in-depth discussions that were essential for developing a deep understanding of physics together.

I would also like to thank Prof. Dr. Stefan Linden for being my second assessor, and sparking my interest for Optik und Wellenmechanik in the third semester.

I am especially grateful to Nina for all the time we spent together, both in and out of the lab, which truly shaped my experience during this thesis. Thank you for believing in me and I think you are the heart and positive spirit of our group. With you, I did not only find superatoms in the lab, but also my superperson. A special thank-you goes to Wolfgang for sharing all your knowledge and intuition—with me and everyone else interested. I will miss your small demonstration experiments, where every time a bit of your enthusiasm for and joy in discovery jumped over to me. A special thanks to Eduardo for the time spent together at the institute, especially during the pandemic. The spirit of the FCQED lab played a key role in building the RQO lab, right in the same room. I am grateful for the guidance provided by the senior members of our group, especially Hannes, Xin and Frank, who were always willing to answer questions and offer support.

My fellow PhDs. Cedric—you have been by my side (almost) from the beginning. Together, we figured out how to use all the various devices in the lab and what they are actually for. Now that our journey is coming to an end, I still have not figured out which muscle groups all those gym machines are supposed to train. Daniil—as part of the next generation, I have enjoyed seeing your enthusiasm and growth. And Chris—thank you for sharing your theoretical perspective and opening my eyes to new ways of thinking. As someone once said: "Theories[sts] are like children—there are none as wonderful as your own." Being part of such a wonderful research group has truly been a privilege. A special thank you to Lukas, Ludwig, Tangi, Julia, and Daniel—although we did not work closely together, meeting you for a coffee has always been a joy.

I am grateful to have worked with many outstanding Bachelor students—Simon, Jan, Bennet, Hannah, Matthias, and Chris. It always warms my heart (and makes me proud) when you—and others—stop by the office just to say hi. A special thanks goes to Simon and Jan, who briefly went their own way and then returned for their Master's theses.

I would also like to express my heartfelt gratitude to the heroes of the third floor. Tina, thank you for the amazing support throughout this entire journey. I truly admire your drive to change things, and not be satisfied with "It was always done like this." Dietmar, thank you for keeping this institute

together, and staying calm, when I asked for yet another key.

I am also deeply thankful to everyone who took the time to proofread this thesis.

To my friends both within and beyond the university—especially to my school friends, and the Beuchler-Keucher team—thank you for making my studies and thesis work so much more enjoyable. To my Duisdorf bike gang—Janek and Andi—thank you for all the bike rides, Frisbee Sundays, joint meals at the Mensa, and for sharing the best World-of-Hardstyle remix.

I am forever grateful to Frau S., for all the sessions that transformed my life.

Finally, to my parents and my sister—your love and support over all these years have been the foundation for this achievement.